PREDICTION OF STRUCTURAL AND THERMOCHEMICAL PROPERTIES: COMPUTATIONAL STRATEGIES FOR SMALL MOLECULES TO PERIODIC SYSTEMS

By

Zainab H. A. Alsunaidi

A DISSERTATION

Submitted to
Michigan State University
in partial fulfillment of the requirements
for the degree of

Chemistry – Doctor of Philosophy

2017

ABSTRACT

PREDICTION OF STRUCTURAL AND THERMOCHEMICAL PROPERTIES: COMPUTATIONAL STRATEGIES FOR SMALL MOLECULES TO PERIODIC SYSTEMS

By

Zainab H. A. Alsunaidi

The prediction of thermochemical properties is central in chemistry and is essential in industry to predict the stability of materials and to gain understanding about properties of reactions of interest such as enthalpies of formation, activation energies and reaction enthalpies. Advances in state-of-the-art computing and algorithms as well as high-level *ab initio* methods have accounted for the generation of a considerable amount of thermochemical data. Today, the field of thermochemistry is largely dominated by computational methods, particularly with their low cost relative to the cost of experiment.

There are many computational approaches used for the prediction of thermochemical properties. In selecting an approach, considerations about desired level of accuracy and computational efficiency need to be made. Strategies that have shown utility in the prediction of thermochemical properties with high accuracy and lower computational cost than high-level *ab initio* methods are *ab initio* composite approaches, or model chemistries, such as the correlation consistent Composite Approach (ccCA). ccCA has been shown to predict enthalpies of formation within "chemical accuracy", which is considered to be 1 kcal mol^{-1}, on average, for main group elements with respect to well-established experiments.

In this dissertation, ccCA and the commonly used G*n* composite methods have been utilized to establish effective routes for the determination of structural and thermochemical properties of oxygen fluorides species and for organoselenium compounds. To assess the

reliability of these approaches, enthalpies of formation were calculated and compared to experimental data. Density functionals have also been employed in these projects to examine their performance in comparison to experiments as well as to composite methods. The impact of several thermochemical approaches on the accuracy of the predicted enthalpies of formation via various computational methods has been also considered such as the traditional atomization approach and molecular reaction approaches.

Additionally, in this dissertation, the reaction of a direct amination of benzene to produce aniline on the Ni(111) surface was investigated to identify possible reaction intermediates and to determine the thermodynamically preferred reaction pathways. The adsorption behaviors and energetics of all species involved in this reaction are presented. Periodic density functionals were used to consider this heterogeneous catalytic process. Because DFT is based on the uniform electron gas model, which in principle resembles the band theory of metallic systems, DFT is particularly good at modeling metallic systems and thus well suited for the study of heterogeneous catalysts at the molecular level.

This dissertation is dedicated to my husband Uthman and children Riadh, Sahar, and Yousef.
Thank you for always believing in me.

ACKNOWLEDGMENT

I would first like to praise and thank Allah for all the countless blessings and for giving me the strength and courage to complete this dissertation. The faith in his support, glory, and mercy has always held me strong.

Upon completion, I would like to acknowledge many people who have been supportive during my graduate career. First, I would like to thank my research advisor Professor Angela K. Wilson for continuous support and patience during my PhD study at both the University of North Texas and Michigan State University. Her mentorship, guidance, motivation, and leadership have contributed to my growth as an independent scientist. I am very grateful to her for encouraging me to get publications and to present at conferences. Her words, advice, and actions have all granted me an incredible academic experience at the U.S.

I acknowledge financial support from the University of Dammam in Saudi Arabia. I believe that this scholarship has contributed successfully to my personal and academic development. It also gave me the opportunity to meet and learn from outstanding scientists from around the world. Without their financial support, none of this would have been possible.

I acknowledge Professor Thomas Cundari for collaboration on the work presented in Chapter 5 and for his support and enthusiastic sharing of knowledge. I thank my committee members here at Michigan State University Professor James "Ned" Jackson, Professor Gary Blanchard, and Professor Katharine Hunt for their time and suggestions. I also thank my former committee members at the university of North Texas Professor Thomas Cundari, Professor Paul Marshall, and Professor Mohammad Omary for their time and suggestions during my qualifying exams.

Thank you to my amazing colleagues in the Wilson group, past and present, for their continuous sharing of knowledge and techniques. Thank you to Dr. Jiaqi Wang and Michael Jones for support and helpful conversation. I thank Dr. Kameron Jorgensen, who introduced me to *ab initio* composite methods, Dr. Charlie Peterson for fruitful discussion and for help with my solid state calculations, and Dr. George Schoendorff and Dr. Inga Ulusoy for thoughtful and interesting discussions. I thank Dr. Deborah Penchoff, for her friendship, many enriching conversations, and help in managing challenges and stress along the way.

I thank my friends who have been there for me during my Ph.D. work. All of my friends in Denton have helped me to keep focus and maintain balance through these hectic years. I thank them for constant cheering and for making our stay in Denton a pleasant experience. The support from my friends in Saudi Arabia has always been substantial for my success. Their words, prayers, and encouragement always have been like fuel to continue and to succeed.

I am especially grateful to my immediate family for their love, prayers, words and encouragements that have been sources of strength and inspiration. I express my greatest gratitude to my parents, Sajedah and Dr. Husain, for their endless support, prayers, and love, and who made me what I am today. I am very grateful to my mother- and father-in-law, Khaledah and Riadh, for their support, love, and encouragement. My deepest gratitude goes to all my siblings for consistent motivation, support, love, prayers and always believing in me.

Finally, I am endlessly grateful to the love of my life, my husband, Uthman Alhumaidan, for his patience, understanding, and keeping me calm through all of my stressful challenges. Your wisdom, genius, kindness, love, and trust have contributed the most in my success. No such words can describe my gratitude and appreciation. You have been always there for me either to celebrate a little achievement or to overcome obstacles. I cannot remember any time that you

were disappointed in me even with all of my frustration and absence. Thank you for reminding me and keeping me involved in my kids' childhood. Without your support, none of this would have been possible. To my precious gems Riadh, Sahar, and Yousef, thank you for being such responsible, supportive, and respectful kids. Thank you for always bringing joy and love to my life. You are my heroes and my everything.

TABLE OF CONTENTS

LIST OF TABLES

LIST OF FIGURES

LIST OF SCHEMES

CHAPTER 1 INTRODUCTION

Computational chemistry is a rapidly growing field of chemistry that uses fundamental physics, mathematics, and computer simulation to investigate chemical systems. Advances in high computing performance have played an important role in improvements in computational methods and algorithms that, in turn, facilitate the elucidation of complex chemical systems, such as solids, biological macromolecules, polymers, and ionic liquids. Information such as electronic structure, reactivity of atoms and molecules, thermochemical and spectroscopic properties, just to name a few, can all be reliably provided from high-level theoretical calculations. This information helps chemists to gain in-depth understanding of a particular chemical problem and develop and design new reactions or systems. Computational applications also aid in interpreting available experimental measurements and provide predictions for systems/properties that are unknown or unexplored, or that are difficult to address experimentally. Nowadays, applications in critical areas such as anti-cancer drugs, energy development, astronomy, and green chemistry have been explored theoretically.

Two main classes of computational chemistry methods are molecular mechanics and electronic structure methods and within each class are numerous approaches. Each family of approaches differs in the type of approximation, attainable accuracy, and computing resources required (disk space, time, and memory). Knowing the applicability and limitations of a theory allow suitable methods to be selected for a given chemical problem while taking into account the system size, the target accuracy, the available computing resources, and the property of interest. Molecular mechanics (MM) are classical mechanics approaches that solve for Newton's equations of motion using pre-determined empirical force fields to describe potential energy

surface (PES). MM are highly useful approaches for providing molecular and thermodynamic properties of large molecules, as large as >10000 atoms, such as enzymes, from a macroscopic perspective. These approaches are used intensively in biochemical research. The reliability of a MM calculation depends on how accurate the empirically derived force fields are and how suitable/transferable they are for a system of interest and on the correct sampling of the phase space.

Electronic structure methods, on the other hand, are quantum mechanical approaches that are based on solving the time-independent Schrödinger equation and are increasingly important in chemistry, physics and material science. They can be categorized into three classes: *ab initio* molecular orbital (MO) theory, density functional theory (DFT), and semi-empirical methods. Both semi-empirical and *ab initio* methods are wave function based; however, unlike *ab initio* methods, semi-empirical methods, as expected from the name, use fitting parameters typically derived from experimental data (e.g. enthalpy of formation, ionization potentials, structural parameters, and dipole moments) to compensate for approximations made to the quantum mechanical model, such as neglecting two-electron integrals, i.e. electron correlation is approximated using empirical parameters. Although semi-empirical methods are computationally faster compared to *ab initio* methods, and can be applied to systems containing >1000 atoms, they are less accurate than *ab initio* methods and their accuracies are dependent on the experimental database for which they were parameterized.

In this dissertation, *ab initio* molecular orbital (MO) theory and density functional theory (DFT), discussed in more detail in Chapter 2, were employed to investigate systems spanning from small inorganic molecules to larger organic compounds to extended periodic systems. The aim is to utilize various computational approaches and strategies to predict accurate (within "or

near “chemical accuracy”) thermochemical properties and to evaluate the performance of these methods relative to experiment, where available. Another aspect of this work is to use density functional theory as well as statistical thermodynamic to identify and study possible adsorbed intermediates involved in a heterogeneous reaction process.

Ab initio methods are developed from first principles (physical constants), i.e. do not use empirically obtained force fields or parameters, and use several approximations to solve for the many-body Schrödinger equation. If these approximations are small in magnitude (such as in Configuration Interaction (CI)), accurate solutions to the Schrödinger equation can be achieved yet at high computational cost. These less approximated methods can be only applied to small molecules. Density functional theory, however, can be applied to larger systems (~100 - 1000 atoms) at a moderate computational cost, i.e. DFT scales as N^4, where N represents the number of basis functions. DFT solves for the Schrödinger equation in terms of the total electron density instead of a wave function. The solution for the Schrödinger equation provides a real numerical value of the energy of a system and its electron distribution. Calculating the second derivative of the energy (Hessian matrix) with respect to atomic positions determines force constants and vibrational frequencies. This information allows predicting thermochemical properties including enthalpies of formation, bond dissociation energies, ionization potentials, and electron affinities.

There are strategies that have been established to address the accuracy and high computational cost demands of high-level *ab initio* methods. For example, a number of *ab initio* composite approaches, or model chemistries, have been developed for predicting thermochemical properties with accuracies that mimic those possible from high-level *ab initio* methods, such as coupled cluster with single, double, and perturbative triple excitations (CCSD(T)), but with reduced computational cost. Composite methods utilize a series of steps

combining lower level methods and basis sets to replicate results with higher-level methods. Gaussian-*n* (G*n*) composite methods and the correlation consistent Composite Approach (ccCA) both are discussed in Chapter 2 and were utilized in Chapter 3 and Chapter 4.

Understanding the utility of theoretical methods for predicting energetic properties of various classes of molecules is important, and can lead to the development of effective strategies for future studies. In Chapter 3, composite methods including ccCA, G3, and G3B3 are utilized for the prediction of enthalpies of formation ($\Delta H°_f's$) for oxygen fluoride species, which is compared to reliable experimental data. In addition, the performance of several density functionals including M06 and M06-2X, for determining structures and $\Delta H°_f's$ of the same set of oxygen fluorides also was examined. The set includes fluorides, difluorides, dioxides, trioxides, and the corresponding hydrides. These molecules have been a great challenge for the computational community particularly due to the unusual geometry of molecules such FOO and FOOF.

The research in Chapter 4 includes the prediction of accurate enthalpies of formation for a set of organoselenium compounds using several thermochemical schemes via composite methods and density functionals. Selenium compounds play a substantial role in organic synthetic reactions, in the semiconductor industry, and in biochemistry. Thermochemical properties, particularly $\Delta H°_f's$, are of great importance in providing predictions and insight about chemical reactions including molecular stability, reaction enthalpy, and bond dissociation energy. Isodesmic and hypohomodesmotic reaction schemes have been developed to cancel errors arising from differential correlation effects and size extensivity (which will be discussed herein), which, in turn, can result in a better prediction of $\Delta H°'_f s$ as compared with the

conventional atomization approach.

In Chapter 5, plane-wave DFT is employed to investigate possible reaction mechanisms for the direct amination of benzene on the Ni(111) surface. The direct amination of benzene to produce aniline is of significant interest from a green chemistry perspective, although, it is very challenging because of the strong C-H bond of benzene and the N-H bond of ammonia. In this research, a full detailed study of this reaction including adsorption behaviors (structures, energetics, frequencies, electronic interactions) of all species on the Ni(111) surface and thermochemical properties is done and suggestions of reliable computational models are provided. The study uses the PBE and PBE-D3 functionals to determine adsorption structures and energetics for a variety of adsorption systems including adsorbed NH_x species and adsorbed aromatic species to consider possible reaction intermediates relevant to the direct amination of benzene. Statistical thermochemistry is employed to calculate reaction enthalpies and reaction free energies of the proposed reaction pathways between imide and benzene. The study also aims to compare and correlate a heterogeneous Ni(111)–imide model with the corresponding homogenous nickel-imide model for the C-H amination reaction. In Chapter 6, all of the research projects are summarized and future interests are discussed.

CHAPTER 2 THEORETICAL BACKGROUND

2.1 The Schrödinger Equation

In quantum mechanics, electrons are described using a wave function (Ψ). The wave function conveys all information of the state of the system and can be used with an operator to measure an observable property of a given system. A cornerstone wave equation of quantum mechanics is the non-relativistic time-dependent Schrödinger equation,[1–6] Eq. 2.1,

$$-\frac{\hbar}{i}\frac{\partial}{\partial t}\Psi(r,R,t) = \hat{H}\Psi(r,R,t) \tag{2.1}$$

where $\hat{H}$ is the Hamiltonian operator (the energy operator), $\Psi(r,R,t)$ is the wave function of electronic coordinates, nuclear coordinates, and time, respectively. i equals to $\sqrt{-1}$, and $\hbar$ equals to $h\ /\ 2\pi$, where h is the Planck's constant. The time-dependent Schrödinger equation describes how a wave function $\Psi(r,R,t)$ for a system evolves with time when governed by a Hamiltonian. In other words, it describes the dynamics of a given system and provides the probability distribution of the state of the particle at each time.

In quantum chemistry, many applications are concerned with obtaining the constant energy of stationary states, i.e. standing waves that have no time dependence, of a chemical system. Hence, the non-relativistic time-independent Schrödinger equation, Eq. 2.2, is widely used, which can be derived from Eq. 2.1 using the separation of variables principle in which the wave function is factored into a function that depends only on spatial coordinates and a function that depends only on time. The time-independent Schrödinger equation, Eq. 2.2, is employed in this dissertation and will be referred to as the Schrödinger equation henceforth. It is a second order differential equation in electronic and nuclear coordinates. The Schrödinger equation is

also an eigenvalue equation, where the Hamiltonian operator ($\hat{H}$) is applied to a wave function ($\psi(r,R)$) that describes the chemical system to give the total energy (E) of that system.[7]

$$\hat{H}\psi(r,R) = E\psi(r,R) \tag{2.2}$$

The Hamiltonian is shown in Eq. 2.3 in atomic units and is expressed as the sum of the kinetic energy ($\hat{T}$) and potential energy ($\hat{V}$) operators of *N* electrons (*i* and *j*) and *M* nuclei (*A* and *B*) within a system:

$$\hat{H} = \underbrace{-\frac{1}{2}\sum_{i=1}^{N}\nabla_i^2}_{\hat{T}_e} \underbrace{-\frac{1}{2}\sum_{A=1}^{M}\frac{\nabla_A^2}{M_A}}_{\hat{T}_n} \underbrace{-\sum_{A=1}^{M}\sum_{i=1}^{N}\frac{Z_A}{|R_A - r_i|}}_{\hat{V}_{ne}} + \underbrace{\sum_{i=1}^{N}\sum_{j>i}^{N}\frac{1}{|r_i - r_j|}}_{\hat{V}_{ee}} + \underbrace{\sum_{A=1}^{M}\sum_{B>A}^{M}\frac{Z_A Z_B}{|R_A - R_B|}}_{\hat{V}_{nn}} \tag{2.3}$$

where M_A is the mass of the nuclei, Z_A and Z_B are the charges of nuclei *A* and *B*, respectively. $|R_A - r_i|$ is the distance between an electron and a nucleus, $|r_i - r_j|$ is the distance between two electrons, $|R_A - R_B|$ is the distance between two nuclei, and ∇^2 is the Laplacian operator. The first two terms represent the kinetic energy operator of the electrons ($\hat{T}_e$) and the nuclei ($\hat{T}_n$). The following terms correspond to the potential energy operator of the attraction between electrons and nuclei ($\hat{V}_{ne}$), the repulsion between electrons ($\hat{V}_{ee}$), and the repulsion between nuclei ($\hat{V}_{nn}$).[8]

The Schrödinger equation, Eq. 2.2, elucidates that certain energy levels (eigenvalues) are allowed for a given system and correspond to wave functions that are the stationary state solutions (eigenfunctions) of this given system. The wave function itself is not measureable, however it can be squared ($\psi\psi^*$) to give the probability, $|\psi^2|$of finding an electron within a given region in space, according to Max Born,[9] i.e. it can describe the electron density of the

system. The integral of $|\psi^2|$ over all the volume space ($d\tau$) must be equal to one for a normalized wave function.

$$\int |\psi^2| \; d\tau = \langle \psi | \psi \rangle = 1 \tag{2.4}$$

2.1.1 Born-Oppenheimer Approximation

The Schrödinger equation cannot be solved exactly except for one electron systems such as hydrogen atom or hydrogenic cations. Thus, solving for the total energy for multi-electron systems requires the use of approximations due to the many body problems arising from the correlation of the motion of many electrons in the Schrödinger equation. One fundamental approximation is based on the fact that the masses of the nuclei are much larger than the mass of the electrons, which, in turn, means that the nuclei move more slowly than the electrons for a given kinetic energy. Thus, the nuclei can be considered fixed with respect to the motion of the electrons. This is the essence of the so-called Born-Oppenheimer approximation[10] that allows a decoupling of the nuclear and electronic motions. With the assumption that the electrons move in the field of fixed nuclei, the Hamiltonian can be reduced to an expression independent of the nuclear motion[8] as shown in Eq. 2.5,

$$\hat{H}_{elec} = \underbrace{-\frac{1}{2}\sum_{i=1}^{N} \nabla_i^2}_{\hat{T}_e} \underbrace{- \sum_{A=1}^{M}\sum_{i=1}^{N} \frac{Z_A}{|R_A - r_i|}}_{\hat{V}_{ne}} + \underbrace{\sum_{i=1}^{N}\sum_{j>i}^{N} \frac{1}{|r_i - r_j|}}_{\hat{V}_{ee}} \tag{2.5}$$

where the kinetic energy term of the nuclei ($\hat{T}_n$) is zero when applying the Born-Oppenheimer approximation. The repulsion between the nuclei ($\hat{V}_{nn}$) becomes a constant that is obtained classically via Coulomb's law. Since constant terms in an operator do not have an effect on the wave function, the ($\hat{V}_{nn}$) term is not included in the electronic Hamiltonian. When the electronic

Hamiltonian ($\hat{H}_{elec}$) is applied to a wave function, the electronic Schrödinger equation, Eq. 2.6, is obtained

$$\hat{H}_{elec}\psi_{elec}(r) = E_{elec}\psi_{elec}(r) \tag{2.6}$$

where $\psi_{elec}(r)$ is obtained from a separation of variables from $\psi(r, R)$.

The addition of the potential energy of the repulsion of nuclei ($\hat{V}_{nn}$) to the electronic energy (E_{elec}) results in the total energy (E_{tot}) of the system, as shown in Eq. 2.7.

$$E_{tot} = E_{elec} + \underbrace{\sum_{A=1}^{M}\sum_{B>A}^{M}\frac{Z_A Z_B}{|R_A - R_B|}}_{\hat{V}_{nn}} \tag{2.7}$$

2.1.2 Slater Determinant

The electronic wave function (ψ_{elec}) in the electronic Schrödinger equation (Eq. 2.6) must be a product of both the spatial and spin functions in order to fully describe an electron. As fermions, electrons cannot share the same set of quantum numbers, i.e. they must obey the Pauli exclusion principle.[11,12] Furthermore, the electronic wave function is required to be antisymmetric with respect to the interchange between spatial or spin functions. To achieve both conditions a determinant can be utilized to construct an antisymmetric wave function which was introduced first by Slater.[13] For an N-electron system ($\mathrm{x}_1, \mathrm{x}_2, \ldots, \mathrm{x}_N$) occupying N spin orbitals ($\chi_i, \chi_j, \ldots, \chi_N$) (2.8), the Slater determinant satisfies the requirement of an antisymmetric wave function,

$$\Psi(\mathrm{x}_1, \mathrm{x}_2, \ldots, \mathrm{x}_N) = \frac{1}{\sqrt{N!}} \begin{vmatrix} \chi_i(\mathrm{x}_1) & \chi_j(\mathrm{x}_1) & \cdots & \chi_N(\mathrm{x}_1) \\ \chi_i(\mathrm{x}_2) & \chi_j(\mathrm{x}_2) & \cdots & \chi_N(\mathrm{x}_2) \\ \vdots & \vdots & \ddots & \vdots \\ \chi_i(\mathrm{x}_N) & \chi_j(\mathrm{x}_N) & \cdots & \chi_N(\mathrm{x}_N) \end{vmatrix} \tag{2.8}$$

where $\frac{1}{\sqrt{N!}}$ is a normalization factor. The rows in a Slater determinant represent electrons and the columns represent spin orbitals. The interchange between two electrons (two rows) or two spin states (two columns) changes the sign of the determinant. In addition, if the same electron occupies the same spin orbital, then two columns will be equal and the determinant is zero.[8]

2.1.3 Variational Principle

The variational principle states that for a well-behaved wave function the expectation value of the Hamiltonian must result in an energy (E) that is greater than or equal to the exact ground state energy (E_0) of that system, as shown in Eq. 2.9, i.e. there is a lower bound to the energy.

$$E = \frac{\langle \Psi | \hat{\mathrm{H}} | \Psi \rangle}{\langle \Psi | \Psi \rangle} \geq E_0 \tag{2.9}$$

The wave function (Ψ) here is a trial wave function and the expectation value is the resultant trial energy (E). For a normalized wave function, the denominator $\langle \Psi | \Psi \rangle$, as mentioned earlier, equals 1 and thus the energy (E) will equal to $\langle \Psi | \hat{\mathrm{H}} | \Psi \rangle$.

The variational principle allows the determination of the best wave function that gives the most accurate energy, i.e. the lowest energy of a given system. The more parameters the trial wave function contains, the closer the trial energy is to the exact ground state energy.

In order to solve the Schrödinger equation, approximate forms of the electronic Hamiltonian, termed methods, are used in combination with basis sets, which are mathematical functions used to construct the wave function. There are now several methods utilized for this purpose, such as *ab initio* methods, semiempirical methods, and density functional theory (DFT). Here the focus is only on the *ab initio* and density functional methods.

2.2 *Ab initio* Methods

Ab initio means "from the beginning," indicating that these calculations are based on quantum mechanics, physical constants, and laws of physics without reference to empirical data or parameters. The lack of experimental parameters makes *ab initio* methods flexible to apply to different systems and problems without showing any degree of bias. Various *ab initio* methods have been developed based on the type of approximation employed to solve the Schrödinger equation.

2.2.1 Hartree-Fock Approximation

The Hartree-Fock (HF) approximation[14–18] is among the simplest *ab initio* methods and is often the first approximation made when solving the Schrödinger equation for multi-electron systems. It can be used to provide a well-defined starting point for more advanced wave function based methods. The electron-electron repulsion in HF theory is computed using the mean-field approximation that treats the motion of each electron in an average potential field of other electrons. The Hartree-Fock wave function (Ψ_{HF}) is a single Slater determinant and for an N electron system occupying N spin orbitals ($\chi_i, \chi_j, \ldots, \chi_N$) is

$$\Psi_{HF} = |\chi_1 \chi_2 \cdots \chi_N\rangle \tag{2.10}$$

The variational principle is used to select the "best" spin orbitals that will give the lowest energy when using the HF equation, Eq. 2.10. The eigenvalue HF equation can be written as

$$\hat{f}_i \chi_i(i) = \varepsilon_i \chi_i(i) \tag{2.11}$$

where $\chi_i(i)$ represents the one-electron orbital wave function, ε_i is the energy of that orbital, and $\hat{f}_i$ is the Fock operator of the form

$$\hat{f}_i = -\frac{1}{2}\nabla_i^2 - \sum_{A=1}^{nuclei} \frac{Z_A}{|R_A - r_i|} + v^{HF}(i) \tag{2.12}$$

The first two terms in the Fock operator, Eq 2.12, represent the one-electron core Hamiltonian ($\hat{h}_i$), which consists of the kinetic energy of the electron and the potential energy of the attraction between the electron and nuclei, respectively. $v^{HF}(i)$ corresponds to the effective potential of the interaction of the ith electron with the average charge density of the rest of the electrons, and is called the Hartree-Fock potential. The HF potential depends on the coulomb and the exchange potentials that are generated from the interaction of one-electron with the field of the remaining electrons. Because this term depends on all other electrons, an iterative scheme must be used to solve the HF equation in order to obtain optimized orbitals and their energies. This can be achieved by using the self-consistent field (SCF) methods.

The solutions to the HF equation are a set of optimized molecular orbitals (MOs) that are constructed from the linear combination of the one-electron atomic orbitals (LCAO). The HF limit can be obtained by using an infinite set of basis functions (that construct the one-electron

atomic orbitals) and it provides the lowest energy accessible for the ground state energy of a system when electron correlation is a mean field correlation.

The HF approximation accounts for ~99% of the total energy of a system,[19] the remaining ~1% energy, which is due to the electron-electron correlation beyond the mean field approximation, is critical for describing the chemistry of a given problem.[20] The electron correlation energy (E_{corr}) is defined as the difference between the exact energy of a system (E_{exact}) and the HF energy (E_{HF}).

$$E_{corr} = E_{exact} - E_{HF} \tag{2.13}$$

2.2.2 Post-HF Methods

To obtain more accurate information of a chemical system, post-HF methods have been developed to account for the electron correlation energy. Examples of these methods include configuration interaction (CI), Møller-Plesset perturbation theory (MP*n*), and coupled cluster theory (CC). The electron correlation energy can be accounted for by mixing in excited state determinants in addition to the HF Slater determinant to improve the quality of the wave function. The linear combination of the HF wave function and the excited state determinants results in a new trial energy that is lower than the HF energy and approaches to the exact energy when using a variational method, such as CI and CC. This multi-determinant wave function can be written as

$$\Psi = a_0\Phi_{\mathrm{HF}} + \sum_{i=1} a_i\Phi_i \tag{2.14}$$

where a_0 is the coefficient of the HF wave function Φ_{HF} and it depends on the normalization of the wave function. The a_i coefficients define the weight of each excited state determinant Φ_i into the wave function.

2.2.2.1 Configuration Interaction

The CI method is similar to the HF method where both utilize the variational principle. However, instead of using a single Slater determinant in the HF approximation, CI defines the wave function (Ψ_{CI}) as a linear combination of the possible determinants arising from excitations from the reference state. Typically, the reference state is the Slater determinant corresponding to the ground state HF wave function (Φ_{HF}), though faster convergence to the exact energy sometimes can be obtained using other reference wave functions. The possible excitations can be grouped as single (S), double (D), triple (T), etc., excitations from the reference state up to n-tuple excitations, where n is the number of electrons. If the CI expansion (Eq. 2.15)[20] is not truncated, then the method is called Full Configuration Interaction (Full-CI).

$$\Psi_{\mathrm{CI}} = a_0\Phi_{\mathrm{HF}} + \sum_{\mathrm{S}} a_{\mathrm{S}}\Phi_{\mathrm{S}} + \sum_{\mathrm{D}} a_{\mathrm{D}}\Phi_{\mathrm{D}} + \sum_{\mathrm{T}} a_{\mathrm{T}}\Phi_{\mathrm{T}} + \cdots = \sum_{i=0} a_i\Phi_i \qquad (2.15)$$

In Equation 2.15, a_i is the coefficient corresponding to each configuration and each a_i is a variational parameter that is varied to minimize the total energy. Full CI provides the "exact" non-relativistic solution of the Schrödinger equation within the Born-Oppenheimer approximation for the working basis. When a complete basis set is used, the method is called Complete CI and the truly exact non-relativist energy is obtained.

The computational cost of Full CI increases dramatically as the number of orbitals increases, to which the Full CI becomes impractical. A binomial coefficient, shown in Eq. 2.16,

can be used to provide the number of determinants required for a system with K number of orbitals and N number of electrons

$$\binom{2K}{N} = \frac{(2K)!}{N!\,(2K-N)!} \tag{2.16}$$

Because of the high computational scaling of the Full CI method, it is usually truncated to include only certain number of the possible excited state determinants. For example, CIS only includes the ground state wave function and the singly excited determinants. CISD includes the singly and doubly excites determinants as well as the ground state wave function, and so on. These truncated CI methods, although can be computational feasible, they are size inconsistent methods. If the energy calculated from the sum of energies of two individual atoms is equal to the energy calculated when these two atoms are at infinite distance from each other, i.e. they are non-interacting, then the method is size consistent.[8]

2.2.2.2 Perturbation Theory

Another non-variational method for recovering correlation energy is many-body perturbation theory (MBPT). The MBPT concept is to use a well-defined approximate solution to Schrödinger equation to a certain chemical problem as a reference and then add a correction to this reference as a perturbation. The assumption is that the approximate solution that is used as the zeroth order Hamiltonian and wave function should be close to the exact solution, i.e. the perturbation must be small if the perturbation expansion series is to be convergent. Mathematically, MBPT defines the full Hamiltonian operator ($\widehat{H}$) of a system as a sum of two parts, a reference, unperturbed zeroth order Hamiltonian ($\widehat{H}_0$) and a perturbation Hamiltonian ($\lambda H'$), where (λ) defines the level of perturbation (correction), Eq. 2.17.

$$\hat{H} = \hat{H}_0 + \lambda H' \tag{2.17}$$

In addition, the perturbed wave function is expanded in the form

$$\Psi = \Psi_0 + \sum_{i=1}^{n} \lambda^i \Psi_i \tag{2.18}$$

and the total energy will be in the form

$$\mathrm{E} = \mathrm{E}_0 + \sum_{i=1}^{n} \lambda^i \mathrm{E}_i \tag{2.19}$$

One commonly used form of perturbation theory is the Møller-Plesset (MP*n*) perturbation theory.[21] The MP*n* perturbation theory uses the sum over the one-electron Fock operator, defined in Eq. 2.12, as the zeroth order Hamiltonian ($\hat{H}_0$) and the Hartree-Fock determinant as the zeroth order wave function (Ψ_0). The Fock operator double counts the average electron-electron term $\langle V_{ee} \rangle$, thus the perturbation Hamiltonian, which represents the remaining correlation, becomes[8,20]

$$H' = \hat{H} - \hat{H}_0 = \langle V_{ee} \rangle - 2 \langle V_{ee} \rangle = - \langle V_{ee} \rangle \tag{2.20}$$

where the $\hat{H}$ is the full electronic Hamiltonian.

The wave function and the energy can then be expanded in Taylor series. The eigenvalue equation of the *i*th eigenfunctions when the perturbations is added can be written as

$$(\hat{H}^{(0)} + \lambda H')(\sum_{n=0} \lambda^n \Psi_i^{(n)}) = (\sum_{n=0} \lambda^n \mathrm{E}_i^{(n)}) (\sum_{n=0} \lambda^n \Psi_i^{(n)}) \tag{2.21}$$

where n represent the order of the perturbation to the zeroth order energy $E^{(0)}$. The first-order energy correction returns the Hartree-Fock energy, i.e. it does not include electron correlation beyond HF theory. The most commonly used MP*n* method is the second-order energy correction

(MP2) method, which only involves perturbation of double excitation states and accounts for about 80-90% of correlation energy.[20] The energy of the second order correction has the form[22]

$$E(\mathrm{MP}_2) = \sum_{i<j}^{occ} \sum_{a<b}^{vir} \frac{\langle \Phi_0 | \mathrm{H}' | \Phi_{ij}^{ab} \rangle \langle \Phi_{ij}^{ab} | \mathrm{H}' | \Phi_0 \rangle}{E_0 - E_{ij}^{ab}} \tag{2.22}$$

where i and j refer to occupied orbitals, a and b refer to virtual orbitals. Φ_0 is the HF wave function and Φ_{ij}^{ab} is the doubly excited wave function.

2.2.2.3 Coupled Cluster Theory

Coupled cluster theory (CC)[23–26] is similar to the CI method in that it uses the HF wave function as a starting point to construct the CC wave function that includes excited state determinants (e.g. S, D, T, Q, etc.). The CC wave function (Ψ_{CC}), Eq. 2.23, includes an exponential cluster operator $\hat{T}$, defined in Eq. 2.24 and Eq. 2.25, that acts on the reference wave function (Φ_0) to generate all possible excitation states,

$$\Psi_{CC} = e^{T} \Phi_0 \tag{2.23}$$

$$\hat{T} = \hat{T}_1 + \hat{T}_2 + \cdots + \hat{T}_{Nelec} \tag{2.24}$$

$$\begin{aligned} e^{T} = 1 + \hat{T}_1 + \left(\hat{T}_2 + \frac{1}{2!}\hat{T}_1^{\,2}\right) + \left(\hat{T}_3 + \hat{T}_1\hat{T}_2 + \frac{1}{3!}\hat{T}_1^{\,3}\right) + \left(\hat{T}_4 + \hat{T}_3\hat{T}_1 \right. \\ \left. + \frac{1}{2!}\hat{T}_2^{\,2} + \frac{1}{2!}\hat{T}_1^{\,2}\hat{T}_2 + \frac{1}{4!}\hat{T}_1^{\,4} + \cdots \right) \end{aligned} \tag{2.25}$$

where Φ_0 is the HF wave function. The first term in Eq. 2.24 is the HF determinant. Single excitation states are generated by $\hat{T}_1$, double excitation are generated by $\hat{T}_2$ and $\hat{T}_1^{\,2}$, triple

excitations are generated by $\hat{T}_3$, $\hat{T}_1\hat{T}_2$, and $\hat{T}_1{}^3$. All $\hat{T}_i$ are connected operators while the remaining other operators are called disconnected operators (products of connected operators), such as $\hat{T}_1{}^2$ and $\hat{T}_1\hat{T}_2$. Examples of the excitations are shown below, where t is the amplitude which is analogous to the a_i coefficient of the CI method. Eq. 2.26 and Eq. 2.27 are two examples of single and double excitations, respectively, using connected operators. Eq. 2.28, on the other hand, represents triple excitations using disconnected operators.

$$\hat{T}_1|\Psi_0\rangle = \sum_{i}^{occ}\sum_{a}^{vir} t_i^a\,|\Psi_i^a\rangle \tag{2.26}$$

$$\hat{T}_2|\Psi_0\rangle = \frac{1}{4}\sum_{i\,j}^{occ}\sum_{a\,b}^{vir} t_{i\,j}^{a\,b}\,|\Psi_{i\,j}^{a\,b}\rangle \tag{2.27}$$

$$\hat{T}_1\hat{T}_2|\Psi_0\rangle = \frac{1}{4}\sum_{i\,j\,k}^{occ}\sum_{a\,b\,c}^{vir} t_i^a t_{j\,k}^{b\,c}\,|\Psi_{i\,j\,k}^{a\,b\,c}\rangle \tag{2.28}$$

…

The utilization of the disconnected operators in the CC methods allows the generations of all possible excitation configurations of each type of excited determinant. It is the cluster operator that makes the CC theory an outstanding computational method and superior over the CI method. In fact, it is the inclusion of the disconnected cluster operators that accounts for the faster convergence to the exact energy of the CC expansion compared to the CI expansion. Moreover, it is also the disconnected cluster operators that make a truncated CC expansion size extensive in contrast to a truncated CI expansion.

Perhaps the most widely used coupled cluster method is the CCSD(T), which includes single and double excitations and a perturbative inclusion of triple excitations. CCSD(T) in

conjunction with sufficiently large basis functions can usually provide accurate energetics within ± 1 kcal mol^{-1} deviation from experimental data for the light main group species that are dominated by a single determinant.[20]

Although the post-HF methods yield more accurate energetics than HF alone, these methods can be computationally intensive. The HF method scales as N^4, where N is the number of basis functions. The cost of post-HF methods typically increases exponentially or even combinatorially. While the minimal scaling of the correlation methods (post-HF methods) is N^5 as in MP2, it can be as high as $N^{N!}$ as in the Full CI. CCSD and CCSD(T), on the other hand, scale as N^6 and N^7, respectively. MP3 and MP4 scale as N^6 and N^6, respectively. As the computational scaling of an *ab initio* method increases, the computational cost in terms of memory, CPU time, and disk space increases. Thus, achieving a balance between efficiency and accuracy is often important particularly for large chemical systems.

2.3 Density Functional Theory

Density functional theory (DFT)[27–29] is a common electronic structure method that is used in physics, chemistry, and material science to study chemical and physical related problems. DFT scales roughly the same as HF, (N^4), but with a pre-factor that is dependent of the density functional employed. The advantage is that DFT accounts for electron correlation energy typically at a lower computational cost than post-HF methods. Modern DFT has been developed based on two theorems: the Hohenberg-Kohn[30] and the Kohn-Sham[31] theorems, in which both rely on the fact that there is a unique relationship between the electron density and the ground state energy.[30,31] Thus, all properties of a given system can be calculated as a function of the

electron density $\rho(r)$, which is the square of the wave function integrated over N-1 electron coordinates, Eq. 2.29. In *ab initio* methods, the wave function depends on the 3N coordinates of each of n-electrons (can be 4N if electron spin is taken into account), while in DFT the electron density is only a function of the three dimensions of space, i.e. $\rho(r) = f(x, y, z)$.

$$\rho(r) = N \sum_{i=1}^{N_{elec}} \int |\Psi(r_1, r_2, \cdots, r_N)|^2 \, dr_2 dr_3 \cdots dr_N \tag{2.29}$$

In the Kohn-Sham (KS) theory, the kinetic energy is calculated from an N independent non-interacting electron system that is constructed from a single determinant wave function of a fully interacting system.[31] The total Kohn-Sham DFT energy ($E[\rho]$) for a fully interacting system is defined as in Eq. (2.30)[20]

$$E[\rho] = T_S[\rho] + E_{ne}[\rho] + J[\rho] + E_{XC}[\rho] \tag{2.30}$$

where $T_S[\rho]$ is the kinetic energy of the non-interacting electrons, $E_{ne}[\rho]$ is the potential energy of the attraction between the nuclei and the electrons, $J[\rho]$ is the Coulomb term representing the electron-electron repulsion, and $E_{XC}[\rho]$ is the exchange-correlation energy that accounts for all the remaining terms of the electron-electron interactions, e.g. the kinetic energy caused by interacting electrons. The DFT energy expression, Eq. (2.30), is within the Born-Oppenheimer approximation as there is no nuclear kinetic energy and the internuclear repulsions are still solved classically.

The exchange-correlation energy $E_{XC}[\rho]$ is a functional of the electron density and can be divided into two approximate functionals; the exchange functional ($E_X[\rho]$) corresponding to the same-spin electron interactions and the correlation functional ($E_C[\rho]$) corresponding to the mixed-spin electron interactions as

$$E_{XC}[\rho] = E_X[\rho] + E_C[\rho] \tag{2.31}$$

Because the exact form of the exchange-correlation functional is unknown, a variety of approximations of the E_{XC} formulations have been developed. These approximations can be categorized into two main classes: the local density approximation (LDA), which utilizes local functionals that depend only on the electron density (ρ) and the generalized gradient approximation (GGA) that uses gradient-corrected functionals that depend not only on the electron density (ρ) but also on its gradient (∇_ρ). Perdew[42] presented a hierarchy of DFT functionals and named it the "Jacob's Ladder" of DFT, which includes LDA (first rung), GGA (second rung), meta-GGA (third rung), hybrid-GGA (fourth rung), and double hybrid GGA (fifth rung). The most commonly used functionals are LDA up to the hybrid GGA, which will be introduced herein.

2.3.1 Local Density Approximation (LDA)

The LDA[32] is the simplest approximation in which the density is treated locally as a non-interacting uniform electron gas. In LDA, the density is defined as $\rho = N/V$, where N is the number of electrons and V is the volume of the gas. This form of electron density is only used in the LDA. Generally, since electrons have spin α or spin β, LDA is replaced by the local spin density approximation (LSDA). In LSDA, the total electron density ρ is replaced by the spin electronic density, ρ_α and ρ_β. The LSDA approximation generally provides better molecular geometries and vibrational frequencies than the HF approximation; however, it tends to overestimate the chemical bonding.[33] The LDA approximation is commonly used in solid-state

physics for studying metals where the electron density varies slowly.[34] One of the commonly used LSDA functionals is VWN.[35]

2.3.2 Generalized Gradient Approximation (GGA)

Since in LDA the electron density is treated as a local property that does not reflect the spatial variation in densities, the GGA method[36–41] corrects for this shortcoming by including the electron density and its first derivative (∇_ρ). One of the commonly used GGA corrected exchange functionals is B88 developed by Becke[36] in which a correction parameter is added to the LDA exchange energy. GGA corrected correlation functionals were also developed, such as the LYP[38] functional and the P86[42] functional. Because the exchange-correlation energy is comprised from two terms, the exchange and the correlation terms, the gradient-corrected exchange functional can be combined with the gradient-corrected correlation functional. The most widely used combinations are BLYP,[36,38] PBE,[40,41] and BP86.[36,42] The PBE functional is a non-empirical functional and has numerous applications on metallic systems largely because it correctly describes the slowly varying electron densities of metals.

2.3.3 Meta-GGA

Additional improvement over the GGA method is the meta-GGA (MGGA) approach in which more inhomogeneity property is added to the electron density by including the second derivative of the electron density ($\nabla^2\rho$) and/or, local kinetic energy density ($\tau\rho$). These additional terms can offer a better performance than LDA and GGA particularly in the

description of chemical interactions. TPSS[43] and M06-L[44] are commonly used meta-GGA functionals.

2.3.4 Hybrid- GGA

In DFT, the description of the exchange energy suffers from the self-interaction problem that arises from the spurious interaction of an electron with itself. The idea in hybrid functionals is to use the Hartree-Fock exact exchange in addition to the Kohn-Sham correlation. This can help improve the performance of the exchange functional of the DFT. However, the inclusion of 100% of the HF exchange term can in some cases worsen the performance of the functional because it can result in a poor description of the total exchange-correlation hole of DFT. Combination of HF exchange with DFT exchange, however, largely improves the description of molecularly properties.[33,45] Two types of the hybrid functionals are developed. The first one is the hybrid GGA (HGGA) in which the HF exchange function is added to a pure GGA functional. B3LYP is one of the most popular hybrid-GGA functional containing 20% of HF exchange.[33,38,46] In addition, B3PW91 is another popular hybrid-GGA functional that also includes 20% of HF exchange.[33,47] The other type of hybrid functional is hybrid MGGA (HMGGA). In this type, a percentage of HF exchange energy is added to the MGGA functional. The Minnesota functionals M06, M062X, and M06-HF are all useful HMGGA functionals,[48] in which M06 contains 27%, M06-2X contains 54%, and M06-HF contains 100% HF exchange.

2.4 Basis Sets

In the previous sections, the focus was on using several computational methods, such as *ab initio* methods and density functional theory, to approximate the Hamiltonian operator in the

Schrödinger equation. However, the accuracy of all the methods depends on the number and quality of the basis functions (basis sets) that are used to describe the wave function. Basis sets are basically vectors that are used to define a certain region of space. In quantum chemistry, basis sets are mathematical functions that describe the molecular orbitals (MOs) and can be expanded as a linear combination of atomic orbitals or basis functions (χ_r) Eq. (2.32),

$$\phi_i = \sum_r c_{ri}\chi_r \tag{2.32}$$

where ϕ represent a MO and c_{ri} are the weighting coefficients indicating the relative importance of each basis function (or atomic orbital) χ_r.

A finite number of basis functions is always used in conjunction with an electronic structure method to construct the wave function (Ψ) which is used as a solution to the Schrödinger equation. This finite set can be a source of error in the calculation and is usually referred to as incomplete basis set error. Types of basis sets commonly used are atom-centered basis sets, such as the Pople basis sets[49–52] and the correlation consistent basis sets developed by Dunning and coworkers.[53–59] These basis sets are constructed using basis functions localized in a region of space. Another kind of basis set is constructed with plane waves. Plane waves are delocalized basis function basis sets that are usually used for describing periodic systems, such as crystals.[60]

2.4.1 Atom-Centered Basis Sets

The atomic orbital basis sets are sets of localized functions used to construct atomic orbitals. The linear combination of these atomic orbitals produces the MOs of a given system.

Two types of these basis sets have commonly been used: Slater-type orbitals (STOs)[7,61] and Gaussian-Type orbitals (GTOs)[62–64].

STOs are developed to resemble the hydrogen atomic orbitals and are expressed as:

$$\Psi(\mathrm{r},\theta,\phi) = N\, Y_l^m\,(\theta,\phi) r^{n-1}\, e^{-\zeta r} \tag{2.33}$$

where N is the normalization factor and Y_l^m is the angular function and is defined by the angular (l) and magnetic (m) quantum numbers. r is the distance between the electron and the nucleus and (n) is the principle quantum number. ζ is the exponent and it determines the spatial extent of the function, i.e. small ζ gives diffuse functions while large ζ gives tight function. STOs can successfully describe short range and long range behavior to correctly describe the cusp at the nucleus and the tail, respectively. While STOs correctly describe these regions, electronic integrals cannot be solved analytically and thus must be computed numerically. This results in additional computational expense while also making the quality of the computed results dependent on the size of the integration grid.

Alternatives to STOs are GTOs which have the following functional form:

$$\Psi(\mathrm{r},\theta,\phi) = N\, Y_l^m\,(\theta,\phi) r^{2n-2-l}\, e^{-\zeta r^2} \tag{2.34}$$

where the radius exponent here is squared ($e^{-\zeta r^2}$) compared to the exponent in the STOs ($e^{-\zeta r}$). This formulation is easier to compute than the STOs since integrals over GTOs have analytic solutions. However, the performance of the GTOs at the cusp and the tail of a radial function is poor. GTOs have a zero gradient at the r=0 rather than a cusp in addition to decaying too slowly in the tail region. To improve the performance of the GTOs, multiple GTOs are used in a linear combination to reproduce the shape of STOs. This requires many functions, thus contracted

GTOs are often used to minimize the computational expense. As the number of GTOs included in the linear combination increases, the description of the atomic orbital using the GTOs become more accurate.

A minimal basis set is the smallest number of basis functions that can describe all electrons of an atom, i.e. one function per atomic orbital. For example, the minimal basis set of hydrogen is one basis function representing the 1*s* atomic orbital. For the carbon atom, and other first row elements, the minimal basis set includes two functions for the 1*s* and 2*s* orbitals and three functions for the p_x, p_y, and p_z. Although the minimal basis set can describe atomic orbitals, it is not enough to describe the molecular orbitals where atomic orbitals can undergo distortion. Furthermore, minimal GTO basis sets cannot reproduce the cusp and tail regions correctly. To overcome this shortcoming, additional basis functions can be added to the valence orbitals since they are essential for chemical bonding. These basis sets are called split-valence basis sets. To illustrate, a double-ζ basis set has two GTO functions for each valence orbitals, a triple-ζ basis set has three GTO functions for each valence orbitals, and so on.

2.4.1.1 Pople Basis Sets

Pople and coworkers[49–52] developed the Gaussian split-valence basis sets that employ the contracted GTOs concept. A general notation of a Pople double-ζ basis set is X-YZG, where X represents the number of the primitive GTOs used to construct the contracted GTO for core orbitals. YZ represent the number of primitive GTOs used to make two contracted GTOs for the valence orbitals. For Pople triple-ζ basis set, a number will be added to the split valence function to show how many primitive GTOs used to make the third contracted GTO for the valence orbital, e.g. X-YZTG. Common examples of the Pople double-ζ basis set are 6-31G, 6-21G, 4-

31G, 3-21G, etc. and Pople triple-ζ basis set can be written as 6-311G. Polarization functions can be added to the basis set to better describe distortion or polarization that occurs when a bond is formed. In order to allow for this polarization, the angular momentum of the polarizing function must increase by one compared with the type of function being polarized, e.g. p-functions to polarize s-functions, d-functions to polarize p-functions, etc. These functions are represented by an asterisk "*" as in 6-31G*. They also can be denoted by adding d or p, such as 6-31G(d,p), in which a set of d functions are added to non-hydrogen atoms and a set of p functions are added to the hydrogen atom. Diffuse functions that have small ζ exponents are added to account for long range interaction, such as if an electron is far away from the nucleus as happens in anionic systems. Diffuse functions are represented as a plus sign "+" as in 6-31+G which means s and p functions are added to non-hydrogen atoms.

2.4.1.2 Correlation Consistent Basis Sets

The correlation consistent (cc) basis sets introduced by Dunning and coworkers[53–59] were designed in order to systematically and predictably recover the correlation energy of the valence electrons by increasing the number of the basis functions per atoms.[56] Specifically, these basis sets built on the idea that functions recovering same amount of correlation energy are added to the same shell. The correlation consistent (cc) basis sets are denoted as cc-pVnZ, where pV indicates polarized valence functions, Z is zeta, and n is related to the number of functions used to describe the valence orbitals. The n also can be an indication of the maximum angular momentum function contained within the basis set. The zeta level differs for different values of n. The values of n can be D(2), T(3), Q(4), 5, and 6 and so on. For example, for first row atoms, in which the minimal basis set is 2*s*1*p*, the cc-pVDZ set includes 3*s*2*p*1*d*, where a *d* polarized

function is added. The cc-pVTZ includes 4*s*3*p*2*d*1*f*, where the second *d* and the first *f* recover the same amount of correlation energy. The cc-pVQZ includes 5*s*4*p*3*d*2*f*1*g*, in which the third *d*, the second *f*, and the first *g* recover the same amount of correlation energy. The reason for the inclusion of these higher basis functions is to systematically recover more correlation energy of a molecule.

The systematic recovery of the correlation energy built in these basis sets allows for the extrapolation of the correlation energy to the complete basis set (CBS) limit where the error arising from the use of a finite basis set vanishes, yet the intrinsic error from the chosen method remains. Various extrapolation techniques estimate the CBS limit, including the Peterson extrapolation scheme[65] and the Schwartz extrapolation scheme.[66] Further discussion of the extrapolation schemes of the correlation consistent basis set is presented in Section 2.5.2.

Additive basis functions such as diffuse functions (aug)[54,57] and polarized core-valence correlating functions (CV)[56,59] can also be added without affecting the convergent behavior of the basis sets, such as aug-cc-pCVTZ. The diffuse functions are often added to help describe long-range interactions, while the polarized core-valence correlating functions are used when the subvalence or core electrons are included in the correlated method in addition to the electrons in the valence space. Additionally, a relativistic re-contraction of the Hartree-Fock set of functions is often used in conjunction with relativistic calculations.[67] This re-contraction often provides faster convergence of the relativistic wave function as well as aiding in optimization to the correct electronic state.

2.4.2 Plane Wave Basis Sets

Plane wave (PW) basis sets are basis sets used to describe valence electrons in extended systems, such as solids and crystals, and are used in conjunction with periodic boundary conditions (PBC). Since the valence electrons in periodic systems behave as free electrons, using the atom-centered basis sets to describe these systems is impractical. Rather, plane wave basis sets are used and are delocalized across the entire periodic system. The discrete energy levels vanish in periodic systems, thus bands are formed rather than localized atomic and molecular orbitals.

For a periodic system, plane wave basis functions ($e^{i\mathrm{kr}}$) are used to construct the periodic wave function $\Psi_{\mathrm{k}}(\mathrm{r})$, Eq. 2.35. This wave function obeys the Bloch theorem[68] that states that "the eigenfunction of the wave equation for a periodic potential is the product of a plane wave ($e^{i\mathrm{k.r}}$) times a function $\mathrm{u_k}(\mathrm{r})$ with the periodicity of the crystal lattice". Thus, $\Psi_{\mathrm{k}}(\mathrm{r})$ represents a numerical solution to the Schrödinger equation.

$$\Psi_{\mathrm{k}}(\mathrm{r}) = e^{i\mathrm{kr}} \tag{2.35}$$

In Eq. 2.35, k is the wave vector. The size of a plane wave basis set is controlled by the highest value of the k vector.[69] Plane wave basis sets are very large compared with all-electron basis sets. Since these basis sets are not spatially bound, an energy cut-off has to be set to allow for an SCF convergence. A common energy cut off value is 200 eV, which corresponds to about 20,000 basis functions depending on the size of the unit cell being modeled.[20]

2.4.2.1 Pseudopotentials

The core electrons in the metallic systems are strongly localized near the nuclei, which in turn requires a large number of PW functions in order to describe this behavior. Plane wave basis sets work well in describing the valence electrons in extended systems but are inefficient at describing core electrons. Since core electrons are not significantly involved in chemical bonding and reaction, the effect of core electrons can be implicitly described using pseudopotentials, which smear the nuclear charges and model the effect of the core electrons.

Different types of pseudopotentials have been developed, such as norm-conserving pseudopotentials,[70] ultra-soft pseudopotentials,[71] and the projector augmented-wave (PAW) pseudopotentials.[72,73] The PAW method developed by Blöchl is known to be an efficient method for predicting the electronic structure of materials because it is capable to include the upper core electrons as well as the valence electrons in the self-consistent iteration of the Kohn equations. In the PAW method, the exact wave function of the core electrons is mapped onto an auxiliary pseudo-wave function in the core region using projectors and retaining the correct nodal structure of the pseudo-wave function, in contrast, to standard pseudopotentail methods.[72]

2.5 Composite Methods

In order to reduce the computational cost of high level *ab initio* calculations, composite methods or model chemistries have been developed. These methods are constructed of sequential additive steps of a combination of high level methods with a small basis sets and low level methods with large basis sets resulting in a high level of accuracy with lower computational cost. Composite methods that have been developed include the Gaussian-*n* (G*n*) methods by Pople et

al.,[74–83] the Weizmann-*n* (W*n*) methods by Martin et al.,[84–89] the High accuracy Extrapolated *Ab initio* Thermochemistry (HEAT) method by Stanton et al.,[90–92] the complete basis set (CBS) methods by Petersson et al.,[93–98] and the correlation consistent Composite Approach (ccCA) by Wilson et al.[99–110] Herein the G*n* methods and the ccCA are introduced and are used in Chapter 3 and Chapter 4.

2.5.1 Gaussian-*n* (G*n*) Theory

Gaussian-*n* methods are composite methods that perform sequential *ab initio* molecular calculations to predict accurate thermochemical properties at low computational cost. The original G*n* method is the Gaussian-1 (G1) developed by Pople and coworkers[74–83] with a target accuracy of ± 2 kcal mol^{-1} for compounds containing first-row elements and ± 3 kcal mol^{-1} for compounds containing second-row elements.[74] The G1 method performs poorly for the dissociation energies of ionic species, triplet states, some hydrides, and hypervalent species.[75] Therefore, a series of developments have been implemented in G1 and other versions of the G*n* theories have been developed including G2,[75] G3,[78] and G4[82] with higher target accuracy of ~1 kcal mol^{-1}. In addition, each G*n* theory has several variants, for example, the G3 family of composite methods includes G3(MP2),[80] G3B3,[79] and G3-RAD.[111]

The most commonly used version of G*n* methods is G3, which is used in Chapter 3 and Chapter 4 of this dissertation. In G3, a sequence of *ab initio* molecular orbital calculations is performed to predict accurate energetics. The following computational steps are used in G3:[78]

1. Initial geometry optimization and frequency calculations are carried out at the HF/6-31G(d) level of theory. A scaling factor of 0.8929 is used to correct for the anharmonicity in the vibrations. These frequencies are used to calculate the zero point energy, E(ZPE).

2. Equilibrium geometries are then obtained using the MP2(full)/6-31G(d) level of theory. This equilibrium structure is used for all the single point energy calculations that follow.
3. A single point energy calculation is performed at the MP4/6-31G(d) level. The energy obtained from this step is the reference energy of the G3 method.
4. A series of single point energy calculations are carried out at high level of theories and are used to improve the reference energy as follows:
    a. A correction for the correlation effect beyond the MP4 method using the quadratic configuration interaction method (QCISD(T)),[112] $\Delta E(QCI)$:

$$\Delta E(QCI) = E[QCISD(T)/6\text{-}31G(d)]\text{-}E[MP4/6\text{-}31G(d)] \tag{2.36}$$

    b. A correction for diffuse functions, $\Delta E(+)$:

$$\Delta E(+) = E[MP4/6\text{-}31+G(d)]\text{-}E[MP4/6\text{-}31G(d)] \tag{2.37}$$

    c. A correction for higher polarization function, $\Delta E(2df,p)$:

$$\Delta E(2df,p) = E[MP4/6\text{-}31G(2df,p)]\text{-}E[MP4/6\text{-}31G(d)] \tag{2.38}$$

    d. A correction for a larger basis set effect, $\Delta E(G3large)$:

$$\Delta E(G3large) = E[MP2(full)/G3large]\text{-}E[MP2/6\text{-}31G(2df,p)]\text{-}E[MP2/6\text{-}31+G(d)]+E[MP2/6\text{-}31G(d)] \tag{2.39}$$

5. Atomic spin orbit correction is included, $\Delta E(SO_a)$.
6. An empirical "high level correction" (E(HLC)) is added to the reference energy to recover any remaining correlation energy, such as correlation of valence electron pairs

and correlation of unpaired electrons in molecules. HLC also aims to minimize the difference between theory and experiment in the predicted enthalpies of formation and atomization energies.

7. A combination of the reference energy and all other contribution results in the G3 energy at 0 K, E_0(G3):

$$E_0(G3) = E[MP4/6\text{-}31G(d)] + \Delta E(QCI) + \Delta E\,(+) + \Delta E(2df,p) + \Delta E(G3large) + E(HLC) + \Delta E(SO_a) + E(ZPE) \quad (2.40)$$

The goal of the G3 method is to achieve target accuracy within the QCISD(T)/G3Large level of theory.

G3B3 method[79] is similar to G3 in that both perform single point energy calculations at the same level and procedure but at different structure. The geometry optimization in G3 is at MP2(full)/6-31G(d) level of theory; in contrast, G3B3 uses the B3LYP/6-31G(d) level of theory to predict structures and to calculate zero point energy. G3B3 actually was developed for open-shell systems where the unrestricted MP2 method, used in G3, suffers from spin contamination of the HF reference wavefunction.[79] The inclusion of the empirical parameters within the HLC term introduces a bias in the G_n methods.

2.5.2 Correlation Consistent Composite Approach (ccCA)

The ccCA method, developed by Wilson and coworkers,[99–110] avoids the use of the empirical high-level correction (HLC) found in the G*n* methods and utilizes the convergence behavior of the correlation consistent basis sets to eliminate the basis set incompleteness error. The ccCA method is designed to approach the [CCSD(T,FC1)-DK/aug-cc-pCV∞Z-DK] energy at a reduced computational cost, which in turn, can achieve the chemical accuracy of 1 kcal/mol

of reliable experiments for energetic properties of main group species, on average. The detailed computational steps in ccCA are as follows:

1. A geometry optimization and frequency calculation are performed at the B3LYP/cc-pVTZ. The optimized structure is determined to be a minimum on the potential energy surface via a Hessian calculation. Harmonic vibrations are scaled by a factor of 0.989 in order to account for anharmonicity and are used to calculate the zero point energy,E(ZPE). The equilibrium structure predicted in this step is used for all the single point energy calculations that follow.
2. A single point energy calculation is carried out at the MP2/cc-pVnZ level, where n= D, T, and Q and the energies are extrapolated to the CBS limit to obtain the ccCA reference energy. The HF reference energies (resulted from this step) are extrapolated to the CBS limit using the Feller extrapolation scheme:[113,114]

$$E(n) = E_{HF-CBS} + B \exp(-1.63n) \tag{2.41}$$

Where $E(n)$ is the energy at the nth zeta-level of the used basis set, E_{HF-CBS} is the extrapolated HF energy to the CBS limit, and B is a fitting variable. The energy resulting from this extrapolation is the E(HF/CBS).

The MP2 valence correlation energies are then extrapolated using one of the following extrapolation schemes. One option is the Peterson extrapolation scheme which is a mixed Gaussian and exponential formula:[65]

$$E(n) = E_{CBS} + B \exp[-(n-1)] + C \exp[-(n-1)^2] \tag{2.42}$$

where $E(n)$ is the energy at the nth zeta-level of the used basis set, E_{CBS} is the energy at the CBS limit, and B and C are fitting parameters. The ccCA variant that utilizes the Peterson extrapolation scheme is referred to as ccCA-P. Other alternative extrapolation schemes are the Schwartz extrapolation schemes,[66] which are based on the cubic or quartic inverse power of the highest order angular momentum (l_{max}) function included in the basis set:

$$E(l_{max}) = E_{CBS} + \frac{B}{(l_{max} + \frac{1}{2})^x} \tag{2.43}$$

where at x = 3 ccCA is designated as ccCA-S3 and is designated as ccCA-S4 at x = 4. The energy resulting from this extrapolation is the E(MP2)/CBS.

3. A series of single point energy calculations are carried out at high level of theories and are used as additive terms that added to the ccCA reference energy. These calculations as follows:

    a. A contribution of a scalar relativistic effect is accounted for using the spin-free one-electron Douglas-Kroll Hamiltonian at the MP2 level with the corresponding relativistically re-contracted basis set, ΔE(DK):

    $$\Delta E(DK) = E[MP2\text{-}DK/cc\text{-}pVTZ\text{-}DK] - E[MP2/cc\text{-}pVTZ] \tag{2.44}$$

    b. A contribution of the core-core and the core-valence correlation effects is determined by employing an MP2 calculation that correlates the outer core as well as the valence in conjunction with a core-valence basis set, ΔE(CV):

$$\Delta E(CV) = E[MP2(FC1)/aug\text{-}cc\text{-}pCVTZ] - E[MP2/aug\text{-}cc\text{-}pVTZ] \quad (2.45)$$

where FC1 indicates that outer core electrons are correlated in addition to the valence.

c. A contribution of high levels of electron correlation that are not described by MP2 is determined using CCSD(T) with the cc-pVTZ basis set, $\Delta E(CC)$:

$$\Delta E(CC) = E[CCSD(T)/cc\text{-}pVTZ] - E[MP2/cc\text{-}pVTZ] \quad (2.46)$$

4. Atomic spin orbit correction is included, $\Delta E(SO_a)$.
5. Finally, a combination of the reference energy and all other contribution results in the ccCA energy at 0 K, $E_0(ccCA)$:

$$E_0(ccCA) = E(HF/CBS) + E(MP2/CBS) + \Delta E(CC) + \Delta E(CV) + \Delta E(DK) + \Delta E(SO_a) + E(ZPE) \quad (2.47)$$

Various variants of ccCA have been developed including the ccCA-TM[115] for first row transition metal, the relativistic-pseudopotential (rp)-ccCA[108] for transition metals heavier than 3d elements, multireference (MR)-ccCA[106] for molecules with multireference characters, and ONIOM-ccCA[107] for large chemical system. Other implementations in ccCA include methods to decrease the computational cost such as the resolution-of-the-identity (RI)-ccCA[105] and the ccCA-F12.[109] All of which have been found to be efficient and accurate, overall, within the target accuracy.

REFERENCES

REFERENCES

(1) Schrödinger, E. Quantisierung Als Eigenwertproblem. *Ann. Phys.* **1926**, *386* (18), 109–139.

(2) Schrödinger, E. Quantisierung Als Eigenwertproblem. *Ann. Phys.* **1926**, *384* (6), 489–527.

(3) Schrödinger, E. Quantisierung Als Eigenwertproblem. *Ann. Phys.* **1926**, *80* (13), 437–490.

(4) Schrödinger, E. Über Das Verhältnis Der Heisenberg□Born□Jordanschen Quantenmechanik Zu Der Meinen. *Ann. Phys.* **1926**, *384* (8), 734–756.

(5) Schrödinger, E. An Undulatory Theory of the Mechanics of Atoms and Molecules. *Phys. Rev.* **1926**, *28* (6), 1049–1070.

(6) Kragh, H. Erwin Schrödinger and the Wave Equation: The Crucial Phase. *Centaurus* **1982**, *26* (2), 154–197.

(7) Levine, I. N. *Quantum Chemistry*, 7th ed.; Pearson Education Inc.: New York, U. S., 2014.

(8) Szabo, A.; Ostlund, N. S. *Modern Quantum Chemistry: Introduction to Advanced Electronic Structure Theory*, 1st ed.; Dover Publications, Inc.: Mineola, New York, 1996.

(9) Born, M. Zur Quantenmechanik Der Stoßvorgänge. *Z. Physik.* **1926**, *37* (12), 863–867.

(10) Born, M.; Oppenheimer, R. Zur Quantentheorie Der Molekeln. *Ann. Phys.* **1927**, *389* (20), 457–484.

(11) Pauli, W. Über Den Zusammenhang Des Abschlusses Der Elektronengruppen Im Atom Mit Der Komplexstruktur Der Spektren. *Z. Physik.* **1925**, *31* (1), 765–783.

(12) Pauli, W. Exclusion Principle and Quantum Mechanics. In *Writings on Physics and Philosophy*; Springer Berlin Heidelberg: Berlin, Heidelberg, 1994; pp 165–181.

(13) Slater, J. C. The Theory of Complex Spectra. *Phys. Rev.* **1929**, *34* (10), 1293–1322.

(14) Hartree, D. R. The Wave Mechanics of an Atom with a Non-Coulomb Central Field. Part III. Term Values and Intensities in Series in Optical Spectra. *Math. Proc. Cambridge*

Philos. Soc. **1928**, *24* (3), 426–437.

(15) Hartree, D. R. The Wave Mechanics of an Atom with a Non-Coulomb Central Field. Part II. Some Results and Discussion. *Math. Proc. Cambridge Philos. Soc.* **1928**, *24* (1), 111–132.

(16) Hartree, D. R. The Wave Mechanics of an Atom with a Non-Coulomb Central Field. Part I. Theory and Methods. *Math. Proc. Cambridge Philos. Soc.* **1928**, *24* (1), 89–110.

(17) Fock, V. Näherungsmethode Zur Lösung Des Quantenmechanischen Mehrkörperproblems. *Z. Physik.* **1930**, *61* (1), 126–148.

(18) Fock, V. "Selfconsistent Field" Mit Austausch Für Natrium. *Z. Physik.* **1930**, *62* (11), 795–805.

(19) Combs, L. L.; Holloman, M. Semiempirical Calculations of Internal Barriers to Rotation and Ring Puckering. *J. Mol. Struct.* **1976**, *33* (2), 289–305.

(20) Jensen, F. *Introduction to Computational Chemistry*, 2nd ed.; John Wiley & Sons Ltd.: Chichester, U.K., 2007.

(21) Møller, C.; Plesset, M. S. Note on an Approximation Treatment for Many-Electron Systems. *Phys. Rev.* **1934**, *46* (7), 618–622.

(22) Jensen, F. *Introduction to Computational Chemistry, 2nd Ed*; John Wiley & Sons, Ltd: West Sussex, England, 2007.

(23) Čížek, J. On the Correlation Problem in Atomic and Molecular Systems. Calculation of Wavefunction Components in Ursell□Type Expansion Using Quantum□Field Theoretical Methods. *J. Chem. Phys.* **1966**, *45* (11), 4256–4266.

(24) Purvis, G. D.; Bartlett, R. J. A Full Coupled□cluster Singles and Doubles Model: The Inclusion of Disconnected Triples. *J. Chem. Phys.* **1982**, *76* (4), 1910–1918.

(25) Raghavachari, K.; Trucks, G. W.; Pople, J. A.; Head-Gordon, M. Reprint of: A Fifth-Order Perturbation Comparison of Electron Correlation Theories. *Chem. Phys. Lett.* **2013**, *589*, 37–40.

(26) Bartlett, R. J.; Musia, M. Coupled-Cluster Theory in Quantum Chemistry. *Rev. Mod. Phys.* **2007**, *79* (1), 291–352.

(27) Koch, W.; Holthausen, M. C. *A Chemist's Guide to Density Functional Theory*, 2ed ed.; Wiley-VCH Verlag GmbH: Weinheim, Germany, 2002.

(28) Sholl, D. S.; Steckel, J. A. *Density Functional Theory : A Practical Introduction*, 1st ed.; John Wiley & Sons, Inc.: New Jersey, U.S., 2009.

(29) Tsuneda, T. *Density Functional Theory in Quantum Chemistry*; Springer Japan: Tokyo, Japan, 2014.

(30) Hohenberg, P.; Kohn, W. Inhomogeneous Electron Gas. *Phys. Rev.* **1964**, *136* (3), B864–B871.

(31) Kohn, W.; Sham, L. J. Self-Consistent Equations Including Exchange and Correlation Effects. *Phys. Rev.* **1965**, *140* (4), A1133–A1138.

(32) Politzer, P.; Abu-Awwad, F. A Comparative Analysis of Hartree-Fock and Kohn-Sham Orbital Energies. *Theor. Chem. Acc.* **1998**, *99* (2), 83–87.

(33) Becke, A. D. A New Mixing of Hartree–Fock and Local Density-Functional Theories. *J. Chem. Phys.* **1993**, *98* (2), 1372–1377.

(34) Lewars, E. G. *Computational Chemistry: Introduction to the Theory and Applications of Molecular and Quantum Mechanics*, 2nd ed.; Springer Science, Business Media B.V.: Dordrecht, Netherlands, 2011.

(35) Vosko, S. H.; Wilk, L.; Nusair, M. Accurate Spin-Dependent Electron Liquid Correlation Energies for Local Spin Density Calculations: A Critical Analysis. *Can. J. Phys.* **1980**, *58* (8), 1200–1211.

(36) Becke, A. D. Density-Functional Exchange-Energy Approximation with Correct Asymptotic Behavior. *Phys. Rev. A* **1988**, *38* (6), 3098–3100.

(37) Becke, A. D. Density-Functional Exchange-Energy Approximation with Correct Asymptotic Behavior. *Phys. Rev. A, Gen. Phys.* **1988**, *38* (6), 3098–3100.

(38) Lee, C.; Yang, W.; Parr, R. G. Development of the Colle-Salvetti Correlation-Energy Formula into a Functional of the Electron Density. *Phys. Rev. B* **1988**, *37* (2), 785–789.

(39) Miehlich, B.; Savin, A.; Stoll, H.; Preuss, H. Results Obtained with the Correlation Energy Density Functionals of Becke and Lee, Yang and Parr. *Chem. Phys. Lett.* **1989**, *157* (3), 200–206.

(40) Perdew, J. P.; Burke, K.; Ernzerhof, M. Generalized Gradient Approximation Made Simple. *Phys. Rev. Lett.* **1996**, *77*, 3865–3868.

(41) Perdew, J. P.; Burke, K.; Ernzerhof, M. Erratum: Generalized Gradient Approximation Made Simple. *Phys. Rev. Lett.* **1997**, *78* (7), 1396–1396.

(42) Perdew, J. P. Density-Functional Approximation for the Correlation Energy of the Inhomogeneous Electron Gas. *Phys. Rev. B* **1986**, *33* (12), 8822–8824.

(43) Tao, J.; Perdew, J. P.; Staroverov, V. N.; Scuseria, G. E. Climbing the Density Functional Ladder: Nonempirical Meta–Generalized Gradient Approximation Designed for Molecules and Solids. *Phys. Rev. Lett.* **2003**, *91* (14), 146401–146401.

(44) Zhao, Y.; Truhlar, D. G. A New Local Density Functional for Main-Group Thermochemistry, Transition Metal Bonding, Thermochemical Kinetics, and Noncovalent Interactions. *J. Chem. Phys.* **2006**, *125* (19), 194101–194118.

(45) Becke, A. D. Density-Functional Thermochemistry. III. The Role of Exact Exchange. *J. Chem. Phys.* **1993**, *98* (7), 5648.

(46) Burke, K. Perspective on Density Functional Theory. *J. Chem. Phys.* **2012**, *136* (15), 150901–150909.

(47) Perdew, J. P.; Wang, Y. Accurate and Simple Analytic Representation of the Electron-Gas Correlation Energy. *Phys. Rev. B* **1992**, *45* (23), 13244–13249.

(48) Zhao, Y.; Truhlar, D. The M06 Suite of Density Functionals for Main Group Thermochemistry, Thermochemical Kinetics, Noncovalent Interactions, Excited States, and Transition Elements: Two New Functionals and Systematic Testing of Four M06-Class Functionals and 12 Other Functionals. *Theor. Chem. Acc.* **2008**, *120* (1), 215–241.

(49) Hehre, W. J.; Stewart, R. F.; Pople, J. A. Self□Consistent Molecular□Orbital Methods. I. Use of Gaussian Expansions of Slater□Type Atomic Orbitals. *J. Chem. Phys.* **1969**, *51* (6), 2657–2664.

(50) Hehre, W. J.; Ditchfield, R.; Pople, J. A. Self-Consistent Molecular Orbital Methods. XII. Further Extensions of Gaussian-Type Basis Sets for Use in Molecular Orbital Studies of Organic Molecules. *J. Chem. Phys.* **1972**, *56* (5), 2257–2261.

(51) Binkley, J. S.; Pople, J. A.; Hehre, W. J. Self-Consistent Molecular Orbital Methods. 21. Small Split-Valence Basis Sets for First-Row Elements. *J. Am. Chem. Soc.* **1980**, *102* (3), 939–947.

(52) Krishnan, R.; Binkley, J. S.; Seeger, R.; Pople, J. A. Self□consistent Molecular Orbital Methods. XX. A Basis Set for Correlated Wave Functions. *J. Chem. Phys.* **1980**, *72* (1), 650–654.

(53) Dunning, T. H. Gaussian Basis Sets for Use in Correlated Molecular Calculations. I. The Atoms Boron through Neon and Hydrogen. *J. Chem. Phys.* **1989**, *90* (2), 1007–1023.

(54) Woon, D. E.; Dunning, T. H. Gaussian Basis Sets for Use in Correlated Molecular Calculations. III. The Atoms Aluminum through Argon. *J. Chem. Phys.* **1993**, *98* (2), 1358–1371.

(55) Woon, D. E.; Dunning, T. H. Gaussian Basis Sets for Use in Correlated Molecular Calculations. IV. Calculation of Static Electrical Response Properties. *J. Chem. Phys.* **1994**, *100* (4), 2975–2988.

(56) Woon, D. E.; Dunning, T. H. Gaussian Basis Sets for Use in Correlated Molecular Calculations. V. Core□valence Basis Sets for Boron through Neon. *J. Chem. Phys.* **1995**, *103* (11), 4572–4585.

(57) Wilson, A. K.; Woon, D. E.; Peterson, K. A.; Dunning, T. H. Gaussian Basis Sets for Use in Correlated Molecular Calculations. IX. The Atoms Gallium through Krypton. *J. Chem. Phys.* **1999**, *110* (16), 7667–7676.

(58) Dunning, T. H.; Peterson, K. A.; Wilson, A. K. Gaussian Basis Sets for Use in Correlated Molecular Calculations. X. The Atoms Aluminum through Argon Revisited. *J. Chem. Phys.* **2001**, *114* (21), 9244–9253.

(59) Peterson, K. A.; Dunning, T. H. Accurate Correlation Consistent Basis Sets for Molecular Core–valence Correlation Effects: The Second Row Atoms Al–Ar, and the First Row Atoms B–Ne Revisited. *J. Chem. Phys.* **2002**, *117* (23), 10548–10560.

(60) Kohanoff, J. *Electronic Structure Calculations for Solids and Molecules: Theory and Computational Methods*; Cambridge University Press: Cambridge, UK, 2006.

(61) Cook, D. B. *Handbook of Computational Quantum Chemistry*; Dover Publications Inc.: Mineola, U.S., 2005.

(62) Boys, S. F. Electronic Wave Functions. I. A General Method of Calculation for the Stationary States of Any Molecular System. *Proc. R. Soc. London* **1950**, *A200* (1063), 542–554.

(63) Boys, S. F. Electronic Wave Functions. II. A Calculation for the Ground State of the Beryllium Atom. *Proc. R. Soc. London* **1950**, *A201* (1064), 125–137.

(64) O-ohata, K.; Taketa, H.; Huzinaga, S. Gaussian Expansions of Atomic Orbitals. *J. Phys. Soc. Japan* **1966**, *21* (11), 2306–2313.

(65) Peterson, K. A.; Woon, D. E.; Dunning, T. H. Benchmark Calculations with Correlated Molecular Wave Functions. IV. The Classical Barrier Height of the $H+H_2 \rightarrow H_2+H$ Reaction. *J. Chem. Phys.* **1994**, *100* (10), 7410–7415.

(66) Schwartz, C. Importance of Angular Correlations between Atomic Electrons. *Phys. Rev.* **1962**, *126* (3), 1015–1019.

(67) de Jong, W. A.; Harrison, R. J.; Dixon, D. A. Parallel Douglas–Kroll Energy and Gradients in NWChem: Estimating Scalar Relativistic Effects Using Douglas–Kroll Contracted Basis Sets. *J. Chem. Phys.* **2001**, *114* (1), 48–53.

(68) Bloch, F. Über Die Quantenmechanik Der Elektronen in Kristallgittern. *Z. Physik.* **1929**, *52* (7), 555–600.

(69) Kittel, C. *Introduction to Solid State Physics*, 8th ed.; John Wiley & Sons, Inc.: New Jersy, USA, 2005.

(70) Zunger, A.; Cohen, M. L. First-Principles Nonlocal-Pseudopotential Approach in the Density-Functional Formalism: Development and Application to Atoms. *Phys. Rev. B* **1978**, *18* (10), 5449–5472.

(71) Vanderbilt, D. Soft Self-Consistent Pseudopotentials in a Generalized Eigenvalue Formalism. *Phys. Rev. B* **1990**, *41* (11), 7892–7895.

(72) Blöchl, P. E. Projector Augmented-Wave Method. *Phys. Rev. B* **1994**, *50* (24), 17953–17979.

(73) Kresse, G.; Joubert, D. From Ultrasoft Pseudopotentials to the Projector Augmented-Wave Method. *Phys. Rev. B* **1999**, *59* (3), 1758–1775.

(74) Pople, J. A.; Head□Gordon, M.; Fox, D. J.; Raghavachari, K.; Curtiss, L. A. Gaussian□1 Theory: A General Procedure for Prediction of Molecular Energies. *J. Chem. Phys.* **1989**, *90* (10), 5622–5629.

(75) Curtiss, L. A.; Raghavachari, K.; Trucks, G. W.; Pople, J. A. Gaussian□2 Theory for Molecular Energies of First□ and Second□row Compounds. *J. Chem. Phys.* **1991**, *94* (11), 7221–7230.

(76) Curtiss, L. A.; Carpenter, J. E.; Raghavachari, K.; Pople, J. A. Validity of Additivity Approximations Used in Gaussian□2 Theory. *J. Chem. Phys.* **1992**, *96* (12), 9030–9034.

(77) Curtiss, L. A.; Raghavachari, K.; Pople, J. A. Gaussian□2 Theory Using Reduced Møller–

Plesset Orders. *J. Chem. Phys.* **1993**, *98* (2), 1293–1298.

(78) Curtiss, L. A.; Raghavachari, K.; Redfern, P. C.; Rassolov, V.; Pople, J. A. Gaussian-3 (G3) Theory for Molecules Containing First and Second-Row Atoms. *J. Chem. Phys.* **1998**, *109* (18), 7764–7776.

(79) Baboul, A. G.; Curtiss, L. A.; Redfern, P. C.; Raghavachari, K. Gaussian-3 Theory Using Density Functional Geometries and Zero-Point Energies. *J. Chem. Phys.* **1999**, *110* (16), 7650–7657.

(80) Curtiss, L. A.; Redfern, P. C.; Raghavachari, K.; Rassolov, V.; Pople, J. A. Gaussian-3 Theory Using Reduced Møller-Plesset Order. *J. Chem. Phys.* **1999**, *110* (10), 4703–4709.

(81) Curtiss, L. A.; Raghavachari, K. Gaussian-3 and Related Methods for Accurate Thermochemistry. *Theor. Chem. Acc.* **2002**, *108* (2), 61–70.

(82) Curtiss, L. A.; Redfern, P. C.; Raghavachari, K. Gaussian-4 Theory. *J. Chem. Phys.* **2007**, *126*, 084108–084112.

(83) Curtiss, L. A.; Redfern, P. C.; Raghavachari, K. Gaussian-4 Theory Using Reduced Order Perturbation Theory. *J. Chem. Phys.* **2007**, *127* (12).

(84) Martin, J. M. L.; de Oliveira, G. Towards Standard Methods for Benchmark Quality Ab Initio thermochemistry-W1 and W2 Theory. *J. Chem. Phys.* **1999**, *111* (5), 1843–1856.

(85) Martin, J. M. L. Heat of Atomization of Sulfur Trioxide, SO3: A Benchmark for Computational Thermochemistry. *Chem. Phys. Lett.* **1999**, *310* (3–4), 271–276.

(86) Parthiban, S.; Martin, J. M. L. Assessment of W1 and W2 Theories for the Computation of Electron Affinities, Ionization Potentials, Heats of Formation, and Proton Affinities. *J. Chem. Phys.* **2001**, *114* (14), 6014–6029.

(87) Boese, A. D.; Oren, M.; Atasoylu, O.; Martin, J. M. L.; Kállay, M.; Gauss, J. W3 Theory: Robust Computational Thermochemistry in the kJ/mol Accuracy Range. *J. Chem. Phys.* **2004**, *120* (9), 4129–4141.

(88) Karton, A.; Rabinovich, E.; Martin, J. M. L.; Ruscic, B. W4 Theory for Computational Thermochemistry: In Pursuit of Confident Sub-kJ/mol Predictions. *J.Chem. Phys*. **2006**, *125*, 144108–144117.

(89) Karton, A.; Martin, J. M. L. Performance of W4 Theory for Spectroscopic Constants and Electrical Properties of Small Molecules. *J. Chem. Phys.* **2010**, *133* (14), 144102–144117.

(90) Tajti, A.; Szalay, P. G.; Császár, A. G.; Kállay, M.; Gauss, J.; Valeev, E. F.; Flowers, B. A.; Vázquez, J.; Stanton, J. F. HEAT: High Accuracy Extrapolated Ab Initio Thermochemistry. *J. Chem. Phys.* **2004**, *121* (23), 11599–11613.

(91) Bomble, Y. J.; Vázquez, J.; Kállay, M.; Michauk, C.; Szalay, P. G.; Császár, A. G.; Gauss, J.; Stanton, J. F. High-Accuracy Extrapolated Ab Initio Thermochemistry. II. Minor Improvements to the Protocol and a Vital Simplification. *J. Chem. Phys.* **2006**, *125* (6), 064108–064115.

(92) Harding, M. E.; Vázquez, J.; Ruscic, B.; Wilson, A. K.; Gauss, J.; Stanton, J. F. High-Accuracy Extrapolated Ab Initio Thermochemistry. III. Additional Improvements and Overview. *J. Chem. Phys.* **2008**, *128* (11), 114111–114115.

(93) Petersson, G. A.; Bennett, A.; Tensfeldt, T. G.; Al□Laham, M. A.; Shirley, W. A.; Mantzaris, J. A Complete Basis Set Model Chemistry. I. The Total Energies of Closed□ shell Atoms and Hydrides of the First□row Elements. *J. Chem. Phys.* **1988**, *89* (4), 2193–2218.

(94) Montgomery, J. A.; Ochterski, J. W.; Petersson, G. A. A Complete Basis Set Model Chemistry. IV. An Improved Atomic Pair Natural Orbital Method. *J. Chem. Phys.* **1994**, *101* (7), 5900–5909.

(95) Ochterski, J. W.; Petersson, G. A.; Montgomery, J. A. A Complete Basis Set Model Chemistry. V. Extensions to Six or More Heavy Atoms. *J. Chem. Phys.* **1996**, *104* (7), 2598–2619.

(96) Montgomery, J. A.; Frisch, M. J.; Ochterski, J. W.; Petersson, G. A. A Complete Basis Set Model Chemistry. VI. Use of Density Functional Geometries and Frequencies. *J. Chem. Phys.* **1999**, *110* (6), 2822–2827.

(97) Montgomery, J. A.; Frisch, M. J.; Ochterski, J. W.; Petersson, G. A. A Complete Basis Set Model Chemistry. VII. Use of the Minimum Population Localization Method. *J. Chem. Phys.* **2000**, *112* (15), 6532–6542.

(98) Wood, G. P. F.; Radom, L.; Petersson, G. A.; Barnes, E. C.; Frisch, M. J.; Montgomery, J. A. A Restricted-Open-Shell Complete-Basis-Set Model Chemistry. *J. Chem. Phys.* **2006**, *125* (9), 094106–094122.

(99) DeYonker, N. J.; Grimes, T.; Yockel, S.; Dinescu, A.; Mintz, B.; Cundari, T. R.; Wilson, A. K. The Correlation-Consistent Composite Approach: Application to the G3/99 Test Set. *J. Chem. Phys.* **2006**, *125*, 104111–104115.

(100) DeYonker, N. J.; Cundari, T. R.; Wilson, A. K. The Correlation Consistent Composite Approach (ccCA): An Alternative to the Gaussian-N Methods. *J. Chem. Phys.* **2006**, *124*,

114104–114121.

(101) DeYonker, N. J.; Cundari, T. R.; Wilson, A. K.; Sood, C. A.; Magers, D. H. Computation of Gas-Phase Enthalpies of Formation with Chemical Accuracy: The Curious Case of 3-Nitroaniline. *J. Mol. Struct. THEOCHEM* **2006**, *775* (1–3), 77–80.

(102) DeYonker, N. J.; Mintz, B.; Cundari, T. R.; Wilson, A. K. Application of the Correlation Consistent Composite Approach (ccCA) to Third-Row (Ga−Kr) Molecules. *J. Chem. Theory Comput.* **2008**, *4* (2), 328–334.

(103) DeYonker, N. J.; Wilson, B. R.; Pierpont, A. W.; Cundari, T. R.; Wilson, A. K. Towards the Intrinsic Error of the Correlation Consistent Composite Approach (ccCA). *Mol. Phys.* **2009**, *107* (8–12), 1107–1121.

(104) Grimes, T. V; Wilson, A. K.; DeYonker, N. J.; Cundari, T. R. Performance of the Correlation Consistent Composite Approach for Transition States: A Comparison to G3B Theory. *J. Chem. Phys.* **2007**, *127* (15), 154117–154125.

(105) Prascher, B. P.; Lai, J. D.; Wilson, A. K. The Resolution of the Identity Approximation Applied to the Correlation Consistent Composite Approach. *J. Chem. Phys.* **2009**, *131* (4), 044130–044142.

(106) Oyedepo, G. A.; Wilson, A. K. Multireference Correlation Consistent Composite Approach [MR-ccCA]: Toward Accurate Prediction of the Energetics of Excited and Transition State Chemistry. *J. Phys. Chem. A* **2010**, *114* (33), 8806–8816.

(107) Das, S. R.; Williams, T. G.; Drummond, M. L.; Wilson, A. K. A QM/QM Multilayer Composite Methodology: The ONIOM Correlation Consistent Composite Approach (ONIOM-ccCA). *J. Phys. Chem. A* **2010**, *114* (34), 9394–9397.

(108) Laury, M. L.; DeYonker, N. J.; Jiang, W.; Wilson, A. K. A Pseudopotential-Based Composite Method: The Relativistic Pseudopotential Correlation Consistent Composite Approach for Molecules Containing 4d Transition Metals (Y–Cd). *J. Chem. Phys.* **2011**, *135* (21), 214103–214113.

(109) Mahler, A.; Wilson, A. K. Explicitly Correlated Methods within the ccCA Methodology. *J. Chem. Theory Comput.* **2013**, *9* (3), 1402–1407.

(110) Riojas, A. G.; Wilson, A. K. Solv-ccCA: Implicit Solvation and the Correlation Consistent Composite Approach for the Determination of pKa. *J. Chem. Theory Comput.* **2014**, *10* (4), 1500–1510.

(111) Henry, D. J.; Sullivan, M. B.; Radom, L. G3-RAD and G3X-RAD: Modified Gaussian-3

(G3) and Gaussian-3X (G3X) Procedures for Radical Thermochemistry. *J. Chem. Phys.* **2003**, *118* (11), 4849–4860.

(112) Pople, J. A.; Head□Gordon, M.; Raghavachari, K. Quadratic Configuration Interaction. A General Technique for Determining Electron Correlation Energies. *J. Chem. Phys.* **1987**, *87* (10), 5968–5975.

(113) Feller, D. Application of Systematic Sequences of Wave Functions to the Water Dimer. *J. Chem. Phys.* **1992**, *96* (8), 6104–6114.

(114) Feller, D. The Use of Systematic Sequences of Wave Functions for Estimating the Complete Basis Set, Full Configuration Interaction Limit in Water. *J. Chem. Phys.* **1993**, *98* (9), 7059–7071.

(115) Jiang, W.; DeYonker, N. J.; Determan, J. J.; Wilson, A. K. Toward Accurate Theoretical Thermochemistry of First Row Transition Metal Complexes. *J. Phys. Chem. A* **2012**, *116* (2), 870–885.

CHAPTER 3 DFT AND *AB INITIO* COMPOSITE METHODS: INVESTIGATION OF OXYGEN FLUORIDE SPECIES[1]

3.1 Introduction

The oxygen fluorides have attracted interest because they can be employed as propellants in the rocket industry and can be used as strong fluorinating and oxidizing agents. In addition, oxygen fluorides play a role as intermediates in atmospheric chemistry and are believed to make a minor contribution to the destruction of ozone.[1-6] The source of fluorine in the atmosphere originates from the decomposition of chlorofluorocarbons (CFCs) and their radical fragments, but most of the atmospheric fluorine is in the form of hydrogen fluoride (HF). Hydrogen fluoride is formed from the fast reaction of a fluorine atom with methane and water vapor.[5,7] Although the role of fluorine in ozone depletion is minor, the percentage of fluorine in the atmosphere has been reported to be increasing with time.[8-10] Thus, accurate thermochemical properties are required for modeling fluorine compounds in the study of atmospheric reactions. Due to the unstable nature of oxygen fluorides, experimental measurements of the energetic properties have been limited. Computational approaches can aid in understanding such systems.

Investigating the structural properties of the oxygen fluorides has been a challenge to the computational chemical community, particularly for FOO and FOOF. The F-O bond in oxygen fluorides is a covalent bond between two highly electronegative atoms where both atoms contain lone pair electrons. Therefore, the F-O bond exhibits strong electron lone pair – lone pair repulsion and can become very long in molecules such as FOO and FOOF (~0.2 Å longer than the F-O bond in FOF),[11,12] requiring consideration of high-level electron correlation methods. In FOO and FOOF, the O-O bond length is similar to that in the O_2 molecule but ~0.2 Å shorter

[1] This entire chapter has reprinted from Z. H. A. Alsunaidi, and A. K. Wilson, "DFT and *ab initio* composite methods: Investigation of oxygen fluoride species" *Computational and Theoretical Chemistry.* **2016**, 1095, 71-82, with permission of Elsevier.

than the O-O bond length in HOOH.[11] The unusual geometry of FOO and FOOF presented a computational difficulty for electronic structure methods, which led to numerous investigations of oxygen fluorides using a variety of methods to study their structures and energetic properties.[13-10] Many methods have been unsuccessful in predicting the right structure for oxygen fluorides, such as FOO, FOOO, and FOOF, with respect to the experimental geometries, as will be seen in the following sections.

As a full literature review of these efforts is outside the scope of this paper, a number of significant and recent investigations are highlighted. The FOO structure and enthalpy of formation ($\Delta H°_{f,\,298}$) have been computed by Francisco et al.[16] using Møller-Plesset perturbation theory (MP2, MP3, and MP4), complete active space self-consistent field (CASSCF), and quadratic configuration interaction [QCISD(T)] in conjunction with Pople's basis sets. The study found that all MP*n* methods underestimated the F-O bond length by > 0.2 Å. QCISD(T)/6-31G(d) yielded the best FO bond length that is only shorter by 0.002 Å from the experimental length (expt. r_e (F-O) = 1.649 ± 0.013 Å,[31] where r_e indicates an equilibrium structure), whereas the best CASSCF description of the F-O bond length is 0.8 Å shorter than experiment. Francisco's study reported an enthalpy of formation at 0 K for FOO of 8.9 ± 3 kcal mol^{-1} by using isodesmic and isogyric reaction schemes using QCISD(T)/6-311G(d,p) results.[16] Ventura and Kieninger's[26] study on FOO concluded that B3LYP/6-311++G(3df, 3pd) is a reliable method to describe structures and predict reaction enthalpies for molecules involving F-O bonds. Studies by Denis[30,32,33] found that the inclusion of the full treatment of the triple excitation [CCSDT instead of CCSD(T)] overcame the spin contamination problem presented in UCCSD(T), hence CCSDT predicted an accurate structure and energetics of the FOO molecule. Karton et al.[20] reported the $\Delta H°_{f,\,298}$ of FOO of 5.87 ± 0.16 kcal mol^{-1} in excellent agreement with experiment

(6.1 ± 0.5 kcal mol^{-1}) using the high-level computationally demanding W4 method.[34] A recent theoretical study by Feller et al.[15] obtained a correct structure of FOO using R/UCCSD(T)/aug-cc-pVTZ level of theory and with a calculated value of $\Delta H°_{f,\,298}$ of 6.4 ± 0.7 kcal mol^{-1} using a composite approach that is based on coupled cluster theory with up to quadruple excitations. The difference in the uncertainties estimated by Karton (5.87 ± 0.16 kcal mol^{-1})[20] and Feller (6.4 ± 0.7 kcal mol^{-1})[15] imputes to their different approaches. While W4 estimates uncertainties based on the performance of a set of 25 small molecules,[20] Feller's approach uses molecule-by-molecule criteria to calculate the estimated uncertainties.[15]

The structure and the $\Delta H°_{f,\,298}$ of FOOF have been studied extensively with a broad variety of quantum chemical methods. The computational challenge in the FOOF structure arises from the anomeric delocalization effect that exists in FOOF between the oxygen lone pair and the antibonding orbital of the F-O bond.[29] Although CCSD(T)/aug-cc-pVTZ[15] and B3LYP/6-311++G(2d)[18] can provide a qualitatively correct geometry for FOOF, very few methods used in previous work reproduced the experimental FOOF structure. In fact, a local density functional (LDF) paired with numerical and Gaussian basis sets[35] and the local SVWN functional paired with 6-311++G(2d)[18] were two methods that predicted the closest r_e of the F-O bond compared to experiment, with LDF being superior. LDF predicted F-O and O-O bond lengths that are 0.01 Å and 0.001 Å off from experimental geometries (r_s(F-O) =1.575 ± 0.003 Å and r_s(O-O) = 1.217 ± 0.003 Å),[11] respectively. LDF predicted this good description for FOOF likely due to the high and evenly distributed electron density in FOOF, as justified in Ref. 34. MP2, MP3, and MP4 with different size and type of basis sets, on the other hand, predicted incorrect geometries for FOOF with respect to experiment, however MP6 at the complete basis set (CBS) limit predicted an accurate geometry.[29] Not only is the structure of FOOF problematic but its $\Delta H°_{f,\,298}$ has also

been difficult to predict. The calculated $\Delta H°_{f,\ 298}$ of FOOF using even high-level *ab initio* methods has a large deviation from the experimental value reported in the NIST-JANAF thermochemical table (4.6 ± 0.5 kcal mol^{-1}).[36-37] The $\Delta H°_{f,\ 298}$'s reported by Karton et al.[20] is 7.84 ± 0.18 kcal mol^{-1} and 8.21 ± 0.18 kcal mol^{-1} using W4 energies at the CCSD(T)/cc-pVQZ and experimental geometries, respectively. The most recent value of the $\Delta H°_{f,\ 298}$ of FOOF is 6.4 ± 0.7 kcal mol^{-1} and was calculated using a coupled cluster-base composite approach.[15] These are only a few examples of this large deviation from experiment.

Predicting the conformational structure of FOOO has also been challenging. Frecer et al.[38] investigated the FOOO that formed by F + O_3 reaction and found that $FO(O)_2$ is the most stable structure with F-O being a weak bond (3.671 Å). However, FOOO was observed later as a stabilized intermediate in dilute mixtures of F_2 and O_3 in solid argon by FT-IR spectroscopy.[39] Based on the reported frequencies of FOOO, it is characterized as a FO-O_2 complex, and it cannot be a weak van der Waals complex,[39] which differs from Frecer's stable structure,[38] mentioned above. Quantum chemical studies by Li et al.[40] and Peiró-García et al.[41] of the F + O_3 reaction mechanisms using MP2/6-31G(d) and QCISD/6-311+G(d,p), respectively, also could not predict the FOOO ground state complex observed experimentally in the argon matrix.[39] A geometry optimization and frequency calculations of FOOO were performed by Roohi et al.[25] at the CCSD/aug-cc-pVDZ, CCSD/6-311+G(d), and QCISD/aug-cc-pVDZ levels of theory. Roohi's study[25] showed that the planar FOOO with dihedral angle of 0.0° is the most stable structure, with its calculated frequencies agreeing well with the reported experimental frequencies.[39] No $\Delta H°_{f,\ 298}$ for FOOO has been previously reported, to our knowledge. The structure of the corresponding hydride FOOOH has only been studied previously by MINDO[42] and by MP2/6-3lG(d).[43] As MP2 theory has encountered difficulty for calculating the F-O and

the O-O bond lengths, an additional investigation of the FOOOH structure has to be done.

While methods such as CCSDT and QCISD are computationally demanding, *ab initio* composite methods have been developed to circumvent the computational demands of such methods. One such approach, the correlation consistent Composite Approach (ccCA)[44-46], is a method that has been demonstrated to be practical and reliable for the prediction of thermochemical properties, such as enthalpies of formation, ionization potentials, and electron affinities. The targeted accuracy of ccCA for main group molecules is to yield a mean absolute deviation of approximate chemical accuracy, 1 kcal mol^{-1} at reduced computational cost. This is in contrast to coupled cluster-based composite methods, which generally strive for a chemical accuracy of ± 0.24 kcal mol^{-1}, such as the W4 composite method and the approach used by Feller et al.[15] Because the performance of ccCA for a variety of halogen oxides and their related hydrides has not been examined in detail, it is of our interest to consider the utility of ccCA in describing oxygen fluorides, such as FOO, FOOF, and FOOO.

Density functionals provide another option, as, overall, functionals have a lower formal computational scaling than post-HF methods such as CCSD(T) and CCSDT, though DFT predictions such as for enthalpies of formation, in general, do not reach the accuracies achievable by composite methods, such as ccCA. Thus, they are system dependent methods and are worth considering for each system. For example, the Minnesota density functionals M06[47] and M06-2X[47] were used by Meyer and Kass,[48] in conjunction with the correlation consistent basis sets[49-51] to assess their performance for predicting the $\Delta H°_{f,\,298}$'s of a set of chlorine oxides and related hydrides (ClO_x and ClO_xH, where x =1-4) with respect to the $\Delta H°_{f,\,298}$'s of W4 method.[34] The capability of G3[52] and G3B3[53] for calculating $\Delta H°_{f,\,298}$'s of chlorine oxides were also investigated in the same study.[48] The main findings from the Meyer and Kass study are that M06

$\Delta H°_{f,\,298}$'s were found to differ by an average of 1.3 kcal mol^{-1} from the W4 $\Delta H°_{f,\,298}$'s, while M06-2X resulted in larger error (6.2 kcal mol^{-1}). G3 and G3B3 $\Delta H°_{f,\,298}$'s yielded an average error of 4.6 kcal mol^{-1} and 6.5 kcal mol^{-1}, respectively. The author attributed the large errors of G3 and G3B3 $\Delta H°_{f,\,298}$'s to their poor predicted geometries. Although M06 and M06-2X functionals were examined for the prediction of the $\Delta H°_{f,\,298}$'s of chlorine oxides, the capability of M06 and M06-2X to predict structures and $\Delta H°_{f,\,298}$'s has not been assessed for other halogen oxides. Thus, it is of interest to evaluate these functionals for oxygen fluoride species, as well as examine the performance of G3 and G3B3 methods for these systems. G3 and G3B3 are used here, largely, as they were included in the Meyer and Kass study.[48] Though G4 is a more modern method, beginning with an MP4 reference energy is a costly start, and as shown in previous studies, G4 predicts very similar energies as G3.[54-55]

In the present study, the reliability of ccCA, G3, and G3B3 for the prediction of the $\Delta H°_{f,\,298}$'s of oxygen fluoride species was evaluated. In addition to these composite methods, the performance of M06 and M06-2X was also examined for predicting the structures and enthalpies of formation of oxygen fluoride species. A set of various oxygen fluorides were considered in this study, including FO, FOO, FOOO, and the related hydrides (FOH, FOOH, and FOOOH) and difluorides (FOF, FOOF, and FOOOF), where the $\Delta H°_{f,\,298}$'s of FOOO and FOOOH have not been reported previously. The effects of basis set size and spin contamination were also considered. For comparison, the $\Delta H°_{f,\,298}$'s of chlorine oxides and related hydrides have been provided, whereas full theoretical investigations for chlorine oxides and related hydrides can be found in the Meyer and Kass study and references therein.[48]

3.2 Computational Methodology

All calculations were performed using the Gaussian 09 software package.[56] The hybrid-meta-generalized gradient approximation (HMGGA) Minnesota functionals (M06[47] and M06-2X)[47] in conjunction with the augmented correlation consistent polarized valence basis sets (aug-cc-pV*n*Z), where *n* = D, T, Q,[49-51] were used to optimize the structures of all molecules under investigation. The tight-*d* correlation consistent basis set of Dunning et al.,[57] aug-cc-pV(*n*+*d*)Z, where *n* = D, T, Q, were used for chlorine. Frequency calculations were performed to ensure that the structure is a stationary point. The enthalpies of formation for these structures were determined at the same level of theory.

ccCA, G3, and G3B3, were also applied to predict the enthalpies of formation. In ccCA, geometry optimization and vibrational frequencies calculations are performed using B3LYP/aug-cc-pVTZ.[44] The harmonic vibrational frequencies are then corrected using a scale factor of 0.989 as recommended in Ref. 44. The remaining steps in ccCA involve a series of single point energy calculations performed using the B3LYP/aug-cc-pVTZ geometry (for details see Chapter2 Section 2.5.2). Several variants of ccCA can be used, which vary by the means used to extrapolate the MP2 energy (MP2/aug-cc-pV∞Z) to the CBS limit.[44] ccCA-S3 and ccCA-S4 utilize Schwartz's inverse cubic and quartic extrapolation scheme, respectively.[58] ccCA-P utilizes Peterson's mixed Gaussian/exponential extrapolation scheme[59] and ccCA-PS3 is an average of ccCA-P and ccCA-S3. G3[52] and G3B3[53] both are composite methods that involve the same series of single point energy calculations though based upon different geometries (see Chapter 2 Section 2.5.1). The geometry optimization in G3 is at the MP2(full)/6-31G(d) level of theory, while G3B3 uses the B3LYP/6-31G(d) level of theory.

For open-shell systems (radicals) such as FOO and FOOO, which show a degree of spin contamination, restricted open shell (RO) calculations are used, i.e. ROM06, ROM06-2X. In addition, RO-ccCA[60] and G3-RAD[61] energies were obtained and used to calculate their $\Delta H°_{f,\,298}$'s. Gaussian 09[56] was used to determine these energies. The mean absolute deviations (MADs) of the calculated $\Delta H°_{f,\,298}$'s were determined for all of the utilized methods with respect to the experimental values, unless otherwise noted.

3.3 Results and Discussion

3.3.1 Structures

The structural parameters obtained by M06 and M06-2X for all of the species are listed in Table 3.1. The optimized structures at the B3LYP/aug-cc-pVTZ, MP2(full)/6-31G(d), and B3LYP/6-31G(d) levels, which are used for geometry optimizations in ccCA, G3, and G3B3, respectively, were also considered (shown in Table 3.1). Experimental structural parameters of FO,[22] FOO,[31] FOF,[12] FOOF,[11] and FOH,[17] have been reported and were utilized as reference data to determine the performance of the considered methods. To the authors' knowledge no experimental observations have been reported for the geometric parameters of FOOH, FOOO, and FOOOF. Thus, for these molecules theoretical results from rigorous methods such as coupled cluster are presented to calibrate the considered methods (CCSD(T)/TZ2P structure for FOOH,[21] CCSD/6-311+G(d) structure for FOOO,[25] and CCSD(T)/cc-pVTZ for FOOOF).[19]

Table 3.1 Structural parameters of the oxygen fluoride species at different level of theories, bond lengths are in angstroms and bond angles and dihedral angles in degree.

FO			
Method/Basis set	*r* (FO)		
M06/aug-cc-pVDZ	1.332		
M06/aug-cc-pVTZ	1.328		
M06/aug-cc-pVQZ	1.324		
M062X/aug-cc-pVDZ	1.329		
M062X/aug-cc-pVTZ	1.329		
M062X/aug-cc-pVQZ	1.325		
B3LYP/aug-cc-pVTZ	1.351		
B3LYP/6-31g(d)	1.354		
MP2(full)/6-31g(d)	1.344		
Experiment[a]	1.354		
FOH			
Method/Basis set	*r* (FO)	*r* (OH)	*a* (FOH)
M06/aug-cc-pVDZ	1.408	0.973	99.1
M06/aug-cc-pVTZ	1.405	0.969	99.2
M06/aug-cc-pVQZ	1.401	0.966	99.3
M062X/aug-cc-pVDZ	1.401	0.971	99.3
M062X/aug-cc-pVTZ	1.400	0.968	99.4
M062X/aug-cc-pVQZ	1.397	0.967	99.5
B3LYP/aug-cc-pVTZ	1.430	0.971	98.6
B3LYP/6-31g(d)	1.434	0.977	97.8
MP2(full)/6-31g(d)	1.444	0.979	97.1
Experiment[b]	1.4350 ± 0.0031	0.9657 ± 0.0016	97.54 ± 0.50
FOF			
Method/Basis set	*r* (FO)	*a* (FOF)	
M06/aug-cc-pVDZ	1.380	103.5	
M06/aug-cc-pVTZ	1.377	103.6	
M06/aug-cc-pVQZ	1.374	103.7	
M062X/aug-cc-pVDZ	1.376	102.9	
M062X/aug-cc-pVTZ	1.374	103.0	

Table 3.1 Continued.

M062X/aug-cc-pVQZ	1.371	103.1
B3LYP/aug-cc-pVTZ	1.403	103.9
B3LYP/6-31g(d)	1.409	103.9
MP2(full)/6-31g(d)	1.423	102.6
Experiment[c]	1.412	103.1

FOO

Method/Basis set	*r* (FO)	*r* (OO)	*a* (FOO)
M06/aug-cc-pVDZ	1.811	1.177	110.7
M06/aug-cc-pVTZ	1.752	1.171	110.6
M06/aug-cc-pVQZ	1.747	1.170	110.7
ROM06/aug-cc-pVDZ	1.589	1.182	110.6
ROM06/aug-cc-pVTZ	1.580	1.178	110.6
ROM06/aug-cc-pVQZ	1.572	1.178	110.7
M062X/aug-cc-pVDZ	2.090	1.184	111.2
M062X/aug-cc-pVTZ	1.520	1.190	110.0
M062X/aug-cc-pVQZ	1.519	1.187	110.1
ROM062X/aug-cc-pVDZ	1.508	1.194	109.9
ROM062X/aug-cc-pVTZ	1.500	1.194	110.0
ROM062X/aug-cc-pVQZ	1.500	1.191	110.1
B3LYP/aug-cc-pVTZ	1.618	1.188	111.2
B3LYP/6-31g(d)	1.571	1.211	111.0
MP2(full)/6-31g(d)	-	-	-
Experiment[d]	1.649±0.013	1.200±0.013	111.2±0.36

FOOH

Method/Basis set	*r* (FO)	*r* (OO)	*r* (OH)	*a* (FOO)	*a* (OOH)	*d*(FOOH)
M06/aug-cc-pVDZ	1.447	1.343	0.977	105.9	104.0	85.5
M06/aug-cc-pVTZ	1.438	1.346	0.972	105.9	103.9	85.2
M06/aug-cc-pVQZ	1.434	1.343	0.970	106.0	104.0	85.4
M062X/aug-cc-pVDZ	1.419	1.358	0.973	105.3	103.6	84.6
M062X/aug-cc-pVTZ	1.415	1.361	0.970	105.4	103.6	84.6
M062X/aug-cc-pVQZ	1.412	1.357	0.968	105.5	103.7	84.7
B3LYP/aug-cc-pVTZ	1.470	1.365	0.974	106.3	103.7	85.0
B3LYP/6-31g(d)	1.465	1.376	0.981	106.1	102.9	83.1

Table 3.1 Continued.

MP2(full)/6-31g(d)	1.468	1.39	0.981	105.0	102.0	83.1
CCSD(T)/TP2Z[e]	1.481	1.393	0.969	105.4	101.9	84.5

FOOF

Method/Basis set	*r* (FO)	*r* (OO)	*a* (FOO)	*d* (FOOF)
M06/aug-cc-pVDZ	1.506	1.217	108.6	87.2
M06/aug-cc-pVTZ	1.494	1.219	108.5	86.9
M06/aug-cc-pVQZ	1.485	1.221	108.6	87.0
M062X/aug-cc-pVDZ	1.426	1.285	106.6	85.9
M062X/aug-cc-pVTZ	1.420	1.289	106.7	85.7
M062X/aug-cc-pVQZ	1.419	1.286	106.8	85.8
B3LYP/aug-cc-pVTZ	1.523	1.227	109.3	88.1
B3LYP/6-31g(d)	1.497	1.266	108.3	86.7
MP2(full)/6-31g(d)	1.496	1.291	106.9	85.8
Experiment[f]	1.575±0.003	1.217±0.003	109.5±0.5	87±0.5

FOOO

Method/Basis set	*r* (FO)	*r* (FO-O), *r* (FOO-O)	*a* (FOO), *a* (OOO)	*d* (FOOO)
M06/aug-cc-pVDZ	1.338	2.469, 1.196	97.8, 110.8	0.0
M06/aug-cc-pVTZ	1.335	2.408, 1.191	93.0, 106.5	0.0
M06/aug-cc-pVQZ	1.331	2.449, 1.189	92.4, 105.9	0.0
ROM06/aug-cc-pVDZ	1.357	1.704, 1.192	100.2, 110.1	0.0
ROM06/aug-cc-pVTZ	1.354	1.687, 1.189	100.9, 110.5	0.0
ROM06/aug-cc-pVQZ	1.350	1.681, 1.188	101.1, 110.7	0.0
M062X/aug-cc-pVDZ	1.331	2.598, 1.191	88.5, 103.4	0.0
M062X/aug-cc-pVTZ	1.333	2.537, 1.187	90.4, 105.6	0.0
M062X/aug-cc-pVQZ	1.327	2.702, 1.187	91.0, 107.8	0.0
ROM062X/aug-cc-pVDZ	1.360	1.589, 1.204	103.3, 112.1	0.0
ROM062X/aug-cc-pVTZ	1.359	1.575, 1.205	103.9, 112.4	0.0
ROM062X/aug-cc-pVQZ	1.356	1.573, 1.203	104.0, 112.5	0.0
B3LYP/aug-cc-pVTZ	1.354	2.715, 1.204	101.1, 113.8	0.0
B3LYP/6-31g(d)	1.360	2.504, 1.211	91.0, 103.3	0.0
ROB3LYP/aug-cc-pVTZ	1.379	1.709, 1.201	101.2, 111.2	0.0
ROB3LYP/6-31g(d)	1.380	1.710, 1.214	100.3, 110.2	0.0

Table 3.1 Continued.

MP2(full)/6-31g(d)	-	-		-		-
CCSD/6-311+G(d)[g]	1.378	1.745, 1.200		100.5, 111.5		0.0
			FOOOH			
Method/Basis set	*r* (FO)	*r* (FO-O), *r* (O-OH)	*r* (OH)	*a* (FOO), *a* (OOO), *a* (OOH)	*d* (FOOO)	*d* (OOOH)
M06/aug-cc-pVDZ	1.483	1.290, 1.427	0.974	106.5, 109.0, 101.1	-85.8	91.7
M06/aug-cc-pVTZ	1.471	1.292, 1.428	0.970	106.5, 109.0, 101.1	-85.7	91.4
M06/aug-cc-pVQZ	1.466	1.291, 1.424	0.968	106.6, 109.1, 101.2	-85.6	91.8
M062X/aug-cc-pVDZ	1.427	1.331, 1.406	0.972	105.3, 107.9, 101.8	-84.0	91.4
M062X/aug-cc-pVTZ	1.423	1.333, 1.407	0.967	105.5, 108.1, 102,1	-84.0	90.1
M062X/aug-cc-pVQZ	1.421	1.330, 1.403	0.968	105.6, 108.2, 102.2	-83.9	90.3
B3LYP/aug-cc-pVTZ	1.502	1.303, 1.461	0.972	107.3, 109.6, 100.7	-87.4	96.0
B3LYP/6-31g(d)	1.485	1.331, 1.454	0.979	106.3, 108.8, 99.9	-84.9	89.0
MP2(full)/6-31g(d)	1.481	1.358, 1.450	0.981	104.9, 107.5, 99.7	-83.2	87.0
			FOOOF			
Method/Basis set	*r* (FO)	*r* (OO)		*a* (FOO), *a* (OOO)	*d* (FOOO)	
M06/aug-cc-pVDZ	1.419	1.355		106.2, 109.0	± 93.0	
M06/aug-cc-pVTZ	1.413	1.355		106.2, 109.1	±92.5	
M06/aug-cc-pVQZ	1.410	1.353		106.3, 109.2	±92.4	
M062X/aug-cc-pVDZ	1.403	1.360		105.3, 108.1	±90.9	
M062X/aug-cc-pVTZ	1.400	1.360		105.7, 108.3	±90.8	
M062X/aug-cc-pVQZ	1.399	1.357		105.7, 108.5	±91.0	
B3LYP/aug-cc-pVTZ	1.440	1.377		106.6, 109.3	±93.6	
B3LYP/6-31g(d)	1.440	1.386		105.8, 108.7	±90.5	
MP2(full)/6-31g(d)	1.365	1.340		105.6, 108.2	±90.1	
CCSD(T)/cc-pVTZ[h]	1.444	1.385		105.5, 108.3	±91.3	

[a]Reference 22. [b]Reference 17. [c]Reference 12. [d]Reference 31. [e]CCSD(T)/TZ2P: Reference 21. [f]Reference 11. [g]CCSD/6-311+G(d): Reference25. [h]CCSD(T)/cc-pVTZ: Reference 19.

The F-O bond length calculated by M06 and M06-2X for all set of molecules showed a systematic decrease in length when using the correlation consistent basis set family going from aug-cc-pVDZ, aug-cc-pVTZ, to aug-cc-pVQZ (Table 3.1). However, this decrease in the bond length while increasing basis set size does not occur for the O-O bond length as shown in Table 3.1, and can be dependent on the density functional being utilized. Both M06 and M06-2X underestimated the F-O and O-O bond lengths with respect to the corresponding experimental values. M06-2X predicted shorter F-O bond lengths and longer FO-O bond lengths than M06. The average difference between the aug-cc-pVTZ F-O bond lengths and the aug-cc-pVQZ F-O bond lengths is 0.005 Å for M06 and it is 0.002 Å for M06-2X, and for the FO-O bond length it is 0.003 Å for both functionals whereas the aug-cc-pVDZ bond lengths are generally longer. Yet, the M06/aug-cc-pVDZ and M06-2X/aug-cc-pVDZ predicted the closest geometries to the reference data with average errors in the F-O bond length of 0.032 Å and 0.062 Å, respectively. Thus, increasing the basis set size will not always give the better structures for the systems under investigation. For open-shell species, such as FO, FOO, and FOOO, the degree of spin contamination resulting from the mixing of higher spin states into the wavefunction was calculated, as high spin contamination results in incorrect geometries and energies. Previous studies showed a high degree of spin contamination when studying FOO using other methods, such as MP2.[16,26] No spin contamination was found when calculating FO, but it was present when calculating FOO and FOOO. The expectation values of the total spin, $\langle S^2 \rangle$, are listed in Table 3.2, where the optimal value for these radicals is $\langle S^2 \rangle = 0.75$. The effect of spin contamination becomes appreciable as the deviation of $\langle S^2 \rangle$ from 0.75 increases, and this deviation decreases with increasing the size of the basis sets, as shown in Table 3.2. Both UM06 and UM06-2X suffer from spin contamination associated with FOO (small) and FOOO (severe),

as shown in Table 3.2. This error was corrected by using the restricted open-shell density functionals as shown in Table 3.1. ROM06 and ROM06-2X provided better structural parameters with respect to the reference data for FOO and FOOO than what UM06 and UM062X predicted. Thus, the ROM06 and ROM06-2X geometries were used later to calculate the enthalpies of formation. FOOOF was found to exist in two conformers. Both have very similar geometries but differ in the dihedral angles. One conformer has *d*(OOOF) = 91.3° and the other one has *d*(OOOF) = 82.0°.[19] Because the energy difference between the two conformers at the CCSD(T)/cc-pVTZ level is very small, 0.24 kcal mol^{-1}, with the *d*(OOOF) = 82.0° conformer having the lowest energy,[19] only one conformer was included in the molecule test set. M06-2X described the structure of FOOOF better than M06 when compared to the CCSD(T) structure. Overall the geometries predicted by M06 are in better agreement with the reference data than M06-2X, although both functionals generally underestimated the F-O and the O-O bond lengths. Thus, for this set of molecules, doubling the amount of Hartree-Fock exchange from M06 to M06-2X does not improve the results.

As shown in Table 3.1, the F-O bond lengths obtained by B3LYP/aug-cc-pVTZ are in very good agreement (MAD of 0.01 Å) with respect to the reference data, with the exception of the F-O bond distance(s) in FOO and FOOF. The difference in F-O bond lengths is more than 0.01 Å (0.018 Å in FOO and 0.049 Å in FOOF) compared to experimental values. Although B3LYP/aug-cc-pVTZ did not predict very accurate bond lengths for FOO and FOOF, it provided a qualitatively correct description of the structures of these two molecules. The capability of B3LYP to describe the geometries has been noticed previously for some of the oxygen fluorides.[26,35] Quite similarly, the calculated F-O bond lengths at the B3LYP/6-31G(d) level were in very good agreement with respect to the reference data; however, not only is the F-O bond

length underestimated in FOO and in FOOF (by 0.065 Å in FOO and 0.075 Å in FOOF), but also the F-O bond distance in FOOH was underestimated by about 0.016 Å using B3LYP/6-31G(d) in

Table 3.2 The expectation value of the total spin $<S^2>$.

Molecule	**Method/Basis set**	**$<S^2>$**
FOO	M06/aug-cc-pVDZ	0.756
	M06/aug-cc-pVTZ	0.754
	M06/aug-cc-pVQZ	0.754
	M062X/aug-cc-pVDZ	0.782
	M062X/aug-cc-pVTZ	0.750
	M062X/aug-cc-pVQZ	0.75
	B3LYP/aug-cc-pVTZ	0.75
	B3LYP/6-31g(d)	0.7509
FOOO	M06/aug-cc-pVDZ	0.892
	M06/aug-cc-pVTZ	0.782
	M06/aug-cc-pVQZ	0.782
	M062X/aug-cc-pVDZ	0.803
	M062X/aug-cc-pVTZ	0.780
	M062X/aug-cc-pVQZ	0.807
	B3LYP/aug-cc-pVTZ	0.790
	B3LYP/6-31g(d)	0.776

comparison to the reference data. Additionally, when using the 6-31G(d) basis set, the average error for B3LYP increased from 0.01 Å (obtained when using an aug-cc-pVTZ basis set) to 0.02 Å. Thus, again B3LYP with the small basis set 6-31G(d) is not enough to describe peroxide systems, such as FOO, FOOF, and FOOH. B3LYP in conjunction with aug-cc-pVTZ also resulted in the least average error of 0.01 Å (from the reference data) for the O-O bond length compared to other methods. The effect of spin contamination for open shell systems using UB3LYP has been tested and the total spin operators $<S^2>$ are presented in Table 3.2, for each level of theory. The $<S^2>$ values for FOO show that the use of UB3LYP at either basis set levels

does not result in spin contamination, whereas for FOOO, both UB3LYP/aug-cc-pVTZ and UB3LYP/6-31G(d) levels resulted in large deviation from the optimal value $\langle S^2 \rangle = 0.75$. Consequently, the ROB3LYP is used to predict the geometry for FOOO, which is in agreement with the structure predicted by CCSD,[25] as shown in Table 3.1. For FOOOF, B3LYP was able to predict the two conformers with *d*(OOOF) = 91.3° and with *d*(OOOF) = 82.0° and the B3LYP F-O and O-O bond lengths agree well with the CCSD(T) bond lengths.

The predicted geometries for FOF, FOH, and FOOH by MP2(full)/6-31g(d) agree well with the reference data within a 0.01 Å difference. However, MP2(full)/6-31g(d) predicted a 0.1 Å shorter F-O bond and a 0.1 Å longer O-O bond for FOOF compared to experimental bond lengths, this large difference in the bond lengths was also found previously using MP2/6-31g**.[43] Likewise, the F-O and O-O bond lengths predicted by MP2(full)/6-31g(d) for FOOOF are 0.08 Å and 0.05 Å shorter than CCSD(T) results, indicating that this level of theory is not enough to describe the peroxide's geometry. For the open-shell systems FOO and FOOO, the UMP2 method could not provide converged geometries due to large spin contamination.

As mentioned earlier for FOOOH, no reliable theoretical or experimental geometries have been reported. Based on the success of B3LYP/aug-cc-pVTZ method in predicting the FOOOF geometry compared to the CCSD(T)/cc-pVTZ, the B3LYP/aug-cc-pVTZ geometry for FOOOH is considered as the most reliable structure. For this compound, only one conformer *d*(FOOO) = -87.4°) is found to be a stable structure. The B3LYP/6-31G(d) structure of FOOOH is quite similar to the structure at the B3LYP/aug-cc-pVTZ level, with a large difference of 0.03 Å in the FO-O bond length. M06 and M06-2X generally underestimated the bond lengths of

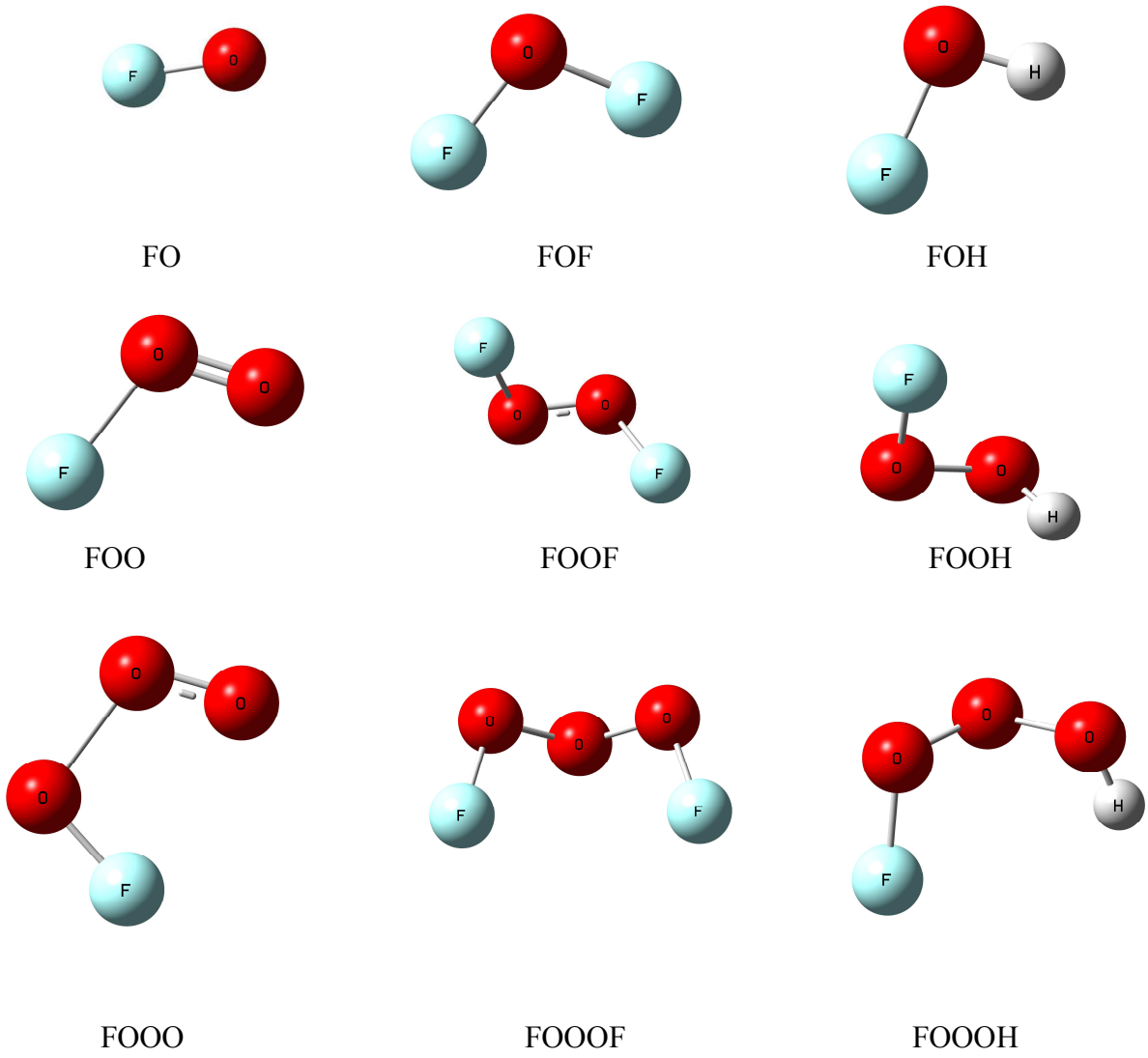

Figure 3.1 B3LYP/aug-cc-pVTZ structures of the oxygen fluoride species included in this study.

FOOOH as compared to the B3LYP/aug-cc-pVTZ geometries. MP2 (full)/6-31g(d) predicted shorter F-O bond length and longer FO-O bond length than the B3LYP/aug-cc-pVTZ.

As a result of the above discussion, M06 and M06-2X are not recommended methods for predicting the geometries of oxygen fluorides and related hydrides and difluorides. MP2 performed well for most of the closed-shell compounds with the exception of the peroxides. The geometries obtained by B3LYP/aug-cc-pVTZ, shown in Figure 3.1, result in the lowest deviation from the reference data among the considered methods. As shown in Figure 3.1, using B3LYP/aug-cc-pVTZ supports conclusions from previous studies[12,17,31] that FOO, FOF, and FOH are bent with bond angles of 111.2°, 103.9°, and 98.6°, respectively. Different bond angles indicate that the bond angle opens more as the repulsion between bonds increases. Similarly, FOOF and FOOH have dihedral angles of 88.2° and 85.0°, respectively, in order to minimize the repulsion between bonds. FOOOF and FOOOH display a zigzag shape with *d*(FOOO) = 93.6°, and *d*(FOOO) = -87.4°, respectively. In contrast to all the peroxide systems, the stable conformer of FOOO is when *d*(FOOO) = 0.0°. Intermolecular dispersion forces might be the cause of the stable FOOO structure.

3.3.2 Enthalpies of Formation ($\Delta H°_{f,\,298}$)

To provide a comparison between the performance of the utilized methods on chlorine oxide and oxygen fluoride species, the $\Delta H°_{f,\,298}$'s of chlorine oxides and related hydrides were determined using M06/aug-cc-pVQZ, M06-2X/aug-cc-pVQZ, ccCA-S3, G3, and G3B3 and are listed in Table 3.3 The MADs of the considered methods with respect to experiment for predicting $\Delta H°_{f,\,298}$'s are provided in Table 3.3 as well. These MADs are 1.1 (ccCA-S3), 2.1 (M06), 2.5 (M06-2X), 2.3 (G3), and 3.5 (G3B3) kcal mol^{-1}. The MAD of ccCA-S3 indicates that

ccCA is a reliable method in predicting energetics for chlorine oxides. M06 resulted in a MAD of 2.1 kcal mol^{-1} for the calculated $\Delta H°_{f,298}$'s of chlorine oxides, which is 0.9 kcal mol^{-1} greater than the MAD (1.2 kcal mol^{-1}) that resulted from the calculations done by Meyer and Kass.[48] This small difference arises from the use of a temperature correction approach that reduces the energy contributed from the low vibrational frequency modes as pointed out in Meyer and Kass study.[48,62] In the present study, however, scale factors of 0.9853 (M06) and 0.9733 (M06-2X)[63] were used for the correction of the vibrational frequencies in the computations. The $\Delta H°_{f,298}$'s calculated by M06 for chlorine oxides in the present study are in good agreement with the experimental values with the exception of ClO_3, which is known to be problematic for not only computational methods but also for experiments, as demonstrated by the error bar associated with the experimental $\Delta H°_{f,298}$ (± 3 kcal mol^{-1}),[64-66] as compared with smaller uncertainties for many main group species. Only ccCA-S3 and G3 predict the $\Delta H°_{f,298}$ of ClO_3 within the experimental uncertainty. The $\Delta H°_{f,298}$'s obtained by G3 are in relatively good agreement with the experiments (MAD = 2.3 kcal mol^{-1}), yet the ClO_2 $\Delta H°_{f,298}$ predicted by G3 overestimated the experimental value by ~4 kcal mol^{-1}. Similar to G3, M06-2X achieved a MAD of 2.5 kcal mol^{-1}, while the MAD for G3B3 was larger (MAD of 3.2 kcal mol^{-1}). Therefore, ccCA results in the lowest MAD with respect to experiment for the prediction of energetic properties of chlorine oxides, followed by M06.

Table 3.3 Enthalpies of formation for chlorine oxides and related hydrides.

Compd.	$\Delta H°_{f,\,298\,K}$ (kcal mol^{-1})					
	ccCA-S3	M06[a]	M06-2X[a]	G3	G3B3	Expt.
ClO	25.3	23.1	23.5	25.9	26.7	24.29 ±0.03[b]
ClO_2	23.9	21.2	26.8	26.8	27.6	22.6 ± 0.3[b,c]
ClO_3	44.0	40.5	50.2	48.3	51.0	46 ± 3[d]
ClO_4	57.7	52.6	65.4	66.0	65.5	-
HOCl	-19.5	-18.0	-19.3	-17.4	-16.9	-18.4 ± 0.03[e]
HOClO	3.5	4.6	6.5	6.4	7.3	-
$HOClO_2$	-2.8	-3.9	3.3	2.0	3.8	-
$HOClO_3$	-0.8	-3.4	5.5	5.6	8.7	-
MAD	1.1	2.1	2.5	2.3	3.5	-

[a]M06 and M06-2X in conjunction with aug-cc-pV(Q+d)Z for chlorine and aug-cc-pVQZ for oxygen and hydrogen. [b]Reference 70. [c]Reference 71. [d]References 64-66. [e]Reference 72.

The $\Delta H°_{f,\,298}$'s for all of the oxygen fluoride species included in this study were calculated using M06 and M06-2X in conjunction with aug-cc-pVDZ, aug-cc-pVTZ, and aug-cc-pVQZ at 298 K using the atomization energy approach and the results are shown in Table 3.4. A systematic decrease in the $\Delta H°_{f,\,298}$ values as the size of the basis set increases is observed, since the basis set with larger zeta (ξ) level recovers more energy, as shown in Table 3.4. The differences between energies determined using M06/aug-cc-pVTZ $\Delta H°_{f,\,298}$'s and those determined using M06/aug-cc-pVQZ $\Delta H°_{f,\,298}$'s is 0.1 - 1.1 kcal mol^{-1} with an average difference of 0.5 kcal mol^{-1}, whereas the differences between energies determined using M06-2X/aug-cc-pVTZ $\Delta H°_{f,\,298}$'s and those determined using M06-2X/aug-cc-pVQZ $\Delta H°_{f,\,298}$'s is 0.3 – 1.9 kcal mol^{-1} with an average difference of 1.2 kcal mol^{-1}. To evaluate the reliability of the utilized methods in calculating $\Delta H°_{f,\,298}$'s, the following reference data was used: experimental $\Delta H°_{f,\,298}$ values for FO, FOO, FOF, FOOF and FOH; the CCSD(T)/ANO4 $\Delta H°_{f,\,298}$ value for FOOH; and

the extrapolated CCSD(T)/aug-cc-pV(T,Q)Z $\Delta H°_{f,\ 298}$ value for FOOOF. For FOOO and FOOOH neither experimental nor theoretical $\Delta H°_{f,\ 298}$ values are available. The MADs of the calculated $\Delta H°_{f,\ 298}$'s with respect to the reference data were computed. Because of the well-known challenges of FOOF,[13,20,21,28] the MAD was also calculated without FOOF. For ccCA, the ccCA-S3 variant was selected as it results in the lowest MAD for the $\Delta H°_{f,\ 298}$'s of oxygen fluoride species with respect to the reference data as shown in Table 3.5 as compared with the other ccCA variants.

Table 3.4 Enthalpies of formation for the oxygen fluoride species using M06 and M06-2X paired with the correlation consistent basis sets.

Compd.	**$\Delta H°_{f,\ 298\ K}$ (kcal mol^{-1})**						
	M06			**M06-2X**			**Reference data[a]**
	aDZ	**aTZ**	**aQZ**	**aDZ**	**aTZ**	**aQZ**	
FO	29.6	28.5	28.1	29.1	28.3	27.5	26.1±2.4
FOH	-16.9	-17.3	-17.7	-16.4	-18.3	-18.6	-23.16±1.2
FOF	12.9	9.7	9.6	11.5	9.6	8.7	5.9±0.5
FOO	10.6	9.5	9.0	18.3	16.0	14.5	6.1±0.5
FOOH	-6.0	-6.9	-7.6	-5.6	-7.6	-8.4	-10.4±1.0[b]
FOOF	14.1	11.3	11.2	18.6	16.9	15.5	4.6±0.5
FOOO	40.3	37.8	36.7	43.4	43.2	41.3	-
FOOOH	4.9	3.5	2.6	6.2	4.1	2.9	-
FOOOF	35.3	31.5	30.9	34.4	32.7	30.9	26.6[c]
MAD	6.3	4.4	4.0	7.7	6.0	5.2	
MAD w/o FOOF	5.7	4.0	3.5	6.7	5.0	4.3	

aDZ: aug-cc-pVDZ
aTZ: aug-cc-pVTZ
aQZ: aug-cc-pVQZ
[a] NIST-JANAF Tables: References 36-37. [b] CCSD(T)/ANO4: Reference 21. [c] Extrapolated CCSD(T)/aug-cc-pV(T,Q)Z: Reference 19.

Table 3.5 Enthalpies of formation for oxygen fluoride species using the different variants of ccCA method.

Compd.	$\Delta H°_{f,\,298\,K}$ (kcal mol^{-1})				
	ccCA-P	**ccCA-S3**	**ccCA-PS3**	**ccCA-S4**	**Reference data**[a]
FO	27.3	27.0	27.2	27.3	26.1±2.4
FOH	-21.1	-21.6	-21.4	-21.1	-23.16±1.2
FOF	6.6	6.2	6.4	6.7	5.9±0.5
FOO	8.1	7.5	7.8	8.1	6.1±0.5
FOOH	-11.0	-11.7	-11.3	-10.9	-10.4±1.0[b]
FOOF	9.4	8.7	9.0	9.4	4.6±0.5
FOOO	31.8[d]	31.0[d]	31.4[d]	31.8[d]	-
FOOOH	-0.7	-1.6	-1.1	-0.6	-
FOOOF	27.8	26.8	27.3	27.8	26.6[c]
MAD	1.8	1.4	1.6	1.8	-
MAD w/o FOOF	1.3	0.9	1.1	1.3	-

[a] NIST-JANAF Tables: References 36-37. [b] CCSD(T)/ANO4: Reference 21. [c] Extrapolated CCSD(T)/aug-cc-pV(T,Q)Z: Reference 19. [d] Using RO-ccCA

The calculated $\Delta H°_{f,\,298}$'s of FO by ccCA, M06, M06-2X, G3, and G3B3 are within the reported experimental uncertainty (± 2.4 kcal mol^{-1}), as shown in Table 3.6. The $\Delta H°_{f,\,298}$'s of FO calculated by G3 and G3B3 are the nearest to the reported experimental value, while the $\Delta H°_{f,\,298}$ calculated by M06 deviated the most by 2.0 kcal mol^{-1}, but is still within the experimental uncertainty. The FO $\Delta H°_{f,\,298}$'s predicted by ccCA is also in very good agreement with experiment. For FOH, the $\Delta H°_{f,\,298}$'s calculated by ccCA is found to be the closest to the reported experimental value, while G3 and G3B3 provide $\Delta H°_{f,\,298}$'s that are 1.6 and 1.9 kcal mol^{-1}, respectively, less than the experimental uncertainty. M06 and M06-2X underestimate the $\Delta H°_{f,\,298}$'s of FOH by 5.46 and 4.56 kcal mol^{-1}, respectively, with respect to the experimental value.

The ccCA $\Delta H°_{f,298}$ of FOF is within the experimental error bar. G3 and G3B3 predict $\Delta H°_{f,298}$'s of 6.5 and 6.8 kcal mol^{-1}, which are greater than the experimental uncertainty by 0.1 and 0.4 kcal mol^{-1}, respectively. M06 predicts a $\Delta H°_{f,298}$ of FOF that is 3.2 kcal mol^{-1} outside of the experimental uncertainty, while the $\Delta H°_{f,298}$ calculated by M06-2X is 2.3 kcal mol^{-1} outside of the experimental uncertainty.

Table 3.6 Calculated enthalpies of formation for the oxygen fluoride species using all methods and the MADs of these methods with respect to the reference data.

Compd.	**$\Delta H°_{f,298\ K}$ (kcal mol^{-1})**					
	ccCA-S3	**M06[a]**	**M06-2X[a]**	**G3**	**G3B3**	**Reference data[b]**
FO	27.0	28.1	27.5	26.1	26.5	26.1±2.4
FOH	-21.6	-17.7	-18.6	-20.4	-20.1	-23.16±1.2
FOF	6.2	9.6	8.7	6.5	6.8	5.9±0.5
FOO	7.5[e]	9.0[f]	14.5[f]	7.1[g]	7.0	6.1±0.5
FOOH	-11.7	-7.6	-8.4	-10.3	-10.2	-10.4±1.0[c]
FOOF	8.7	11.2	15.5	9.3	8.9	4.6±0.5
FOOO	31.0[e]	36.7[f]	41.3[f]	30.1[g]	30.1[g]	-
FOOOH	-1.6	2.6	2.9	0.2	-0.3	-
FOOOF	26.8	30.9	30.9	27.8	27.3	26.6[d]
MAD	1.4	4.0	5.2	1.5	1.5	-
MAD w/o FOOF	0.9	3.5	4.3	0.9	0.9	-

[a] M06 and M06-2X in conjunction with aug-cc-pVQZ. [b] NIST-JANAF Tables: Reference 36-37.
[c] CCSD(T)/ANO4: Reference 21. [d] Extrapolated CCSD(T)/aug-cc-pV(T,Q)Z: Reference 19. [e] Using RO-ccCA. [f] Using ROM06 and ROM06-2X. [g] Using G3-RAD.

For FOO, ccCA and G3B3 give $\Delta H°_{f,298}$'s that are outside the experimental error by 0.9 and 0.4 kcal mol^{-1}, respectively. These results demonstrate the utility of ccCA and G3B3 in predicting the FOO $\Delta H°_{f,298}$. G3-RAD, one of the G3 versions developed for open-shell systems, is used instead of G3 to calculate the $\Delta H°_{f,298}$'s of the radicals FOO and FOOO. The G3-RAD

$\Delta H°_{f,\,298}$ of FOO is also in good agreement with experiment. The calculated $\Delta H°_{f,\,298}$ for FOO using ROM06 is above experimental value by 2.9 kcal mol^{-1}, whereas the $\Delta H°_{f,\,298}$ calculated by ROM06-2X is 10.6 kcal mol^{-1} greater than experiment. This large deviation can be explained by the poor geometry obtained using these ROM06 and ROM06-2X.

For FOOH, the CCSD(T)/ANO4 $\Delta H°_{f,\,298}$ which is -10.4 ± 1.0 kcal mol^{-1},[21] is being used as a reference value for this molecule. G3 and G3B3 predict $\Delta H°_{f,\,298}$'s of FOOH of -10.3 and -10.2 kcal mol^{-1}, respectively, which are in excellent agreement with the CCSD(T) value. Conversely, the ccCA $\Delta H°_{f,\,298}$ value of FOOH is -11.7 kcal mol^{-1}, which is more negative than the CCSD(T) value by 1.3 kcal mol^{-1}. Based on the fact that oxygen fluoride molecules are considered highly correlated molecules, accounting for the core correlation correction in the method is highly important. Thus, ccCA $\Delta H°_{f,\,298}$'s can be more accurate than the CCSD(T) energies because ccCA energies includes core-valence and core-core correction terms, whereas the reported CCSD(T) results used the frozen-core approximation.[21] G3B3 includes the high level correction term (HLC) in the energy. The HLC is calculated based on empirical parameters and it is added to the G3 energy to reduce the error between theory and experiment. Without the HLC the G3B3 $\Delta H°_{f,\,298}$ deviates by ~7.0 kcal mol^{-1} from the CCSD(T) value. M06 and M06-2X both underestimate the $\Delta H°_{f,\,298}$ of FOOH by 2.6 and 1.0 kcal mol^{-1}, respectively. For FOOF, the ccCA $\Delta H°_{f,\,298}$ value lies 3.6 kcal mol^{-1} outside the error bar of the value reported by NIST-JANAF.[36,37] G3 and G3B3 predict $\Delta H°_{f,\,298}$'s that are greater than experimental error bar by 4.2 and 3.8 kcal mol^{-1}, respectively. M06 and M06-2X give $\Delta H°_{f,\,298}$'s larger than experiment by 6.6 and 10.9 kcal mol^{-1}, respectively. Several previous high-level theoretical studies have pointed out the discrepancy between experimental and calculated $\Delta H°_{f,\,298}$'s, and suggested that the experiment to be revisited.[15,20,21,28] For example, high-level methods predicted $\Delta H°_{f,\,298}$ of FOOF

of 9.6 ± 0.9 kcal mol^{-1} (iCAS-CI+Q),[15] 8.7 ± 2.0 kcal mol^{-1} (CCSD(T)/ANO4),[21] 7.84 ± 0.18 kcal mol^{-1} (W4),[20] and 7.3 kcal mol^{-1} (B3PW91/aug-cc-pVQZ).[28] In addition, from this work the ccCA value of the $\Delta H°_{f,\ 298}$ of FOOF is 8.7 kcal mol^{-1}. Thus, the $\Delta H°_{f,\ 298}$'s provided by theoretical approaches is between 7-9 kcal mol^{-1}, whereas the experimental value is 4.6 ± 0.5 kcal mol^{-1}. Because of this large and consistent discrepancy, the MAD of the $\Delta H°_{f,\ 298}$'s is calculated with and without FOOF.

RO-ccCA, G3-RAD, ROM06, and ROM06-2X were employed to calculate the $\Delta H°_{f,\ 298}$ for FOOO and the predicted $\Delta H°_{f,\ 298}$'s are listed in Table 3.6. Due to the lack of reference data for FOOO, the $\Delta H°_{f,\ 298}$ of ccCA for FOOO (31.0 kcal mol^{-1}) is considered the most accurate based on the previous successes of ccCA in predicting energetic properties (MAD of 1.01 kcal mol^{-1} using ccCA-PS3 for main group molecules (G03/05 test set)).[44] G3-RAD also predicts a very close value to the ccCA value (30.1 kcal mol^{-1}). However, including empirical parameters makes G3-RAD a system-dependent method. Thus, the RO-ccCA value is recommended. The computed $\Delta H°_{f,\ 298}$ for FOOO using ROM06 is 5.7 kcal mol^{-1} greater than the RO-ccCA value. M06-2X predicts very high $\Delta H°_{f,\ 298}$'s for FOOO compared to the other methods. For FOOOH, the calculated $\Delta H°_{f,\ 298}$'s of ccCA is considered the reference data for the same reason previously mentioned. The $\Delta H°_{f,\ 298}$ of ccCA for FOOOH (-1.6 kcal mol^{-1}) is chemically sensible since formation of hydride is usually exothermic with fluoride lowering its stability. In addition, G3B3 predicts as exothermic $\Delta H°_{f,\ 298}$ as ccCA, but greater by 1.3 kcal mol^{-1}. G3 and M06 and M06-2X overestimated the $\Delta H°_{f,\ 298}$ of FOOOH by 1.8, 4.2, and 4.5 kcal mol^{-1}, respectively, with respect to the ccCA value. Finally, ccCA successfully predicts the $\Delta H°_{f,\ 298}$ of FOOOF with only a 0.2 kcal mol^{-1} deviation from the extrapolated CCSD(T)/aug-cc-pV(T,Q)Z value calculated previously by Huang et al.,[19] where other methods such as G2 and G96PW91/D95(3df) predicted

$\Delta H°_{f,298}$'s that are > 7.0 kcal mol^{-1} higher than the CCSD(T) value.[67] Here G3B3 $\Delta H°_{f,298}$ is also in good agreement with the CCSD(T) value, with a deviation of only 0.7 kcal mol^{-1} between the two, but G3 $\Delta H°_{f,298}$ differs by 1.2 kcal mol^{-1}. This difference between G3B3 and G3 results typically comes from geometry optimization, with MP2 found to be insufficient to describe the structure of dioxygen fluoride species. M06 and M06-2X again overestimated the enthalpy of formation of FOOOF by 4.3 kcal mol^{-1} with respect to the CCSD(T) value.

The MADs of the calculated $\Delta H°_{f,298}$'s for all the utilized methods with respect to the reference data were computed and provided in Table 3.6. The MADs of M06 and M06-2X as shown in Table 3.6 are 4.0 and 5.2 kcal mol^{-1} (3.5 and 4.3 kcal mol^{-1} without FOOF), respectively. Thus, compared to the chlorine oxides in Table 3.3, M06 and M06-2X do not perform well for oxygen fluoride species. That can be attributed to the poor geometries obtained by M06 and M06-2X. Because of the deficiencies in the M06 and M06-2X computed geometries, single point M06 and M06-2X energy calculations were performed using the B3LYP/aug-cc-pVTZ geometries to examine the performances of M06 and M06-2X for oxygen fluorides energy calculations. $\Delta H°_{f,298}$ and MAD's were calculated and listed in Table 3.7. However, no improvement is noticed in the M06 and M06-2X $\Delta H°_{f,298}$'s when using B3LYP geometries. That supports our conclusion that M06 and M06-2X are not considered reliable methods to predict structures and energetic properties for oxygen fluorides. G3 and G3B3 (including the G3-RAD values) perform well with MAD's of 1.5 kcal mol^{-1} for both methods (0.9 kcal mol^{-1} for both methods without FOOF). This performance is expected taking into account the inclusion of the HLC term in the G3 and G3B3 energy. For example, the G3B3 $\Delta H°_{f,298}$ of FO without the HLC term is 30.3 kcal mol^{-1}, a value that is greater by 3.8 kcal mol^{-1} than the G3B3 $\Delta H°_{f,298}$ listed in Table 3.6. The MAD of the G3 and G3B3 methods (1.5 kcal mol^{-1}) is

much smaller for the oxygen fluorides than for the chlorine oxides (2.3 kcal mol^{-1} for G3 and 3.5 kcal mol^{-1} for G3B3), so G3 and G3B3 perform better for oxygen fluorides than for chlorine oxides. The MAD of ccCA-S3 is 1.4 kcal mol^{-1} (0.9 kcal mol^{-1} without FOOF) for oxygen fluorides and is 1.1 kcal mol^{-1} for chlorine oxides. This indicates a capability of ccCA to predict reliable energetic properties for halogen oxides.

Table 3.7 Calculated enthalpies of formation for the oxygen fluoride species using M06 and M06-2X methods based on B3LYP/aug-cc-pVTZ geometries.

Compd.	**$\Delta H°_{f,\,298\,K}$ (kcal mol^{-1})**		
	B3LYP[a]//M06[b]	**B3LYP[a]//M06-2X[b]**	**Reference data[c]**
FO	28.4	27.7	26.1±2.4
FOH	-17.5	-18.5	-23.16±1.2
FOF	10.2	9.3	5.9±0.5
FOO	9.3	15.0	6.1±0.5
FOOH	-6.9	-7.7	-10.4±1.0[d]
FOOF	11.8	19.9	4.6±0.5
FOOO	34.7	47.5	-
FOOOH	4.9	4.5	-
FOOOF	31.8	32.1	26.6[e]
MAD	4.5	6.0	-
MAD w/o FOOF	4.0	4.4	-

[a] B3LYP/aug-cc-pVTZ. [b] M06/aug-cc-pVQZ and M06-2X/aug-cc-pVQZ
[c] NIST-JANAF Tables: Reference 36-37. [d] CCSD(T)/ANO4: Reference 21.
[e] Extrapolated CCSD(T)/aug-cc-pV(T,Q)Z: Reference 19.

In addition, a comparison between the calculated $\Delta H°_{f,\,298}$'s in this study and the recent Active Thermochemical Tables (ATcT)[68,69] values of the $\Delta H°_{f,\,298}$'s of FO, FOH, FOF, FOO, FOOF, and FOOOF are examined. The ATcT tables use artificial intelligence algorithms to reduce the uncertainties in the experimentally measured $\Delta H°_{f,\,298}$'s by combining experimental

and highly accurate theoretical thermochemical data.[68,69] As shown in Table 3.8, the uncertainties of the ATcT values of FO, FOH, FOF, and FOO decreased in comparison to the NIST-JANAF values (Table 3.6). Thus, to evaluate our methods against the ATcT values, the MADs of the calculated $\Delta H°_{f,\,298}$'s for all the utilized methods with respect to the ATcT values were computed and provided in Table 3.8. The MADs of ccCA-S3, M06, M06-2X, G3, and G3B3 were all lowered by 0.5-0.9 kcal mol^{-1} in comparison with the MADs shown in Table 3.6 (with ccCA-S3 providing the lowest MAD, at 0.6 kcal mol^{-1}). The large difference in the MADs between NIST-JANAF table and ATcT is likely attributed to the large difference between the ATcT value of the $\Delta H°_{f,\,298}$ of FOOF (8.04±0.09 kcal mol^{-1}) and the NIST-JANAF value (4.6 ± 0.5 kcal mol^{-1}).

Table 3.8 Calculated Enthalpies of formation for the oxygen fluoride species using all methods and the MADs of these methods with respect to the ATcT values.

Compd.	**$\Delta H°_{f,\,298\,K}$ (kcal mol^{-1})**					
	ccCA-S3	**M06[a]**	**M06-2X[a]**	**G3**	**G3B3**	**ATcT[b]**
FO	27.0	28.1	27.5	26.1	26.5	26.51±0.04
FOH	-21.6	-17.7	-18.6	-20.4	-20.1	-20.85±0.05
FOF	6.2	9.6	8.7	6.5	6.8	5.91±0.06
FOO	7.5[e]	9.0[f]	14.5[f]	7.1[g]	7.0	5.99±0.06
FOOH	-11.7	-7.6	-8.4	-10.3	-10.2	-
FOOF	8.7	11.2	15.5	9.3	8.9	8.04±0.09
FOOO	31.0[c]	36.7[d]	41.3[d]	30.1[e]	30.1[e]	-
FOOOH	-1.6	2.6	2.9	0.2	-0.3	-
FOOOF	26.8	30.9	30.9	27.8	27.3	26.63±1.86
MAD	0.6	3.1	4.7	0.8	0.7	

[a] M06 and M06-2X in conjunction with aug-cc-pVQZ. [b]ATcT: Reference 68-69. [c] Using RO-ccCA. [d] Using ROM06 and ROM06-2X. [e] Using G3-RAD.

3.1 Conclusion

The capability of ccCA, G3, and G3B3 for the prediction of the enthalpies of formation of oxygen fluoride species was evaluated. In addition, the performance of M06 and M06-2X in conjunction with the correlation consistent basis sets (aug-cc-pV*n*Z), where *n* = D, T, Q, was also examined for predicting the structures and enthalpies of formation of oxygen fluoride species. An important finding from this study is that though M06 and M06-2X are useful functionals for many main group species (including chlorine oxides), M06 and M06-2X were less successful in the prediction of reasonable structures and $\Delta H°_{f,\,298}$'s for oxygen fluorides, oxygen difluorides, and related hydrides. This could be generalized to systems containing F-O and/or O-O bonds (e.g. peroxides and polyoxides). Geometries predicted by B3LYP/aug-cc-pVTZ are generally in good agreement with the listed reference data. When calculating the enthalpies of formation, ccCA-S3 provides the lowest MAD (1.4 kcal mol^{-1} with respect to the reference data; 0.9 kcal mol^{-1} excluding FOOF) without any parameterized energies. While ccCA-S3 provides the smallest MAD of the four different CBS extrapolation formulas considered for this set of molecules, other ccCA variants, such as ccCA-PS3, have been found to be useful in previous studies.[44,45] G3 and G3B3 achieved a MAD that is greater than ccCA-S3 by only 0.1 kcal mol^{-1} with respect to the reference data while incorporating an empirical parameter that is intended to reduce the overall MAD of G3 and G3B3 (or MAD of 0.9 kcal mol^{-1} excluding FOOF, which is identical to ccCA-S3 in this case). The performance of G3 and G3B3 for chlorine oxides is not as good as for oxygen fluorides. ccCA-S3 predictions of the $\Delta H°_{f,\,298}$'s of both the oxygen fluorides and of the chloride oxides species are in good agreement with the experimental values. In addition, when comparing the calculated $\Delta H°_{f,\,298}$'s to the ATcT values, ccCA-S3 provides the lowest MAD (0.6 kcal mol^{-1}) in comparison to the other methods included

in this study. The enthalpies of formation for FOOO and FOOOH are predicted to be 31.0 and -1.6 kcal mol^{-1}, respectively, by the ccCA-S3 method. Overall, the use of the correlation consistent Composite Approach (ccCA) is recommended for such systems, with promise for other halogen systems and peroxides.

REFERENCES

REFERENCES

(1) Prather, M. J.; McElroy, M. B.; Wofsy, S. C. Reductions in Ozone at High Concentrations of Stratospheric Halogens. *Nature*. 1984, pp 227–231.

(2) Prather, M. J.; Watson, R. T. Stratospheric Ozone Depletion and Future Levels of Atmospheric Chlorine and Bromine. *Nature*. 1990, pp 729–734.

(3) Sander, S. P.; Friedl, R. R.; Yung, Y. L. Rate of Formation of the ClO Dimer in the Polar Stratosphere: Implications for Ozone Loss. *Science*. 1989, pp 1095–1098.

(4) Solomon, S. Progress towards a Quantitative Understanding of Antarctic Ozone Depletion. *Nature*. 1990, pp 347–354.

(5) Ravishankara, A. R.; Turnipseed, A. A.; Jensen, N. R.; Barone, S.; Mills, M.; Howard, C. J.; Solomon, S. Do Hydrofluorocarbons Destroy Stratospheric Ozone? *Science*. 1994, pp 71–75.

(6) Parrish, A.; De Zafra, R. L.; Solomon, P. M.; Barrett, J. W.; Carlson, E. R. Chlorine Oxide in the Stratospheric Ozone Layer: Ground-Based Detection and Measurement. *Science*. 1981, pp 1158–1161.

(7) Colussi, A. J.; Grela, M. A. Rate of the Reaction between Oxygen Monofluoride and Ozone: Implications for the Atmospheric Role of Fluorine. *Chem. Phys. Lett.* **1994**, *229* (1–2), 134–138.

(8) Zander, R.; Rinsland, C. P.; Mahieu, E.; Gunson, M. R.; Farmer, C. B.; Abrams, M. C.; Ko, M. K. W. Increase of Carbonyl Fluoride (COF_2) in the Stratosphere and Its Contribution to the 1992 Budget of Inorganic Fluorine in the Upper Stratosphere. *J. Geophys. Res. Atmos.* **1994**, *99* (D8), 16737–16743.

(9) Nassar, R.; Bernath, P. F.; Boone, C. D.; McLeod, S. D.; Skelton, R.; Walker, K. A.; Rinsland, C. P.; Duchatelet, P. A Global Inventory of Stratospheric Fluorine in 2004 Based on Atmospheric Chemistry Experiment Fourier Transform Spectrometer (ACE-FTS) Measurements. *J. Geophys. Res. Atmos.* **2006**, *111* (D22), D22313.

(10) Brown, A. T.; Chipperfield, M. P.; Richards, N. A. D.; Boone, C.; Bernath, P. F. Global Stratospheric Fluorine Inventory for 2004–2009 from Atmospheric Chemistry Experiment Fourier Transform Spectrometer (ACE-FTS) Measurements and SLIMCAT Model Simulations. *Atmos. Chem. Phys.* **2014**, *14* (1), 267–282.

(11) Jackson, R. H. The Microwave Spectrum, Structure, and Dipole Moment of Dioxygen Difluoride. *J. Chem. Soc.* **1962**, 4585–4592.

(12) Pierce, L.; Di Cianni, N.; Jackson, R. H. Centrifugal Distortion Effects in Asymmetric Rotor Molecules. I. Quadratic Potential Constants and Average Structure of Oxygen Difluoride from the Ground-State Rotational Spectrum. *J. Chem. Phys.* **1963**, *38* (3), 730–739.

(13) Feller, D.; Dixon, D. A. Coupled Cluster Theory and Multireference Configuration Interaction Study of FO, F_2O, FO_2, and FOOF. *J. Phys. Chem. A* **2003**, *107* (45), 9641–9651.

(14) Alcami, M.; Mó, O.; Yáñez, M.; Cooper, I. L. The Performance of Density-Functional Theory in Challenging Cases: Halogen Oxides. *J. Chem. Phys.* **2000**, *112* (14), 6131–6140.

(15) Feller, D.; Peterson, K. A.; Dixon, D. A. Refined Theoretical Estimates of the Atomization Energies and Molecular Structures of Selected Small Oxygen Fluorides. *J. Phys. Chem. A* **2010**, *114* (1), 613–623.

(16) Francisco, J. S.; Zhao, Y.; Lester, W. A.; Williams, I. H. Theoretical Studies of the Structure and Thermochemistry of FO_2 Radical: Comparison of Møller–Plesset Perturbation, Complete-active-space Self-consistent-field, and Quadratic Configuration Interaction Methods. *J. Chem. Phys.* **1992**, *96* (4), 2861–2867.

(17) Halonen, L.; Ha, T. K. Equilibrium Structure and Anharmonic Force Field of Hypofluorous Acid (HOF). *J. Chem. Phys.* **1988**, *89* (8), 4885–4888.

(18) Jursic, B. S. The Density Functional Theory Investigation of the Equilibrium Structures of OOF, FOOF, OOF_2, and FOOOF. *J. Mol. Struct. THEOCHEM* **1996**, *366* (1–2), 97–101.

(19) Huang, M.-J.; Watts, J. D. Theoretical Characterization of the F_2O_3 Molecule by Coupled Cluster Methods. *J. Phys. Chem. A* **2010**, *114*, 10197.

(20) Karton, A.; Parthiban, S.; Martin, J. M. L. Post-CCSD(T) Ab Initio Thermochemistry of Halogen Oxides and Related Hydrides XOX, XOOX, HOX, XO_n, and HXO_n (X = F, Cl), and Evaluation of DFT Methods for These Systems. *J. Phys. Chem. A* **2009**, *113* (16), 4802–4816.

(21) Lee, T. J.; Rice, J. E.; Dateo, C. E. The Varying Nature of Fluorine Oxygen Bonds. *Mol. Phys.* **1996**, *89* (5), 1359–1372.

(22) Miller, C. E.; Drouin, B. J. The $X_1\,^2\Pi_{3/2}$ and $X_2\,^2\Pi_{1/2}$ Potential Energy Surfaces of FO. *J. Mol. Spectrosc.* **2001**, *205* (2), 312–318.

(23) Minyaev, R. M.; Gribanova, T. N. Structure and Stability of Halogen Oxoacids XO_nH (X = F, Cl; n = 1-4): A Quantum Chemistry Study. *Russ. J. Inorg. Chem.* **2004**, *49*, 579–586.

(24) O'Hare, P. A. G.; Wahl, A. C. Oxygen Monofluoride (OF, 2Π): Hartree–Fock Wavefunction, Binding Energy, Ionization Potential, Electron Affinity, Dipole and Quadrupole Moments, and Spectroscopic Constants. A Comparison of Theoretical and Experimental Results. *J. Chem. Phys.* **1970**, *53* (6), 2469–2478.

(25) Roohi, H.; Mackiabadi, B. Conformations of O_3–F 1:1 Complexes. An Ab Initio Study. *Bull. Chem. Soc. Jpn.* **2007**, *80* (10), 1914–1919.

(26) Ventura, O. N.; Kieninger, M. The FO_2 Radical: A New Success of Density Functional Theory. *Chem. Phys. Lett.* **1995**, *245* (4–5), 488–497.

(27) Zhao, Y.; Francisco, J. S. Ab Initio Studies of the Structure and Thermochemistry of FO Radicals. *Chem. Phys. Lett.* **1990**, *167* (4), 285–290.

(28) Kieninger, M.; Segovia, M.; Ventura, O. N. A Discrepancy between Experimental and Theoretical Thermochemical Characterization of Some Oxygen Fluorides. *Chem. Phys. Lett.* **1998**, *287* (5–6), 597–600.

(29) Kraka, E.; He, Y.; Cremer, D. Quantum Chemical Descriptions of FOOF: The Unsolved Problem of Predicting Its Equilibrium Geometry. *J. Phys. Chem. A* **2001**, *105* (13), 3269–3276.

(30) Denis, P. A.; Ventura, O. N. CCSDT Study of the Fluoroperoxyl Radical, FOO. *Chem. Phys. Lett.* **2004**, *385* (3–4), 292–297.

(31) Yamada, C.; Hirota, E. The Infrared Diode Laser Spectrum of the ν_2 Band of the FO_2 Radical. *J. Chem. Phys.* **1984**, *80* (10), 4694–4700.

(32) Denis, P. A.; Ventura, O. N. Corrigendum to "CCSDT Study of the Fluoroperoxyl Radical, FOO" [Chem. Phys. Lett. 385 (2004) 292–297]. *Chem. Phys. Lett.* **2004**, *395* (4–6), 385–386.

(33) Denis, P. A. On the Performance of CCSD(T) and CCSDT in the Study of Molecules with Multiconfigurational Character: Halogen Oxides, HSO, BN and O_3. *Chem. Phys. Lett.* **2004**, *395* (1–3), 12–20.

(34) Karton, A.; Rabinovich, E.; Martin, J. M. L.; Ruscic, B. W4 Theory for Computational

Thermochemistry: In Pursuit of Confident Sub-kJ/mol Predictions. *J. Chem. Phys.* **2006**, *125*, 144108–144117.

(35) Dixon, D. A.; Andzelm, J.; Fitzgerald, G.; Wimmer, E. Density Functional Study of a Highly Correlated Molecule, Oxygen Fluoride (FOOF). *J. Phys. Chem.* **1991**, *95* (23), 9197–9202.

(36) Chase, M. W.; Davies, C. A.; Downey, J. R.; Frurip, D. J.; McDonald, R. A.; Syverud, A. N. JANAF Thermochemical Tables, 3rd Ed. *J. Phys. Chem. Ref. Data* **1985**, *14*.

(37) Chase, M. W. NIST-JANAF Thermochemical Tables, 4th Ed. *J. Phys. Chem. Ref. Data* **1998**, 2.

(38) Frecer, V.; Jain, D. C.; Sapse, A.-M. Ab Initio Calculations for FO_3, FO_3^+ , and FO_3^- Complexes Formed by Fluorine with Ozone. *Struct. Chem.* **1998**, *9* (1), 9–13.

(39) Misochko, E. Y.; Akimov, A. V; Wight, C. A. Infrared Spectroscopic Observation of the Stabilized Intermediate Complex FO_3 Formed by Reaction of Mobile Fluorine Atoms with Ozone Molecules Trapped in an Argon Matrix. *J. Phys. Chem. A* **1999**, *103* (40), 7972–7977.

(40) Li, L.-C.; Wang, J.; Wang, X.; Tian, A.-M.; Wong, N.-B. Quantum Chemical Study of the Reaction Mechanism of Ozone and Methane with Fluorine and Chlorine Atoms. *Int. J. Quantum Chem.* **2002**, *87* (5), 288–292.

(41) Peiró-Garcí̄a, J.; Nebot-Gil, I. An Ab Initio Study on the Mechanism of the $F+O_3 \rightarrow FO+O_2$ Reaction: Comparative Reactivity Study along the Isoelectronic NH_2, OH and F Radicals Series. *Chem. Phys. Lett.* **2004**, *391* (1–3), 195–199.

(42) Glidewell, C. Structure and Conformation in Molecular Peroxides. *J. Mol. Struct.* **1980**, *67*, 35–44.

(43) Gimarc, B. M.; Zhao, M. Oxygen Ring Strain Energies Revisited: Effects of Terminal Atoms of the Chain Reference Structure. *J. Phys. Chem.* **1994**, *98* (6), 1596–1600.

(44) DeYonker, N. J.; Wilson, B. R.; Pierpont, A. W.; Cundari, T. R.; Wilson, A. K. Towards the Intrinsic Error of the Correlation Consistent Composite Approach (ccCA). *Mol. Phys.* **2009**, *107* (8–12), 1107–1121.

(45) DeYonker, N. J.; Grimes, T.; Yockel, S.; Dinescu, A.; Mintz, B.; Cundari, T. R.; Wilson, A. K. The Correlation-Consistent Composite Approach: Application to the G3/99 Test Set. *J. Chem. Phys.* **2006**, *125*, 104111–104115.

(46) DeYonker, N. J.; Cundari, T. R.; Wilson, A. K. The Correlation Consistent Composite Approach (ccCA): An Alternative to the Gaussian-*n* Methods. *J. Chem. Phys.* **2006**, *124*, 114104–114121.

(47) Zhao, Y.; Truhlar, D. The M06 Suite of Density Functionals for Main Group Thermochemistry, Thermochemical Kinetics, Noncovalent Interactions, Excited States, and Transition Elements: Two New Functionals and Systematic Testing of Four M06-Class Functionals and 12 Other Functionals. *Theor. Chem. Acc.* **2008**, *120* (1), 215–241.

(48) Meyer, M. M.; Kass, S. R. Experimental and Theoretical Gas-Phase Acidities, Bond Dissociation Energies, and Heats of Formation of $HClO_x$, X = 1-4. *J. Phys. Chem. A* **2010**, *114* (12), 4086–4092.

(49) Dunning, T. H. Gaussian Basis Sets for Use in Correlated Molecular Calculations. I. The Atoms Boron through Neon and Hydrogen. *J. Chem. Phys.* **1989**, *90* (2), 1007–1023.

(50) Woon, D. E.; Dunning, T. H. Gaussian Basis Sets for Use in Correlated Molecular Calculations. III. The Atoms Aluminum through Argon. *J. Chem. Phys.* **1993**, *98* (2), 1358–1371.

(51) Dunning, T. H.; Peterson, K. A.; Wilson, A. K. Gaussian Basis Sets for Use in Correlated Molecular Calculations. X. The Atoms Aluminum through Argon Revisited. *J. Chem. Phys.* **2001**, *114* (21), 9244–9253.

(52) Curtiss, L. A.; Raghavachari, K.; Redfern, P. C.; Rassolov, V.; Pople, J. A. Gaussian-3 (G3) Theory for Molecules Containing First and Second-Row Atoms. *J. Chem. Phys.* **1998**, *109* (18), 7764–7776.

(53) Baboul, A. G.; Curtiss, L. A.; Redfern, P. C.; Raghavachari, K. Gaussian-3 Theory Using Density Functional Geometries and Zero-Point Energies. *J. Chem. Phys.* **1999**, *110* (16), 7650–7657.

(54) Jorgensen, K. R.; Wilson, A. K. Enthalpies of Formation for Organosulfur Compounds: Atomization Energy and Hypohomodesmotic Reaction Schemes via Ab Initio Composite Methods. *Comput. Theor. Chem.* **2012**, *991*, 1–12.

(55) Wilson, B. R.; DeYonker, N. J.; Wilson, A. K. Prediction of Hydrocarbon Enthalpies of Formation by Various Thermochemical Schemes. *J. Comput. Chem.* **2012**, *33* (25), 2032–2042.

(56) Frisch, M. J.; Trucks, G. W.; Schlegel, H. B.; Scuseria, G. E.; Robb, M. A.; Cheeseman, J. R.; Scalmani, G.; Barone, V.; Mennucci, B.; Petersson, G. A.; et al. Gaussian 09, 2009.

(57) Peterson, K. A.; Dunning, T. H. Accurate Correlation Consistent Basis Sets for Molecular Core–valence Correlation Effects: The Second Row Atoms Al–Ar, and the First Row Atoms B–Ne Revisited. *J. Chem. Phys.* **2002**, *117* (23), 10548–10560.

(58) Schwartz, C. Importance of Angular Correlations between Atomic Electrons. *Phys. Rev.* **1962**, *126* (3), 1015–1019.

(59) Peterson, K. A.; Woon, D. E.; Dunning, T. H. Benchmark Calculations with Correlated Molecular Wave Functions. IV. The Classical Barrier Height of the $H+H_2 \rightarrow H_2+H$ Reaction. *J. Chem. Phys.* **1994**, *100* (10), 7410–7415.

(60) Williams, T. G.; DeYonker, N. J.; Ho, B. S.; Wilson, A. K. The Correlation Consistent Composite Approach: The Spin Contamination Effect on an MP2-Based Composite Methodology. *Chem. Phys. Lett.* **2011**, *504* (1–3), 88–94.

(61) Henry, D. J.; Sullivan, M. B.; Radom, L. G3-RAD and G3X-RAD: Modified Gaussian-3 (G3) and Gaussian-3X (G3X) Procedures for Radical Thermochemistry. *J. Chem. Phys.* **2003**, *118* (11), 4849–4860.

(62) Meyer, M. M. Probing the Structure and Reactivity of Gaseous Ions. Ph.D. Dissertation, University of Minnesota, Minneapolis, MN, 2010.

(63) Laury, M. L.; Carlson, M. J.; Wilson, A. K. Vibrational Frequency Scale Factors for Density Functional Theory and the Polarization Consistent Basis Sets. *J. Comput. Chem.* **2012**, *33* (30), 2380–2387.

(64) Colussi, A. J.; Grela, M. A. Kinetics and Thermochemistry of Chlorine- and Nitrogen-Containing Oxides and Peroxides. *J. Phys. Chem.* **1993**, *97* (15), 3775–3779.

(65) Rathmann, T.; Schindler, R. N. Ab Initio Calculations on the Geometries and Thermodynamic Stabilities of Chlorine Trioxides. *Chem. Phys. Lett.* **1992**, *190* (6), 539–542.

(66) Rauk, A.; Tschuikow-Roux, E.; Chen, Y.; McGrath, M. P.; Radom, L. The Possible Role of Chlorine Trioxide Isomers in Relation to Stratospheric Ozone. *J. Phys. Chem.* **1993**, *97* (30), 7947–7954.

(67) Ju, X.-H.; Wang, Z.-Y.; Yan, X.-F.; Xiao, H.-M. Density Functional Theory Studies on Dioxygen Difluoride and Other Fluorine/oxygen Binary Compounds: Availability and Shortcoming. *J. Mol. Struct. THEOCHEM* **2007**, *804* (1–3), 95–100.

(68) Ruscic, B.; Pinzon, R. E.; Morton, M. L.; von Laszevski, G.; Bittner, S. J.; Nijsure, S. G.; Amin, K. A.; Minkoff, M.; Wagner, A. F. Introduction to Active Thermochemical

Tables: Several “Key” Enthalpies of Formation Revisited. *J. Phys. Chem. A* **2004**, *108* (45), 9979–9997.

(69) Ruscic, B.; Pinzon, R. E.; Laszewski, G. Von; Kodeboyina, D.; Burcat, A.; Leahy, D.; Montoy, D.; Wagner, A. F. Active Thermochemical Tables: Thermochemistry for the 21st Century. *J. Phys. Conf. Ser.* **2005**, *16*, 561–570.

(70) Sander, S. P.; Friedl, R. R.; Golden, D. M.; Kurylo, M. J.; Moortgat, G. K.; Keller-Rudek, H.; Wine, P. H.; Ravishankara, A. R.; Kolb, C. E.; Molina, M. J.; et al. *Chemical Kinetics and Photochemical Data for Use in Atmospheric Studies, Evaluation N. 15*; JPL Publication 06-2, Jet Propulsion Laboratory: Pasadena, 2006.

(71) Nickolaisen, S. L.; Friedl, R. R.; Sander, S. P. Kinetics and Mechanism of the Chlorine Oxide ClO + ClO Reaction: Pressure and Temperature Dependences of the Bimolecular and Termolecular Channels and Thermal Decomposition of Chlorine Peroxide. *J. Phys. Chem.* **1994**, *98* (1), 155–169.

(72) Joens, J. A. The Dissociation Energy of OH($X^2\,\Pi_{3/2}$) and the Enthalpy of Formation of OH($X_2\,\Pi_{3/2}$), ClOH, and BrOH from Thermochemical Cycles. *J. Phys. Chem. A* **2001**, *105* (49), 11041–11044.

CHAPTER 4 ENTHALPIES OF FORMATION FOR ORGANOSELENIUM COMPOUNDS VIA SEVERAL THERMOCHEMICAL SCHEMES

4.1. Introduction

Organoselenium compounds have been a subject of interest due to their potential applications in areas including organic synthesis,[1,2] green chemistry,[3,4] biochemistry,[5-8] redox chemistry,[9,10] and synthesis of conducting materials, semiconductors, and optoelectronic materials.[11-15] Organoselenium reagents such as selenoxide, carbonyl selenide, isoselenocyanates, and selenones play an important role in organic reactions involving transformation mechanisms and typically result in high yields overall.[1,2] The generation of complex alkenes via the stereospecific syn-elimination of selenoxides is another important and successful applications of organic selenium compounds.[16-18]

Although selenium is a chalcogen like oxygen and sulfur, it exhibits quite different chemistry. The selenium-carbon bond (bond length (r) = 1.98 Å and bond dissociation energy (BDE) = 55.93 kcal mol^{-1}) is longer and weaker than that of the sulfur-carbon bond (r = 1.81 Å and BDE = 65.01 kcal mol^{-1}), which, in turn, is longer and weaker than the carbon-oxygen bond (r = 1.41 Å and BDE = 85.56 kcal mol^{-1}). Organoselenium reagents, as a result, are more active and involved in wide range of chemical applications than their corresponding organosulfur and organo-oxygen compounds.[19]

Insight about the potential utility of organoselenium compounds can be gained, in part, by knowing about their thermochemical properties including enthalpies of formation, Gibbs free energies, and bond dissociation energies at certain temperatures. Due to the weak Se-C and Se-Se bonds, some organoselenium compounds tend to be relatively unstable during

thermochemical measurements. In addition to their instability, toxicity and difficulties in purification also contribute to the limited availability of thermochemical experimental data for organoselenium species as well as numerous discrepancies among the available experimental results.[20,21] For example, Voronkov et al.[22] reported an enthalpy of formation ($\Delta H°_{f,298}$) of diethyl selenide ($C_2H_5SeC_2H_5$) of -11.78 ± 0.96 kcal mol^{-1} while Tel'noi et al.[23] reported an $\Delta H°_{f,298}$ of -5.02 ± 0.96 kcal mol^{-1} for the same molecule. The most recent review of the thermochemistry of organoselenium compounds was in 2011 by Liebman and Slayden[21] in which they reviewed and assessed the available $\Delta H°_{f,298}{}'s$ of organoselenium compounds that were mostly reported in three different review publications.[22-24]

The lack of reliable thermochemical properties of organoselenium species increases the need for high-level *ab initio* quantum chemical calculations for the prediction of energetic properties of organoselenium compounds and for the validation of available experimental data. Boyd et al.[25,26] evaluated the performance of density functionals for the prediction of the geometries and bond dissociation energies of several biologically relevant organoselenium compounds with respect to the quadratic configuration interaction (QCISD) in conjunction with the cc-pVTZ basis set. The authors found that B3PW91 in conjunction with 6-311G(2df,p) performed the best.[25,26] Another study by Maung et al.[27] found that MP2/6-311G(d,p) predicted the most accurate BDE of HSe-H (H_2Se) with a deviation of only 0.3 kcal mol^{-1} off from experiment, while B3LYP/6-311G(d,p) predicted a BDE that is 4.7 kcal mol^{-1} higher than the experimental value. Maung also calculated BDEs of other organoselenium compounds using several density functionals. Due to the absence of reliable reference data, according to Maung, no definitive conclusion can be reached from their study,[27] although the non-local BHandHLYP functional was determined to be the most useful choice for the prediction of BDEs of

organoselenium compounds at an inexpensive computational cost with respect to its prediction of the BDEs of HSe-H and H-Se.[27] Overall, most of the theoretical applications of quantum mechanics on organoselenium compounds involved the prediction and evaluation of BDEs rather than $\Delta H°_{f,298}'s$.[25-30]

Although QCISD and coupled cluster with single, double, and perturbative triple excitations (CCSD(T)) have been reliable for predicting energetic properties, it is essential that the energies are extrapolated to the complete basis set (CBS) limit, i.e. the basis set incompleteness error is eliminated. However, CBS calculations with highly correlated methods are computationally demanding in terms of computer time, memory, and disk space. A number of *ab initio* composite approaches have been developed for modeling thermochemical properties with accuracy similar to that possible with CCSD(T)/CBS, but with reduced computational cost.[31-38] Composite methods utilize a series of steps combining lower level methods and basis sets to replicate results possible with higher level methods. The most commonly used composite methods are the Gaussian-*n* (G*n*) methods developed by Pople et al.[31-34] Other successful composite methods are the correlation consistent Composite Approaches (ccCA) developed by Wilson et al.[35-41] The G*n* methods, detailed in Chapter 2 Section 2.5.2 and elsewhere,[42] were extended to include molecules containing third-row main group elements.[34,43,44] The developers of the G*n* methods also introduced molecule sets, such as G3/05 set,[45] that can be used to gauge the utility of computational approaches.

The only selenium-containing compounds in the G3/05 set are SeH and SeH_2. The deviations of the calculated atomization energies with respect to experiments for SeH are 0.1 kcal mol^{-1} (G2), -1.1 kcal mol^{-1} (G3), and -0.7 kcal mol^{-1} (G4), and the deviations for SeH_2 are 1.1 kcal mol^{-1} (G2), 0.9 kcal mol^{-1} (G3), and 1.1 kcal mol^{-1} (G4).[34,44] The $\Delta H°_{f,298}$ of SeH_2 was

computed using G2 and was only 1.1 kcal mol^{-1} off from the experimental value.[46] ccCA, detailed in Chapter 2 Section 2.5.2 and elsewhere,[47] also was applied to the G3/05 training set.[37] The deviation of the calculated atomization energies when using ccCA with respect to experiment was -0.7 kcal mol^{-1} for SeH and -0.4 kcal mol^{-1} for SeH_2. These deviations were reduced to -0.2 kcal mol^{-1} for both molecules when including the theoretical second-order atomic spin-orbit corrections, calculated by Blaudeau et al.[48] using the configuration interaction (CI) method, to the ccCA energy,[37] displaying a superior performance over the G*n* methods for these molecules. The ccCA mean absolute deviation (MAD) for the molecules containing third-row atoms (Ga-Kr) included in the G3/05 set was 0.95 kcal mol^{-1} (0.88 kcal mol^{-1} when the second-order atomic spin-order corrections was included) for a group of thermochemical properties including 19 atomization energies (D_0), 11 enthalpies of formation (ΔH_f), 15 ionization potentials (IP), 4 electron affinities (EA), and 2 proton affinities (PA).[37] The aforementioned examples illustrate the rigor of these composite approaches.

There has been much less investigation of the $\Delta H°_{f,298}{}'s$ of selenium-containing organic compounds than for oxygen- or sulfur-containing organic compounds. The most common and simplest method to determine the $\Delta H°_{f,298}{}'s$ in calculations is through the use of the atomization energy approach. This approach employs the difference in energy between the target molecule and its constituent atoms. Although the atomization approach (RC0) has been successfully applied to predict $\Delta H°_{f,298}{}'s$ using high levels of theory and/or model chemistries, differential electron correlation effects and size extensivity can be two problems associated with using this approach. Differential electron correlation effects come from the difference in correlation energy between the molecules (can involve conjugation, polarization, and strain) and the isolated atoms.[49-51] Size extensivity is the ability of a method to scale linearly with increasing the number

of electrons, i.e. the method becomes independent of the size of the system.[41,52] Typically, these two factors become increasingly important as the size of the target molecule is increased. Additionally, since the atomization approach involves relative energies of a molecule and its constituent atoms, any error associated with the approximation of the Schrödinger equation (i.e. Born-Oppenheimer approximation, lack of correlation correction, relativistic effects, and incomplete basis sets) will not be balanced resulting in an accumulation of errors.[41,53] In order to reduce these errors, molecular reaction schemes such as the isogyric reaction, isodesmic reaction, and homodesmotic reaction schemes have been developed to calculate thermochemical properties based on bond interaction energies.[54,55] In thermochemical reaction schemes, relative energies are calculated between the target molecule and its constituent molecules (known as elemental reactants and products) rather than between the target molecule and its constituent atoms as is the case when using the atomization approach. This allows for the cancellation of errors arising from differential electron correlation and size extensivity; thus, in principle, the isodesmic reaction scheme can provide more accurate energetic properties than the atomization approach depending on the accuracy of the calculated reaction enthalpy of the bond separation reaction (BSR) of the target molecule and the experimental $\Delta H°_{f,298}{}'s$ of the constituent molecules.[40,41,52,56-58]

Wheeler et al.[57,58] defined a hierarchy of homodesmotic reactions for the calculation of $\Delta H°_{f,298}{}'s$ for hydrocarbon compounds. The hierarchy includes: isogyric (RC1), isodesmic (RC2), hypohomodesmotic (RC3), homodesmotic (RC4), and hyperhomodesmotic (RC5) reactions.[57] As the homodesmotic reactions hierarchy increases from RC1 to RC5, the degree of error-balanced between reactants and products increases as well as the accuracy of computed enthalpies. For acyclic, closed-shell hydrocarbons, even low-level computational methods such

as Hartree-Fock can provide chemical accuracy when it is used with RC4 or RC5 reaction schemes.[58] The definition of these reaction schemes, according to Wheeler,[57,58] are shown in Table 4.1. In RC1 the number of electron pairs is maintained while in RC2 the number and type of carbon-carbon are both maintained. Not only the number and the bond type of C-C bonds are conserved in RC3, but also the hybridization state and the number of carbons with an equal number of hydrogen atoms attached are both maintained. RC4 and RC5 balance more chemical interactions than the lower scheme, see Table 4.1. This homodesmotic reaction hierarchy provides a clear classification and definition of homodesmotic reactions that make it possible to extend the scheme to a variety of organic molecules including those containing oxygen and sulfur atoms.

Table 4.1 The definition of the homodesmotic reaction schemes according to Wheeler.[57,58]

Reaction scheme	**Name**	**Reaction scheme constraints**
RC1	isogyric	The number of electron pairs and unpaired electrons
RC2	isodesmic	The number and bond type of carbon-carbon
RC3	hypohomodesmotic	The number and the bond type of C-C bond, and The hybridization state of each carbon atom and the number of carbons with an equal number of hydrogen atoms attached
RC4	homodesmotic	"The number of each type of carbon-carbon bond [$C_{sp^3} - C_{sp^3}, C_{sp^3} - C_{sp^2}, C_{sp^3} - C_{sp}, C_{sp^2} - C_{sp^2}, C_{sp^2} - C_{sp}, C_{sp} - C_{sp}, C_{sp^2} = C_{sp^2}, C_{sp^2} = C_{sp}, C_{sp} = C_{sp}, C_{sp} \equiv C_{sp}$]in reactants and products, and The numbers of each type of carbon atom (sp^3, sp^2, sp) with zero, one, two, and three hydrogens attached in reactants and products"
RC5	hyperhomodesmotic	The number of carbon-carbon bond types [$H_3C - CH_2, H_3C - CH, H_2C - CH_2, H_3C - C, H_2C - CH, H_2C - C, HC - CH, HC - C, C - C,\ H_2C = CH, HC = CH, H_2C = C, HC = C, C = C, HC \equiv C,$ and $C \equiv C$] in reactants and products, and The number of each type of carbon atom (sp^3, sp^2, sp) with zero, one, two, and three hydrogens attached in reactants and products"

Wilson et al.[41] extended this definition to include larger molecules and found that for the

ccCA and G3 methods it is necessary to use higher level reaction schemes to gain high accuracy when calculating the $\Delta H°_{f,298}{}'s$ of aromatic hydrocarbons. However, this statement does not hold for the G4 method. The ccCA, G3, and G4 methods used in the Wilson study resulted in MAD's for the $\Delta H°_{f,298}{}'s$ of aromatic hydrocarbon of 2.88, 1.60, and 1.04 kcal mol^{-1}, respectively for RC2 and 0.79, 1.55, and 1.78 kcal mol^{-1}, respectively for RC3. These results show that RC3 is recommended for larger molecules, especially when using ccCA. Engelkemier and Windus[59] extended this hierarchy to calculated $\Delta H°_{f,298}{}'s$ of oxygen-containing organic molecules and showed the effectiveness of these reaction schemes in the cancellation of errors and in providing more accurate enthalpies even for large molecules such β-D-glucopyranose-gg.

Jorgensen and Wilson[40] published a detailed study of the effect of the hypohomodesmotic reaction scheme (RC3) when used in combination with ccCA, G3, and G4 for the prediction of $\Delta H°_{f,298}{}'s$ of organosulfur species and compared it with the atomization approach (RC0). In general, the RC3 reaction scheme did decrease the overall MAD of the $\Delta H°_{f,298}{}'s$ for ccCA, G3, and G4 as compared to the RC0 approach, though not significantly. For example, the MAD of the $\Delta H°_{f,298}{}'s$ of organosulfur species computed with ccCA-P is 0.98 kcal mol^{-1} using RC0 and 0.54 kcal mol^{-1} using RC3.[40] Thus, RC0 is still an effective method when using composite approaches such as ccCA, G3, and G4,[40,41] particularly for light atoms or/and small molecules but not necessarily for heavy elements or/and large molecules. However, the decrease in the MAD when using the RC3 scheme compared to the RC0 for the component methods that are used for the additive terms in the ccCA methodology is very significant (2.39 kcal mol^{-1} when using MP2/aug-cc-pVQZ to 78.11 kcal mol^{-1} when using MP2/aug-cc-pVDZ).[40]

In the present study, the homodesmotic hierarchy is used to predict $\Delta H°_{f,298}{}'s$ for selenium-containing organic compounds. The effect of RC2 and RC3 schemes on predicting the $\Delta H°_{f,298}{}'s$ of organoselenium molecules via ccCA, G3, G4, and B3PW91/aug-cc-pVTZ is investigated and compared to RC0 results. Due to the lack of reliable thermochemical properties of organoselenium species, the molecule set in this study is smaller than for the organosulfur study,[40] mentioned earlier. Additionally, the quality of the experimental $\Delta H°_{f,298}{}'s$ is also assessed due to the significant discrepancies between the reported experimental results. The performance of each individual step of ccCA, using RC2 and RC3 schemes, is also discussed. The study compares trends of the computational approaches used to calculate the $\Delta H°_{f,298}{}'s$ of chalcogen-containing hydrocarbon molecules (group 16 of the periodic table).

4.2 Computational Details

4.2.1 Methods

All calculations have been carried out using the Gaussian 09 software package.[60] The correlation consistent Composite Approach (ccCA), detailed in Chapter 2 Section 2.5.2 and elsewhere[35,36,38] and has been applied widely in prior studies,[40,41,47,61-63] were used to predict the $\Delta H°_{f,298}{}'s$ of organoselenium species. For molecules containing third row atoms (Ga-Kr), the atomic second-order spin orbit coupling is also added to the total ccCA atomic energies.[37] The valence correlation space includes the 3s, 3p, 4s, 3d, and 4p orbitals for selenium in all single point energy calculations within the ccCA methodology and the FC1 correlation space include all the electrons except the 1s electrons for selenium.[37]

The most commonly used composite methods, G3[44] and G4[34] were used for comparison. The hybrid density functional B3PW91[64,65] in conjunction with the aug-cc-pVTZ basis set was also used as it was found to provide accurate geometries and energies for organoselenium compounds when compared to results obtained using QCISD/cc-pVTZ.[26] The $\Delta H°_{f,298}{}'s$ of organoselenium compounds were also calculated using each level of theory that are components of the ccCA methodology. The mean absolute deviation (MAD) and the mean signed deviation (MSD) were both calculated for each method. The geometries and structural parameters of all molecules of interest are presented in the Appendix. The frequency calculations and the wave function stability tests were both used to ensure that the predicted closed-shell structures are all a stable minimum.

4.2.2 Thermochemistry

The $\Delta H°_{f,298}{}'s$ of organoselenium compounds were calculated using ccCA, G3, G4, and B3PW91 methods. Three thermochemical approaches were used in the calculations of the $\Delta H°_{f,298}{}'s$: the atomization approach (RC0), the isodesmic reaction scheme (RC2), and the hypohomodesmotic reaction scheme (RC3).

4.2.2.1 Atomization Approach (RC0)

In this method, the $\Delta H°_{f,298}{}'s$ were computed as follows:

$$\Delta H_{f,M}(298K) = \sum_{atoms} n\Delta H_{f,A}\,(0K) - \left(\sum_{atoms} nE_A - E_M - E_{ZPE}\right) + \left(H_M(298K) - H_M(0K)\right) - \left(\sum_{atoms} n\left(H_A(298K) - H_A(0K)\right)\right) \quad (4.1)$$

The enthalpy of formation of the molecule of interest (*M*) ($\Delta H_{f,M}$) at 298 K is calculated using Eq. 4.1. The first term in Eq. 4.1 is the experimental enthalpy of formation of its constituent atoms ($\Delta H_{f,A}$) at 0K multiplied by *n*, the number of each type of atom. The recommended experimental $\Delta H°_{f,0}$ of the selenium atom, 57.9 kcal mol^{-1},[66,67] was used in this study. Carbon and hydrogen $\Delta H°_{f,0}{}'s$ are the same as those used in Jorgensen's study,[40] which are 170.11 kcal mol^{-1} and 51.63 kcal mol^{-1},[68,69] respectively. The second term is the atomization energy of the molecule of interest ($D_0 = \sum_{atoms} nE_A - E_M - E_{ZPE}$), where E_A, E_M, and E_{ZPE} are the total energies of the constituent atoms, the total energy of the molecule of interest, and the zero point energy of the molecule of interest, respectively. The energies are calculated at the specified level of theory. The last two components are the thermal corrections to the enthalpies to account for a temperature of 298 K for the atoms (experimental) and for the molecule of interest, calculated at a specified level of theory. The thermal corrections to enthalpies for atoms are 1.32 kcal mol^{-1} for selenium,[66] 0.25 kcal mol^{-1} for carbon,[68] and 1.01 kcal mol^{-1} for hydrogen.[69]

4.2.2.2 Isodesmic (RC2) and Hypohomodesmotic (RC3) Reaction Schemes

The $\Delta H°_{f,298}{}'s$ were computed using the RC2 and RC3 reaction schemes as follows:

$$\Delta H_{f,M}(298K) = \sum_{product} \Delta H_{f,prod.}(298K) - \sum_{reactant} \Delta H_{f,react.}(298K) - \left(\sum_{product} H(298K) - \sum_{reactant} H(298K) \right) \quad (4.2)$$

In Eq. 4.2, the $\Delta H_{f,M}$ is calculated using the experimental $\Delta H_f(298K)$ of the elemental reactants and elemental products, i.e. the constituent molecules, and the calculated enthalpy of the reaction which is represented by the term $\left(\sum_{product} H(298K) - \sum_{reactant} H(298K)\right)$. Elemental reactants and products are molecules produced from the bond separation reaction (BSR)[55] of the target molecule and they must maintain all of the constraints of each given reaction scheme. The first step in thermochemical reaction schemes, such as RC2 and RC3, is to define these elemental reactants and products.

4.2.3 Organoselenium Compounds

A set of eight organoselenium molecules were selected based on the availability of experimental data. This set contains only carbon, selenium, and hydrogen atoms and consists of two constituent molecules dimethyl selenide ($(CH_3)_2Se$) and dimethyl diselenide ($(CH_3)_2Se_2$)), six target molecules divinyl selenide ($(CH_2{=}CH)_2Se$, diethyl selenide ($(CH_3CH_2)_2Se$), diethyl diselenide ($(CH_3CH_2)_2Se_2$), diisopropyl selenide ($((CH_3)_2CH)_2Se$)), dipropyl selenide ($(CH_3(CH_2)_2)_2Se$), dibutyl selenide ($(CH_3(CH_2)_3)_2Se$), and selenium dihydride (H_2Se). Aromatic molecules were not included in the set. The $\Delta H°_{f,298}{}'s$ for the set of molecules were calculated using the RC0, RC2, and RC3 approaches via ccCA, G3, G4, and B3PW91. In order to calculate

the $\Delta H°_{f,298}$ of the aliphatic organoselenium compounds using the RC2 and RC3 thermochemical reaction schemes, Wheeler's definition[57] of RC2 and RC3 was extended to include selenium-containing elemental reactants and products. That is, for RC2, the number and the bond type of Se-C and Se-Se bonds was conserved, and for RC3 the number, the bond type, and the hybridization state of selenium were all conserved. These elemental reactants and products are provided in Figure 4.1. The proposed RC2 and RC3 reactions are shown in Figures 4.2 and 4.3, respectively. In these reaction schemes, the uncertainties of the reported results are cumulative. Thus, a potential source of deviations in RC2 and RC3 schemes can come from the uncertainties associated with the experimental $\Delta H°_{f,298}{}'s$ of the constituent molecules involved in the proposed reaction schemes.

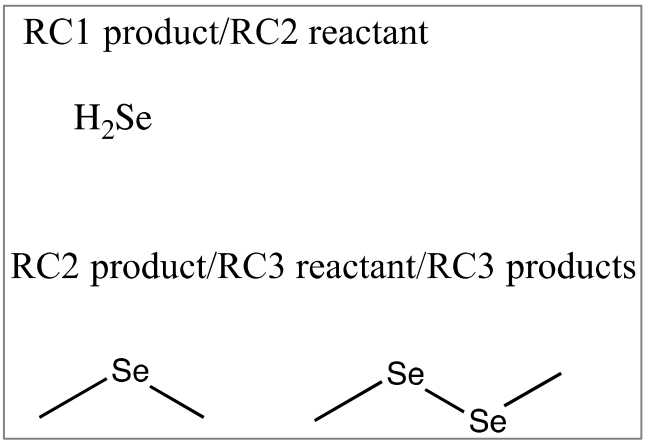

Figure 4.1 Selenium-containing elemental reactants and products.

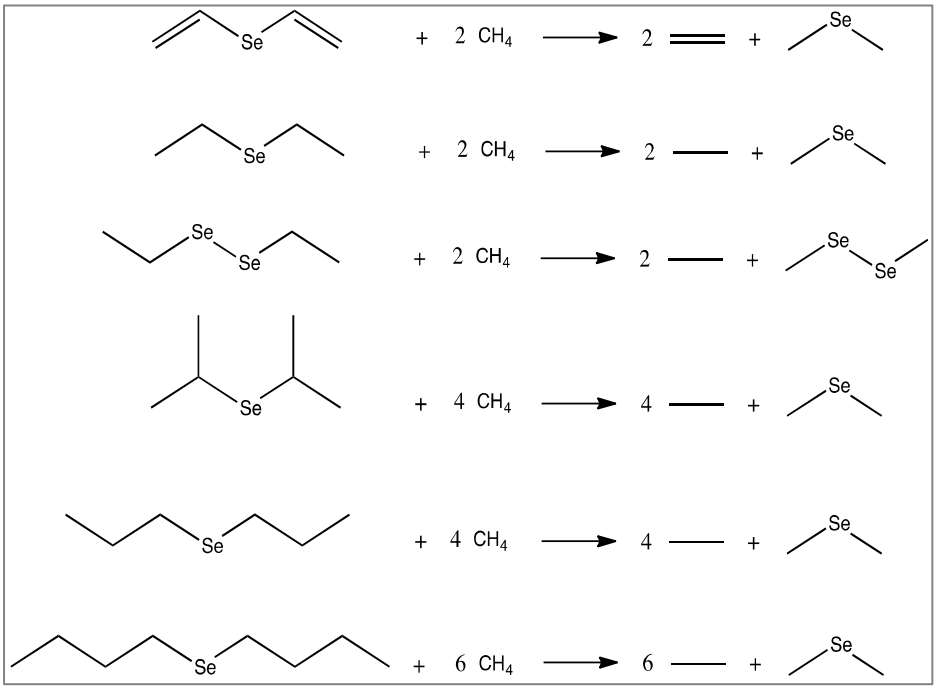

Figure 4.2 Isodesmic (RC2) reaction schemes.

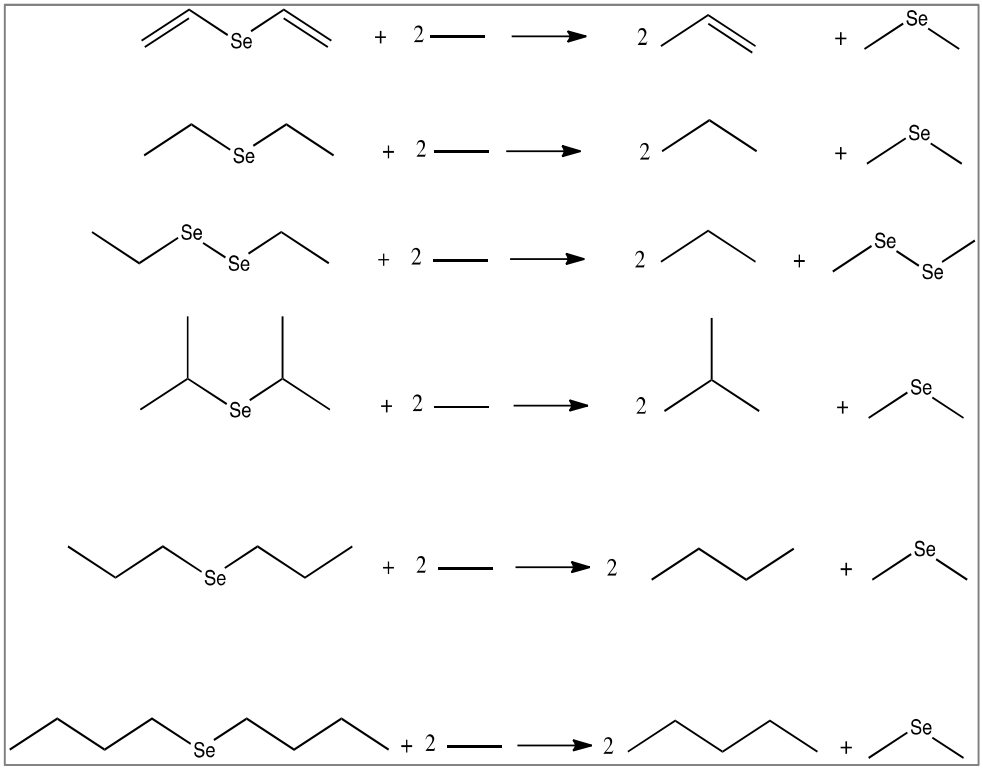

Figure 4.3 Hypohomodesmotic (RC3) reaction schemes.

4.2.4 Reference Data

The available experimental gas phase $\Delta H°_{f,298}{}'s$ of organoselenium molecules were considered as reference data. Due to the large discrepancies between experiments, the quantitative structure-property relationship (QSPR) $\Delta H°_{f,298}{}'s$ were also considered for evaluation purposes. QSPR is a semiempirical method developed to predict chemical and physical properties, such as $\Delta H°_{f,298}{}'s$ of organic and organometallic compounds, using numerical descriptors that generated from molecular structures and has been successfully applied for a variety of organic and organometallic compounds.[70-74] Shown in Table 4.2 are all available reference data categorized by the methods used for measurement.

All the experimental $\Delta H°_{f,298}{}'s$ of organoselenium compounds, provided in Table 4.2, were determined via thermochemical schemes relative to the selenium dioxide (SeO_2) combustion product. The reason for using the combustion procedure is because SeO_2 is the only metallic oxide that is produced from the burning of selenium and its compounds.[24] SeO_2 is soluble in water and to ensure its complete dissolution in water, a high precision measurement, such as the rotating bomb calorimetry, is often used. While rotating bomb calorimetry is a preferred experimental method, Batt[24] showed very good agreement between static and rotating bomb measurement of the $\Delta H°_{f,298}$ of SeO_2.

A review by Liebman and Slayden[21] of the evaluation of organoselenium compounds thermochemistry, as well as the $\Delta H°_{f,298}{}'s$ predicted by QSPR[74] were both used as a guidance in evaluating the reference data. Liebman and Slayden[21] evaluated the $\Delta H°_{f,298}{}'s$ of organoselenium compounds reported from two main calorimetric measurements: static bomb calorimetry performed by Tel'noi[23] and rotating bomb calorimetry performed by Voronkov.[22]

Liebman[21] used the well-established linear relationship, developed by Rossini et al.,[75-77] for the $\Delta H°_{f,298}{}'s$ of a set of homologous organic compounds, such as RZ and R_2Z where R is an alkyl group and Z is a heteroatom to examine the validity of the experimental $\Delta H°_{f,298}{}'s$ of the dialkyl selenides and to predict unknown $\Delta H°_{f,298}{}'s$ for other homologous organic compounds. It was found that the experimental $\Delta H°_{f,298}$ of $(CH_3)_2Se$ measured by Tel'noi[23] using static bomb calorimetry deviates from the Rossini linear relationship by ~3.12 kcal mol^{-1} – a deviation that is too large for reliability.[21] An $\Delta H°_{f,298}$ of -2.39 kcal mol^{-1} for $(CH_3)_2Se$ is suggested by Liebman to be more credible.[21] Using the QSPR approach, a value of -1.77 kcal mol^{-1} is predicted for the $\Delta H°_{f,298}$ of $(CH_3)_2Se$.[74] The QSPR $\Delta H°_{f,298}$ of $(CH_3)_2Se$ is near the value suggested by Liebman. Using the Rossini linear relationship, Liebman validated the $\Delta H°_{f,298}{}'s$ of -11.78±0.96 kcal mol^{-1} for $(CH_3CH_2)_2Se$, -25.81±0.96 kcal mol^{-1} for $((CH_3)_2CH)_2Se$, and -31.50±1.20 kcal mol^{-1} for $(CH_3(CH_2)_3)_2Se$; all were measured by Voronkov et al.[22] using rotating bomb calorimetry. The $\Delta H°_{f,298}$ of $(CH_3(CH_2)_2)_2Se$ was interpolated from this relationship to have a value of -21.75 kcal mol^{-1}. As shown in Table 4.2, the predicted $\Delta H°_{f,298}{}'s$ of these compounds using QSPR are most similar to those measured by Voronkov et al.[22]

The experimental $\Delta H°_{f,298}{}'s$ of dialkyl diselenides exhibit large discrepancies and high uncertainties, which precludes the potential of applying Rossini's linear relationship[75-77] to these compounds. Furthermore, no results from QSPR are available for dialkyl diselenids. For consistency, and since both $(CH_3)_2Se$ and $(CH_3)_2Se_2$ are considered constituent molecules, the $\Delta H°_{f,298}$ of $(CH_3)_2Se_2$, measured by Tel'noi[23] using the same experiment as $(CH_3)_2Se$, was estimated in the same manner as the $\Delta H°_{f,298}$ of $(CH_3)_2Se$ was estimated by Liebman.[21] The recommended $\Delta H°_{f,298}$ of $(CH_3)_2Se_2$ is ~6.22 kcal mol^{-1}. The experimental $\Delta H°_{f,298}{}'s$ of

$(CH_3CH_2)_2Se_2$ and $(CH_3(CH_2)_3)_2Se_2$ measured by Tel'noi et al.[23] using combustion procedure in a stationary bomb often are associated with high uncertainties as shown in Table 4.2. Liebman found that the slope of these two $\Delta H°_{f,298}{}'s$ versus the number of carbon atoms are in reasonable agreement with the slope for similar corresponding symmetrical n-alkanes.

The experimental $\Delta H°_{f,298}{}'s$ of divinyl selenide shown in Table 4.2 were measured with the static bomb[23] to be 49.71±1.90 kcal mol^{-1} and with the rotating bomb[22] to be 28.44±0.96 kcal mol^{-1}. The enthalpy of hydrogenation of divinyl selenide using the 49.71±1.90 kcal mol^{-1} value and the recommended $\Delta H°_{f,298}$ of diethyl selenide (-11.78±0.96 kcal mol^{-1})[21] is -30.71 kcal mol^{-1} per vinyl group which is very close to the enthalpy of hydrogenation of the corresponding alkene, 1,4-pentadiene, which is -30.11±0.15 kcal mol^{-1}.[78] However, the enthalpy of hydrogenation using the rotating bomb value (28.44±0.96 kcal mol^{-1}) is -20.08 kcal mol^{-1} per vinyl group which is much smaller than that of the corresponding alkene. Based on these values of the enthalpy of hydrogenation of divinyl selenide, the value 49.71±1.90 kcal mol^{-1} can be considered more reliable than 28.44±0.96 kcal mol^{-1}. Data shown in bold in Table 4.2 are considered to be the most reliable and are thus used as reference data in the present work.

Table 4.2 Experimental and estimated enthalpies of formation in kcal mol^{-1} for organoselenium compounds.[a,b]

	$\Delta H°_{f,298}{}'s$ (SBC)[c]	$\Delta H°_{f,298}{}'s$ (RBC)[d]	$\Delta H°_{f,298}{}'s$ (Estimated)[e]	$\Delta H°_{f,298}{}'s$ (QSPR)[f]
$(CH_3)_2Se$	4.3±1.90	-	**-2.39±1.90**	-1.77
$(CH_3)_2Se_2$	12.91±1.90	-0.72±0.96	**6.22±1.90**	-
$(CH_2=CH)_2Se$	**49.71±1.90**	28.44±0.96		
$(CH_3CH_2)_2Se$	-5.02±0.96	**-11.78±0.96**	-	-10.68
$(CH_3CH_2)_2Se_2$	**-3.82±2.87**	-9.08±0.96	-	-
$((CH_3)_2CH)_2Se$	-	**-25.81±0.96**	-	-21.82

Table 4.2 Continued.

$(CH_3(CH_2)_3)_2Se$	-	**-31.50±1.20**	-	-28.20
$(CH_3(CH_2)_4)_2Se$	-	**-41.28±1.20**	-	-37.08
$(CH_3(CH_2)_3)_2Se_2$	**-21.03±5.02**	-	-	-
$(CH_3(CH_2)_2)_2Se$	-	-	**-21.75±0.96**	-

[a]SBC stands for static bomb calorimetry, RBS stands for rotating bomb calorimetry, estimated values are obtained based on the Rossini linear relationship, QSPR stands for the quantitative structure-property relationships.

[b]Data shown in bold are considered to be the most reliable and are thus used as reference data in the present work.

[c]Reference. 23. [d]Reference. 22. [e]Reference. 22. [f]Reference. 74.

4.3 Results and Discussion

The $\Delta H°_{f,298}{}'s$ of the constituent fragments shown in Figure 4.1 were calculated using the atomization approach (RC0) via ccCA-P, ccCA-S3, ccCA-S4, ccCA-PS3, G3, G4, and B3PW91/aug-cc-pVTZ and presented in Table 4.3. The calculated $\Delta H°_{f,298}{}'s$ of the hydrocarbon fragments are shown in Table 4.4, as they were calculated using ccCA, G3, and G4 in previous studies.[40,41]

Table 4.3 Calculated enthalpies of formation (in kcal mol^{-1}) for the elemental products and reactants of organoselenium compounds via the atomization approach (RC0).

	ccCA-P	**ccCA-S3**	**ccCA-S4**	**ccCA-PS3**	**G3**	**G4**	**B3PW91/ aVTZ[a]**	**Expt.**
H_2Se	7.19	6.85	7.16	7.02	7.91	8.12	6.75	7.03±0.190[b]
$(CH_3)_2Se$	0.93	-0.34	0.82	0.29	0.90	1.38	2.54	-2.39± 1.90[c]
$(CH_3)_2Se_2$	7.19	5.65	7.12	6.42	7.04	8.02	5.28	6.22± 1.90[c]

[a] aVTZ: aug-cc-pVTZ. [b]Reference 79. [c]Reference 21.

The calculated $\Delta H°_{f,298}'s$ of selenide dihydride (H_2Se) are in relatively good agreement with the experimental value for all computational methods employed. All ccCA variants predict a $\Delta H°_{f,298}$ for H_2Se that is within the experimental uncertainty. G3 and G4 both lead to an underestimate of the $\Delta H°_{f,298}$ of H_2Se by ~1.0 kcal mol^{-1} with respect to experiment, while B3PW91 overestimates by 0.1 kcal mol^{-1}. The $\Delta H°_{f,298}'s$ of dimethyl selenide ($(CH_3)_2Se$) calculated using the current composite methods are all off the reference value by 2.05 kcal mol^{-1} to 4.93 kcal mol^{-1}, with ccCA-S3 being the closet to the reference value (0.15 kcal mol^{-1} off the error bar). The $\Delta H°_{f,298}$of $(CH_3)_2Se$ predicted using the QSPR approach (-1.77 kcal mol^{-1})[74] is in good agreement with the -2.39±1.90 kcal mol^{-1} suggested by Liebman. The calculated $\Delta H°_{f,298}'s$ of dimethyl diselenide ($(CH_3)_2Se_2$) all agree well with the value suggested by Liebman.

Table 4.4 Calculated enthalpies of formation (in kcal mol^{-1}) for the hydrocarbon fragments via the atomization approach (RC0).

	ccCA-P	**ccCA-S3**	**ccCA-S4**	**ccCA-PS3**	**G3**	**G4**	**B3PW91/ aVTZ[a]**	**Expt.[b]**
CH_4	-17.93	-18.53	-18.00	-18.23	-18.02	-17.74	-16.92	-17.82±0.07
CH_3CH_3	-20.15	-21.21	-20.27	-20.68	-20.12	-19.71	-19.61	-20.03±0.05
$CH_2=CH_2$	12.82	11.93	12.78	12.37	12.61	12.68	12.56	12.6±0.1
$CH_3CH_2CH_3$	-24.98	-26.50	-25.14	-25.74	-24.93	-24.45	-23.95	-25.0±0.1
$CH_3CH=CH_3$	5.33	4.24	5.24	4.65	5.13	5.21	4.33	4.8±0.2
$(CH_3)_3CH$	-31.70	-33.66	-31.90	-32.68	-31.78	-31.34	-29.11	-32.1±0.2
$CH_3(CH_2)_2CH_3$	-29.51	-31.48	-29.72	-30.50	-29.86	-29.35	-28.23	-30.0±0.2
$CH_3(CH_2)_3CH_3$	-34.28	-36.70	-34.53	-35.49	-34.79	-34.25	-32.45	-35.1±0.2

[a] aVTZ= aug-cc-pVTZ. [b]Reference 80.

4.3.1 Atomization Approach Using Composite Methods and B3PW91

The $\Delta H°_{f,298}{}'s$ of the six target organoselenium molecules were calculated using the atomization approach (RC0) via the ccCA-P, ccCA-S3, ccCA-S4, ccCA-PS3, G3, G4, and B3PW91/aug-cc-pVTZ methods and are presented in Table 4.5 as well as the corresponding experimental $\Delta H°_{f,298}{}'s$, MADs, and MSDs. The calculated $\Delta H°_{f,298}{}'s$ of divinyl selenide for all methods shown in Table 4.4 are closer to the static bomb measured[23] value of 49.71±1.90 kcal mol^{-1} than the rotating bomb measured[22] value of 28.4±1.0 kcal mol^{-1}. This comes as a support to the evaluation of the static bomb measured value being more reliable based on its enthalpy of hydrogenation. ccCA-S3 resulted in a $\Delta H°_{f,298}$ that is the closest to the experimental value with a deviation of only 0.14 kcal mol^{-1}. All other methods predicted a $\Delta H°_{f,298}$ of divinyl selenide that is within 1.1 to 2.0 kcal mol^{-1} from experiment, yet the $\Delta H°_{f,298}{}'s$ calculated using the G4 and B3PW91 methods are greater by 4.19 and 3.01 kcal mol^{-1}, respectively, from the experiment. The calculated $\Delta H°_{f,298}$ of diethyl selenide is best predicted by ccCA-S3 with only 0.36 kcal mol^{-1} difference from the experimental value recommend by Liebman (-11.78±0.96 kcal mol^{-1}).[21] Jover et al.[74] also predicted a $\Delta H°_{f,298}$ of -10.68 kcal mol^{-1} for diethyl selenide using the QSPR approach, which is in good agreement with Liebman's recommended value. G3 and G4 deviate by 2.48 and 3.17 kcal mol^{-1}, respectively, from the experiment. The B3PW91 functional predicts a $\Delta H°_{f,298}$ that is 4.04 kcal mol^{-1} greater than the experimental value.

The computed $\Delta H°_{f,298}{}'s$ of diethyl diselenide all deviate less than 1.0 kcal mol^{-1} from experiment except the $\Delta H°_{f,298}$ predicted by ccCA-S3 and ccCA-PS3 that deviates by 3.24 and 2.02 kcal mol^{-1} from experiment, which is close to the experimental uncertainty. The $\Delta H°_{f,298}$ of diisopropyl selenide calculated using the ccCA-P is the closest to the experiment among the

other ccCA variants, followed by ccCA-S4. G3 predicts an $\Delta H°_{f,298}$ that is 2.54 kcal mol^{-1} away from the experiment. B3PW91 results in an $\Delta H°_{f,298}$ that is 9.28 kcal mol^{-1} lower than the experiment. For dipropyl selenide, ccCA-P predicts the closest value to the Liebman's interpolated value[21] (-21.75 ± 0.96 kcal mol^{-1}). For dibutyl selenide, G3 predicts the closest $\Delta H°_{f,298}$ to the experimental value, i.e. 1.78 kcal mol^{-1} lower than the experiment.

Overall, the ccCA-P, ccCA-S4, and G3 methods using the RC0 approach result in $\Delta H°_{f,298}{}'s$ with MADs of 1.68, 1.70, and 1.74 kcal mol^{-1}, respectively, showing very good agreement with the experiment with an average uncertainty of 1.53 kcal mol^{-1}. ccCA-S3, in contrast, results in a MAD of 3.10 kcal mol^{-1} and underestimates $\Delta H°_{f,298}{}'s$ with a MSD of 2.93 kcal mol^{-1}, as shown in Table 5.4. Previous ccCA studies[38,40,41] found a similar underestimation in the computed $\Delta H°_{f,298}{}'s$ when using ccCA-S3, which utilizes the Schwartz-3 extrapolation scheme.[81] Due to this large underestimation of ccCA-S3, ccCA-PS3 results in a MAD of 2.53 kcal mol^{-1}. The G4 method results in MAD of 2.85 kcal mol^{-1} and an overestimation of -2.85 kcal mol^{-1} for the $\Delta H°_{f,298}{}'s$ of organoselenium compounds, demonstrating a lower accuracy than ccCA-P, ccCA-S4, and G3. B3PW91/aug-cc-pVTZ has the largest MAD with an overall overestimation of the $\Delta H°_{f,298}{}'s$ of organoselenium compounds. Overall, the ccCA-P variant predicts the best agreement with the experiment using RC0 scheme for the $\Delta H°_{f,298}{}'s$ of organoselenium compounds. For organoselenium compounds containing more than six non-hydrogen atoms, the MP2-DK/aug-cc-pVTZ-DK calculation results in wrong electronic states; hence this contribution was removed from the ccCA energy for these molecules. It is known that this contribution becomes small with increasing the molecular size.

Table 4.5 Calculated enthalpies of formation (in kcal mol^{-1}) for target organoselenium molecules via atomization approach (RC0).

	ccCA-P	ccCA-S3	ccCA-S4	ccCA-PS3	G3	G4	B3PW91/aug-cc-pVTZ	Expt.
$(CH_2=CH)_2Se$	51.69	49.85	51.66	50.77	50.81	53.9	52.72	**49.71±1.90**[a] 28.44±0.96[b]
$(CH_3CH_2)_2Se$	-9.25	-11.42	-10.34	-9.47	-9.3	-8.61	-7.74	**-11.78±0.96**[b] -5.02±0.96[a] -10.68[c]
$(CH_3CH_2)_2Se_2$	-4.62	-7.06	-4.8	-5.84	-4.22	-2.98	-4.12	**-3.82±2.87**[a] -9.08±0.96[b]
$((CH_3)_2CH)_2Se$	-26.59	-29.63	-26.9	-28.12	-23.27	-22.40	-16.53	**-25.81±0.96**[b] -21.82[c]
$(CH_3(CH_2)_2)_2Se$	-23.47	-26.54	-23.78	-25	-19.59	-18.84	-16.21	**-21.75±0.96**[d]
$(CH_3(CH_2)_3)_2Se$	-33.77	-37.73	-34.18	-35.75	-29.72	-28.94	-24.71	**-31.50±1.20**[b] -28.20[c]
MAD	1.68	3.10	1.70	2.53	1.74	2.85	4.83	
MSD	0.18	2.93	0.57	1.41	-1.61	-2.85	-4.73	

[a]Reference 23. [b]Reference 22. [c]Reference 74. [d]Reference 21.

4.3.2 Homodesmotic Approach Using Composite Methods and B3PW91

The calculated $\Delta H°_{f,298}{}'s$ of organoselenium compounds using the isodesmotic reaction scheme (RC2) and the hypohomodesmotic reaction scheme (RC3) via composite methods (ccCA variants, G3, and G4) and B3PW91/aug-cc-pVTZ are presented in Tables 4.6 and 4.7, respectively. Overall, the MADs of all the composite methods were reduced when using the RC2 and RC3 schemes compared to the MADs obtained using the RC0 approach. The MADs of the $\Delta H°_{f,298}{}'s$ calculated by B3PW91/aug-cc-pVTZ using the RC2 scheme was not significantly reduced in comparison to the MAD using the RC0 approach, i.e. 4.83 vs. 4.23 kcal mol^{-1}. Nevertheless, the MAD obtained with B3PW91/aug-cc-pVTZ was decreased to 0.76 kcal mol^{-1} when using the RC3 reaction scheme compared with the RC0 scheme. The calculated $\Delta H°_{f,298}{}'s$ of the principle organoselenium molecules using RC2 and RC3 via ccCA variants lie within the experimental uncertainties of the corresponding experimental values. The most notable decrease in the MADs of the ccCA variants occurs for the MAD of the ccCA-S3 $\Delta H°_{f,298}{}'s$, i.e. from 3.10 (RC0) to 0.92 (RC2) and to 1.22 kcal mol^{-1} (RC3) as shown in Table 4.8.

The differences between the MAD and the MSD of the $\Delta H°_{f,298}{}'s$ calculated using all four ccCA variants become negligible when using the RC2 and RC3 schemes, thus exhibiting less dependency on the extrapolation schemes. The MAD of all four ccCA variants is reduced to ~0.93 kcal mol^{-1} when using the RC2 scheme and to ~1.24 kcal mol^{-1} using the RC3 scheme. Compared to the RC0 approach, the MAD of the $\Delta H°_{f,298}{}'s$ calculated using G3 was reduced by 0.17 kcal mol^{-1} when using the RC2 scheme and increased by 0.04 kcal mol^{-1} when using the RC3 approach. On the other hand, G4 results in a larger decrease in the MAD of the $\Delta H°_{f,298}{}'s$ of organoselenuim compounds when using RC2 and RC3 compared with G3, i.e. from 2.85

(RC0) to 1.47 (RC2) and 1.29 kcal mol^{-1} (RC3). The MSDs of the calculated $\Delta H°_{f,298}{}'s$ were reduced for all composite methods when using RC2 scheme compared to RC0, showing a reduction of statistical bias, i.e. the method neither overestimates nor underestimates, which increases the validity of the utilized method. Using the RC3 scheme, compared to RC0, the reduction of the MSD for all the composite methods is inconsistent. The MSDs of ccCA-S3, ccCA-SP3, and G4 were reduced when using RC3 compared to RC0, but they were increased for ccCA-P, ccCA-S4 and G3. However, the MSD for the set of $\Delta H°_{f,298}{}'s$ of all four ccCA variants is ~0.1 kcal mol^{-1} when using the RC2 scheme and ~0.8 kcal mol^{-1} when using the RC3 scheme. The MAD and the MSD of G3 for each scheme (RC2 and RC3) have the same value; in this case, the MSD becomes insignificant. The MSD of the $\Delta H°_{f,298}{}'s$ calculated using G4 was reduced to 1.33 kcal mol^{-1} when using the RC2 and to 1.21 kcal mol^{-1} when using RC3 in comparison to the RC0 approach. It is worth mentioning here that the average experimental uncertainty in the target molecules is ±1.53 kcal mol^{-1} and the average experimental uncertainty in the constituent molecules used for the RC2 scheme is ±1.41 kcal mol^{-1} and ±1.39 kcal mol^{-1} for the RC3 scheme. All composite methods have a MAD that is within these uncertainties when using RC2 and RC3. However, B3PW91 has an MAD that is within the average experimental uncertainties only when using the RC3 scheme.

Apart from that of G4, the largest deviation when using RC2 and RC3 schemes via composite methods is found for the $\Delta H°_{f,298}$ of divinyl selenid, a conjugated system, with deviations of -1.98 (-1.34), -2.00 (-1.36), -1.99 (-1.36), -1.99 (-1.35), and 2.13 (2.56) kcal mol^{-1} for ccCA-P, ccCA-S3, ccCA-S4, ccCA-PS3, and G3 when using RC2 (RC3), respectively. Jorgensen[40] found a similar large deviation in excess of 1.0 kcal mol^{-1} of the MADs of $\Delta H°_{f,298}{}'s$ of organosulfur compounds containing π-bonds calculated using ccCA variants and

G3 methods using RC0 and RC3. Additionally, the same observation was found when calculating the $\Delta H°_{f,298}{}'s$ of hydrocarbons containing double bonds using ccCA variants and G3 via RC2 and RC3 schemes by Wilson.[41] Compounds containing more than six non-hydrogen atoms have also displayed large deviations in the MAD of their $\Delta H°_{f,298}{}'s$ calculated using the composite methods via RC2 and RC3 schemes with respect to experiments.[40,41] A similar statement can be true here for organoselenium compounds particularly when using RC3 scheme.

Table 4.6 Calculated enthalpies of formation (in kcal mol^{-1}) for target molecules via the isodesmic approach (RC2).

	ccCA-P	ccCA-S3	ccCA-S4	ccCA-PS3	G3	G4	B3PW91/aug-cc-pVTZ	Expt.
$(CH_2=CH)_2Se$	51.69	51.71	51.7	51.7	47.58	50.13	51.69	**49.71±1.90**[a] 28.44±0.96[b]
$(CH_3CH_2)_2Se$	-12.31	-12.28	-12.32	-12.29	-12.8	-12.87	-9.68	**-11.78±0.96**[b] -5.02±0.96[a] -10.68[c]
$(CH_3CH_2)_2Se_2$	-5.39	-5.36	-5.4	-5.37	-5.25	-5.26	-2.2	**-3.82±2.87**[a] -9.08±0.96[b]
$((CH_3)_2CH)_2Se$	-25.35	-25.27	-25.36	-25.31	-26.99	-27.14	-17.5	**-25.81±0.96**[b] -21.82[c]
$(CH_3(CH_2)_2)_2Se$	-22.23	-22.18	-22.24	-22.2	-23.31	-23.59	-17.17	**-21.75±0.96**[d]
$(CH_3(CH_2)_3)_2Se$	-32.10	-32.01	-32.11	-32.05	-33.65	-34.17	-24.7	**-31.50±1.20**[b] -28.20[c]
MAD	0.94	0.92	0.94	0.93	1.58	1.47	4.23	
MSD	0.12	0.07	0.13	0.10	1.58	1.33	-4.23	

[a]Reference 23. [b]Reference 22. [c]Reference 74. [d]Reference 21.

Table 4.7 Calculated enthalpies of formation (in kcal mol^{-1}) for target molecules via the hypohomodesmotic approach (RC3).

	ccCA-P	ccCA-S3	ccCA-S4	ccCA-PS3	G3	G4	B3PW91/aug-cc-pVTZ	Expt.
$(CH_2=CH)_2Se$	51.05	51.07	51.07	51.06	47.15	49.95	51.59	**49.71±1.90**[a] 28.44±0.96[b]
$(CH_3CH_2)_2Se$	-12.62	-12.61	-12.63	-12.61	-12.92	-12.84	-11.92	**-11.78±0.96**[b] -5.02±0.96[a] -10.68[c]
$(CH_3CH_2)_2Se_2$	-5.7	-5.68	-5.72	-5.69	-5.37	-5.23	-4.44	**-3.82±2.87**[a] -9.08±0.96[b]
$((CH_3)_2CH)_2Se$	-26.46	-26.42	-26.48	-26.44	-27.37	-27.04	-24.58	**-25.81±0.96**[b] -21.82[c]
$(CH_3(CH_2)_2)_2Se$	-22.79	-22.78	-22.81	-22.79	-23.34	-23.28	-21.82	**-21.75±0.96**[d]
$(CH_3(CH_2)_3)_2Se$	-33.18	-33.15	-33.19	-33.16	-33.81	-33.77	-32.09	**-31.50±1.20**[b] -28.20[c]
MAD	1.24	1.22	1.26	1.23	1.79	1.29	0.76	
MSD	0.79	0.77	0.80	0.78	1.79	1.21	-0.28	

[a]Reference 23. [b]Reference 22. [c]Reference 74. [d]Reference 21.

Table 4.8 Overall differences between RC0, RC2, and RC3 using composite methods and B3PW91.

	ccCA-P	ccCA-S3	ccCA-S4	ccCA-PS3	G3	G4	B3PW91/aug-cc-pVTZ
RC0							
MAD	1.68	3.10	1.70	2.53	1.74	2.85	4.83
MSD	0.18	2.93	0.57	1.41	-1.61	-2.85	-4.73
RC2							
MAD	0.94	0.92	0.94	0.93	1.58	1.47	4.23
MSD	0.12	0.07	0.13	0.09	1.58	1.33	-4.23
RC3							
MAD	1.24	1.22	1.26	1.23	1.79	1.29	0.76
MSD	0.79	0.77	0.80	0.78	1.79	1.21	-0.28
RC2-RC0							
Diff.	-0.74	-2.18	-0.75	-1.61	-0.17	-1.38	-0.60
RC3-RC0							
Diff.	-0.44	-1.87	-0.44	-1.30	0.04	-1.56	-4.07
RC2-RC3							
Diff.	0.30	0.30	0.31	0.31	0.21	-0.18	-3.48

4.3.3 Atomization Approach Using Single Point Energies within the ccCA Method

The single point calculations involved within the ccCA methodology were utilized to calculate the $\Delta H°_{f,298}{}'s$ of the target molecules in order to assess the effect of the thermochemical approaches on the level of theory utilized within the ccCA method. That is the $\Delta H°_{f,298}{}'s$ of organoselenium compounds were calculated using the RC0 approach via B3LYP/cc-pVTZ, MP2/aug-cc-pVDZ, MP2/aug-cc-pVTZ, MP2/aug-cc-pVQZ, CCSD(T)/cc-pVTZ, MP2(FC1)/aug-cc-pCVTZ, and MP2/cc-pVTZ using the B3LYP/cc-pVTZ geometries and frequencies. The resulted $\Delta H°_{f,298}{}'s$ are displayed in Table 4.9.

It is evident from the results shown in Table 4.9 that the size of the basis set employed plays an important role in predicting accurate $\Delta H°_{f,298}{}'s$ of organoselenium compounds when using RC0. The $\Delta H°_{f,298}{}'s$ calculated at the MP2/aug-cc-pVDZ level of theory, which involves the smallest basis set utilized within ccCA methodology, have the largest MAD of 88.55 kcal mol^{-1}, whereas the $\Delta H°_{f,298}{}'s$ calculated at the MP2/aug-cc-pVQZ level of theory, which is the largest basis set utilized within ccCA methodology, are the closest to experiment with a MAD of 1.91 kcal mol^{-1}. Thus, these calculations are very sensitive to the basis set size, which also was seen when calculating the $\Delta H°_{f,298}{}'s$ of organosulfur compounds using the same level of theories via the RC0 approach.[40] However, this trend was not obtained when utilizing the same methods for a set of hydrocarbon compounds.[41] The MAD of MP2/cc-pVTZ is lower than when using CCSD(T) with the same basis set by 14.37 kcal mol^{-1}, indicative of an outperforming of MP2 compared to CCSD(T) for this set of molecules. Moreover, the CCSD(T)/cc-pVTZ calculations result in a large deviation from experiment, with a MAD of 40.82 kcal mol^{-1}. Less than half the

Table 4.9 Calculated enthalpies of formation (in kcal mol^{-1}) for the target molecules via the atomization approach (RC0) using the specified level of theory at the B3LYP/cc-pVTZ geometry.[a]

	B3LYP/ VTZ	**MP2/ aVDZ**	**MP2/ aVTZ**	**MP2/ aVQZ**	**CCSD(T)/ VTZ**	**MP2(FC1)/ aCVTZ**	**MP2/ VTZ**	**Expt.**
$(CH_2=CH)_2Se$	61.08	108.8	60.45	46.97	82.73	54.25	66.42	**49.71±1.90**[b] 28.44±0.96[c]
$(CH_3CH_2)_2Se$	-0.11	61.15	4.72	-9.56	20.37	-1.57	11.77	**-11.78±0.96**[c] -5.02±0.96[b] -10.68[d]
$(CH_3CH_2)_2Se_2$	5.67	70.61	8.66	-7.79	28.64	-0.13	17.48	**-3.82±2.87**[b] -9.08±0.96[c]
$((CH_3)_2CH)_2Se$	-4.28	72.81	-5.14	-25.04	20.19	-13.57	4.8	**-25.81±0.96**[c] -21.82[d]
$(CH_3(CH_2)_2)_2Se$	-4.08	77.97	-1.21	-21.36	22.76	-9.2	8.25	**-21.75**±0.96[e]
$(CH_3(CH_2)_3)_2Se$	-8.08	95.01	-6.89	-32.86	25.27	-16.53	5.01	**-31.50±1.20**[c] -28.20[d]
MAD	15.86	88.55	17.59	1.91	40.82	9.70	26.45	
MSD	-15.86	-88.55	-17.59	0.78	-40.82	-9.70	-26.45	

[a]VTZ: cc-pVTZ, aVDZ: aug-cc-pVDZ, aVTZ: aug-cc-pVTZ, aVQZ: aug-cc-pVQZ, aCVTZ: aug-cc-pCVTZ. [b]Reference 23. [c]Reference 22. [d]Reference 74. [e]Reference 21.

deviation is found when using the MP2/aug-cc-pVTZ level of theory, emphasizing the importance of using diffuse basis functions (aug-) for such systems. The calculations of $\Delta H°_{f,298}{}'s$ using RC0 via these single point calculations not only are highly sensitive to the basis set, but also to the method of choice. The second best performing method among the single point calculations is the MP2(FC1)/aug-cc-pCVTZ method/basis set combination with a MAD of 9.70 kcal mol^{-1}, which improves upon the MP2/aug-cc-pVTZ results by 7.89 kcal mol^{-1}.

Due to the differential correlation effect that can affect the atomization approach, both the inclusion of more functions and/or the inclusion of the core-core and core-valence correlation functions can minimize the error associated with the differential correlation effect. All the results shown in Table 4.9 indicate that MP2 is highly dependent on the basis set size and a large basis set is crucial to obtain accurate $\Delta H°_{f,298}{}'s$ of organoselenium species. The basis set effects can be accounted for by extrapolating the energies to the complete basis set limit, as is done in the ccCA method, e.g. MAD of ccCA-P is lower than the MAD of MP2/aug-cc-pVQZ level of theory by 0.23 kcal mol^{-1}. The MAD of the $\Delta H°_{f,298}{}'s$ of organoselenium compounds calculated using B3LYP/cc-pVTZ results in a MAD of 15.86 kcal mol^{-1} when using RC0. It is shown in Table 4.9 that the deviation between theory and experiments increases with increasing molecular size. All single point energy calculations, except MP2/aug-cc-pVQZ, tend to overestimate the $\Delta H°_{f,298}{}'s$ of organoselenium compounds when using the RC0 approach compared to experiment as seen from the MSDs shown in Table 4.9 The MP2/aug-cc-pVQZ method shows a tendency for underestimation with a MSD of 0.78 kcal mol^{-1} which agrees with the findings from Jorgensen's study of organosulfur species.[40]

4.3.4 Homodesmotic Approach Using Single Point Energies within the ccCA Method

Shown in Table 4.10 and Table 4.11 are the $\Delta H°_{f,298}{}'s$ calculated using the isodesmic reaction scheme (RC2) and the hypohomodesmotic reaction scheme (RC3) via the single point calculations involved within the ccCA methodology, respectively. The MADs of the $\Delta H°_{f,298}{}'s$ calculated via the constituent energy calculations when using the thermochemical reaction schemes (RC2 and RC3) compared to the RC0 approach were dramatically decreased, i.e. by about 0.49-85.26 kcal mol^{-1} for RC2 and about 0.67-86.27 kcal mol^{-1} for RC3, as shown in Tables 4.12. This reduction of the MADs for these levels of theory when using the RC2 and RC3 reaction schemes, shown in Table 4.12, is more significant than the impacts of the RC2 and RC3 schemes on the MADs of the composites methods when compared to RC0 as shown in Table 4.8. This difference is justified because the composite methods tend to recover more correlation energy than a single point energy calculation, reducing the differential correlation effect and resulting in good agreement with experimental $\Delta H°_{f,298}{}'s$ when using the RC0 approach as shown in Table 4.5.

The largest MAD of the calculated $\Delta H°_{f,298}{}'s$ when using RC0 is 88.55 kcal mol^{-1} obtained with the MP2/aug-cc-pVDZ level of theory. This MAD was lowered to 3.29 and 2.28 kcal mol^{-1} when using RC2 and RC3, respectively. The RC2 and RC3 strategies cancel most of the errors originating from the differential correlation effect and size extensivity by constructing error balanced reaction schemes. Thus, by using these reaction schemes as well as the experimental $\Delta H°_{f,298}{}'s$ of the constituent molecules to calculate $\Delta H°_{f,298}{}'s$, the deviation between theory and experiment is reduced. RC2 and RC3 exhibit less dependency on the basis set size, as largely is the case when using the RC0 approach. To illustrate, the MADs for the $\Delta H°_{f,298}{}'s$ of MP2/aug-cc-pVDZ, MP2/aug-cc-pVTZ, and MP2/aug-cc-pVQZ when using the

Table 4.10 Calculated enthalpies of formation (in kcal mol^{-1}) for the target molecules via isodesmic reaction approach (RC2) using the level of theories specified in the table, at the B3LYP/cc-pVTZ geometry.[a]

	B3LYP/ VTZ	**MP2/ aVDZ**	**MP2/ aVTZ**	**MP2/ aVQZ**	**CCSD(T)/ VTZ**	**MP2(FC1)/ aCVTZ**	**MP2/ VTZ**	**Expt.**
$(CH_2=CH)_2Se$	52.17	49.95	49.91	49.87	51.94	49.52	49.71	**49.71±1.90**[b] 28.44±0.96[c]
$(CH_3CH_2)_2Se$	-9.51	-13.87	-13	-12.73	-11.43	-13.58	-12.42	**-11.78±0.96**[c] -5.02±0.96[b] -10.68[d]
$(CH_3CH_2)_2Se_2$	-1.96	-7.69	-6.35	-5.98	-4.38	-7.09	-5.6	**-3.82±2.87**[b] -9.08±0.96[c]
$((CH_3)_2CH)_2Se$	-17.14	-30.54	-27.83	-27.1	-23.78	-29.04	-26.34	**-25.81±0.96**[c] -21.82[d]
$(CH_3(CH_2)_2)_2Se$	-16.94	-25.38	-23.9	-23.41	-21.21	-24.68	-22.88	**-21.75±0.96**[e]
$(CH_3(CH_2)_3)_2Se$	-24.4	-36.66	-34.55	-33.8	-30.87	-35.47	-33.07	**-31.50±1.20**[c] -28.20[d]
MAD	4.53	3.29	1.86	1.42	1.06	2.57	0.94	
MSD	-4.53	3.21	1.80	1.37	-0.87	2.57	0.94	

[a]VTZ: cc-pVTZ, aVDZ: aug-cc-pVDZ, aVTZ: aug-cc-pVTZ, aVQZ: aug-cc-pVQZ, aCVTZ: aug-cc-pCVTZ. [b]Reference 23. [c]Reference.22. [d]Reference 74. [e]Reference 21.

Table 4.11 Caculated enthalpies of formation (in kcal mol^{-1}) for the target molecules via hypohomodesmotic reaction approach (RC3) using the level of theories specified in the table, at the B3LYP/cc-pVTZ geometry.[a]

	B3LYP/ VTZ	MP2/ aVDZ	MP2/ aVTZ	MP2/ aVQZ	CCSD(T)/ VTZ	MP2(FC1)/ aCVTZ	MP2/ VTZ	Expt.
$(CH_2=CH)_2Se$	51.65	49.84	50.49	50.39	51	50.22	50.03	**49.71±1.90**[b] 28.44±0.96[c]
$(CH_3CH_2)_2Se$	-11.73	-13.37	-12.75	-12.56	-11.99	-13.25	-12.45	**-11.78±0.96**[c] -5.02±0.96[b] -10.68[d]
$(CH_3CH_2)_2Se_2$	-4.18	-7.18	-6.11	-5.82	-4.93	-6.76	-5.63	**-3.82±2.87**[b] -9.08±0.96[c]
$((CH_3)_2CH)_2Se$	-24.33	-28.72	-27.1	-26.62	-25.52	-28.1	-26.41	**-25.81±0.96**[c] -21.82[d]
$(CH_3(CH_2)_2)_2Se$	-21.65	-24.14	-23.28	-23.01	-22.27	-23.87	-22.91	**-21.75±0.96**[e]
$(CH_3(CH_2)_3)_2Se$	-31.9	-34.82	-33.73	-33.39	-32.66	-34.37	-33.3	**-31.50±1.20**[c] -28.20[d]
MAD	0.72	2.28	1.52	1.24	0.76	2.03	1.06	
MSD	-0.47	2.24	1.26	1.01	0.24	1.86	0.95	

[a]VTZ: cc-pVTZ, aVDZ: aug-cc-pVDZ, aVTZ: aug-cc-pVTZ, aVQZ: aug-cc-pVQZ, aCVTZ: aug-cc-pCVTZ. [b]Reference 23. [c]Reference 22. [d]Reference 74. [e]Reference 21.

Table 4.12 Overall differences between RC0, RC2, and RC3 using the level of theories specified in the table.[a]

	B3LYP/ VTZ	MP2/ aVDZ	MP2/ aVTZ	MP2/ aVQZ	CCSD(T)/ VTZ	MP2(FC1)/ aCVTZ	MP2/ VTZ
RC0							
MAD	15.86	88.55	17.59	1.91	40.82	9.70	26.45
MSD	-15.86	-88.55	-17.59	0.78	-40.82	-9.70	-26.45
RC2							
MAD	4.53	3.29	1.86	1.42	1.06	2.57	0.94
MSD	-4.53	3.21	1.80	1.37	-0.87	2.57	0.94
RC3							
MAD	0.72	2.28	1.52	1.24	0.76	2.03	1.06
MSD	-0.47	2.24	1.26	1.01	0.24	1.86	0.95
RC2-RC0							
Diff.	-11.33	-85.26	-15.73	-0.49	-39.76	-7.14	-25.51
RC3-RC0							
Diff.	-15.14	-86.27	-16.08	-0.67	-40.06	-7.67	-25.39
RC2-RC3							
Diff.	-3.81	-1.00	-0.35	-0.18	-0.29	-0.53	0.12

[a]VTZ: cc-pVTZ, aVDZ: aug-cc-pVDZ, aVTZ: aug-cc-pVTZ, aVQZ: aug-cc-pVQZ, aCVTZ: aug-cc-pCVTZ.

RC0 approach are 88.55, 17.59, and 1.91 kcal mol^{-1}, which were reduced to 3.29, 1.86, and 1.42 kcal mol^{-1} when using the RC2 scheme and to 2.28, 1.52, and 1.24 kcal mol^{-1} when using the RC3 scheme. The lowest MAD of the method/basis set combinations when using the RC2 approach is CCSD(T)/cc-pVTZ (MAD = 1.06 kcal mol^{-1}), followed by MP2/cc-pVTZ rather than MP2/aug-cc-pVQZ which is superior when using RC0. The RC3 approach allows for balancing more errors of the reaction scheme than RC2 does, resulting in higher cancellation of errors associated with the differential correlation effect. Thus, B3LYP/cc-pVTZ has the lowest MAD of 0.72 kcal mol^{-1} among all method/basis set combinations when using the RC3 approach, as shown in Table 4.10, followed by CCSD(T)/cc-pVTZ with a MAD of 0.76 kcal mol^{-1} and MP2/cc-pVTZ with a MAD of 1.06 kcal mol^{-1}.

Method choice seems to be more important than basis set size when using RC2 and RC3 reaction schemes compared to RC0. These findings agree with results reported by Jorgensen.[40] The MSD values show a tendency for underestimation of the $\Delta H°_{f,298}'s$ by all the single point energy calculations, except for the CCSD(T) and B3LYP methods, when using the RC2 and the RC3 schemes, as shown in Table 4.10 and 4.11, instead of overestimation as it is using the RC0 scheme. The B3LYP/cc-pVTZ level of theory exhibits an overestimation in the calculated $\Delta H°_{f,298}'s$, on average, when using any of the utilized thermochemical approaches, while CCSD(T) overestimates the $\Delta H°_{f,298}'s$ calculated using the RC0 and RC2 approaches but underestimate those calculated using the RC3 scheme, as shown in Table 4.12.

4.4 Conclusion

The thermochemical isodesmic (RC2) and hypohomodesmotic (RC3) reaction schemes for hydrocarbon have been extended to include organoselenium compounds. The $\Delta H°_{f,298}'s$ of

organoselenium species, including R_2Se, where R is CH_3-, C_2H_5-, C_3H_7-, C_4H_9-, iC_3H_7-, and CH_2=CH-, and $(CH_3CH_2)_2Se_2$, were predicted using the atomization approach (RC0) and the isodesmic (RC2) and hypohomodesmotic (RC3) reaction schemes via several composite methods, such as ccCA, G3 and G4, and the B3PW91 density functional. The quality of these approaches has also been investigated. In addition, an assessment of the impact of RC0, RC2, and RC3 on the single point energy calculations utilized within the ccCA has been examined.

The most important finding here is that while the RC2 and RC3 schemes allow for cancellation of errors from differential correlation and size extensivity, the RC0 scheme via ccCA-P (MAD=1.68 kcal mol^{-1}), ccCA-S4 (MAD=1.70 kcal mol^{-1}), and G3 (MAD=1.74 kcal mol^{-1}) is still an effective and simple approach for predicting $\Delta H°_{f,298}{}'s$ of organoselenium compounds that are within the experimental uncertainties (σ=1.53 kcal mol^{-1}, on average). The reduction in the MADs of the calculated $\Delta H°_{f,298}{}'s$ using RC2 and RC3 was profound with the ccCA-S3 method in which the MAD was reduced by -2.18 (RC2) and -1.87 (RC3) kcal mol^{-1} compared to RC0. Employing the RC2 and RC3 schemes, the MADs of all four ccCA variants become nearly the same with ranges of 0.92 - 0.94 (RC2) and 1.22 - 1.26 (RC3) kcal mol^{-1}, showing less dependency on the extrapolation schemes. Thus, for high accuracy the use of the RC2 reaction scheme with ccCA is recommended since is resulted in the reduction of the maximum deviation of the $\Delta H°_{f,298}{}'s$ of the target organoselenium molecules with respect to experiment.

Trivial change in the MADs of the $\Delta H°_{f,298}{}'s$ calculated using the RC2 and RC3 schemes with the G3 method were observed compared to RC0 (from 1.74 to 1.58 (RC2) and to 1.79 (RC3) kcal mol^{-1}), so G3 seems to be unbiased to any thermochemical schemes. The inclusion of empirical parameters within G*n* theory may be a reason for the low impact of these

thermochemical schemes on the G3 method. On the other hand, the G4 method results in a systematic reduction in the MAD from 2.85 (RC0) to 1.47 (RC2) to 1.29 (RC3) kcal mol^{-1}, while B3PW91 only predicts accurate $\Delta H°_{f,298}{}'s$ when used with the RC3 scheme.

The most significant reduction in MADs, as shown in Figure 4.4, is found when using RC2 and RC3 via the method/basis set combinations involved within the ccCA methodology, compared to RC0, emphasizing the importance of the use of these error balanced reaction schemes (RC2 and RC3) with single point energy calculations. The MAD of the $\Delta H°'_{f,298}s$ of organoselenium species calculated by the methods within ccCA is reduced by 0.49 - 85.26 kcal mol^{-1} when using RC2 and by 0.67 - 86.27 kcal mol^{-1} when using RC3, in comparison to RC0.

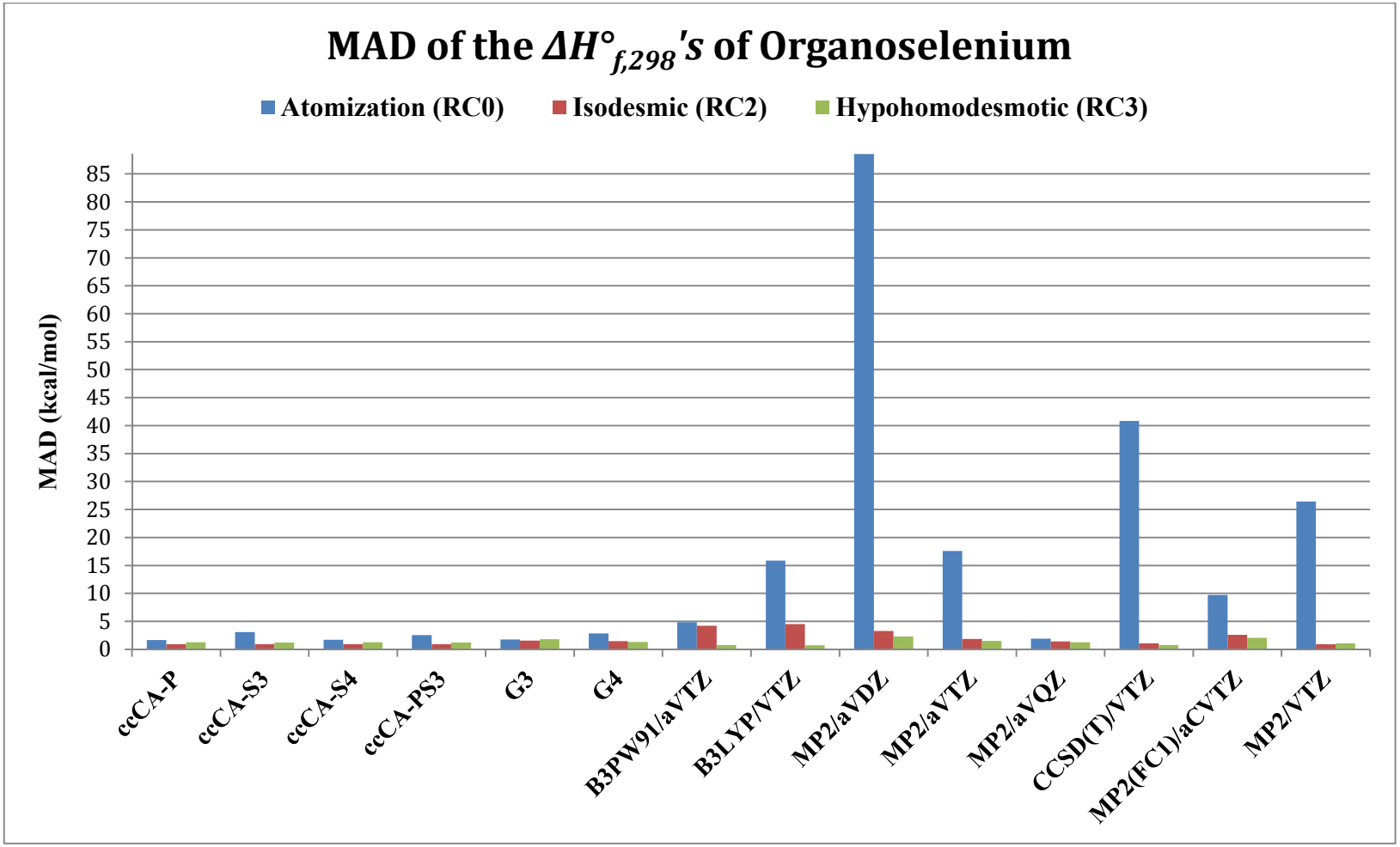

Figure 4.4 The mean absolute deviations (MADs) of the calculated enthalpies of formation using three thermochemical schemes, RC0, RC2, RC3, with composite methods and single point energy calculations utilized within ccCA methodology.

APPENDIX

APPENDIX

Figure 4.4 The optimized structures for organoselenium molecules at the B3LYP/cc-pVTZ level of theory. a. Dimethyl selenide. b. Dimethyl diselenide. c. Divinyl selenide. d. Diethyl selenide. e. Diethyl diselenide. f. Diisopropyl selenide. g. Dipropyl selenide. h. Dibutyl selenide

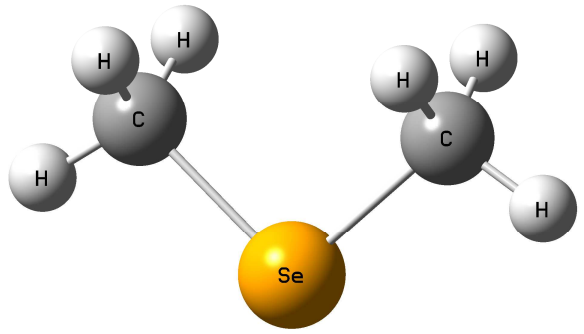

a. Dimethyl selenide

C,0.,1.4745463319,-0.5250668407
C,0.,-1.4745463319,-0.5250668407
H,0.,2.3979939937,0.0487822942
H,0.,-2.3979939937,0.0487822942
H,0.89334582,1.4319630523,-1.1430822182
H,-0.89334582,1.4319630523,-1.1430822182
H,-0.89334582,-1.4319630523,-1.1430822182
H,0.89334582,-1.4319630523,-1.1430822182
Se,0.,0.,0.7732299539

b. Dimethyl diselenide

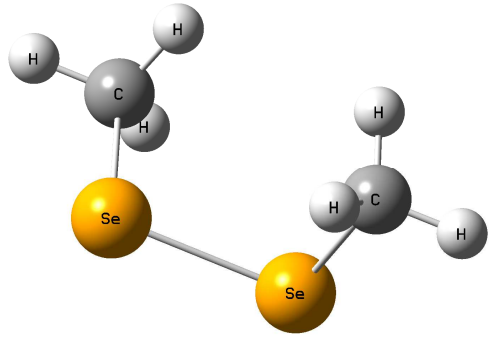

C,-3.8566963534,0.4978802241,-0.1487157894
H,-2.9959769279,0.0321646867,0.3204593568
H,-3.5836945322,0.8699953899,-1.1352109631
H,-4.6807464241,-0.2032193801,-0.2310914273
C,-3.4519132533,1.0664446232,3.9259947929
H,-3.0519066265,2.0717550224,4.0080350634
H,-3.7179227193,0.6893268138,4.9125006592
H,-2.7344865202,0.3999894362,3.4580303513
Se,-4.431262183,2.0818797179,0.8836362695
Se,-5.1354589001,1.102407286,2.8919271468

c. Divinyl selenide

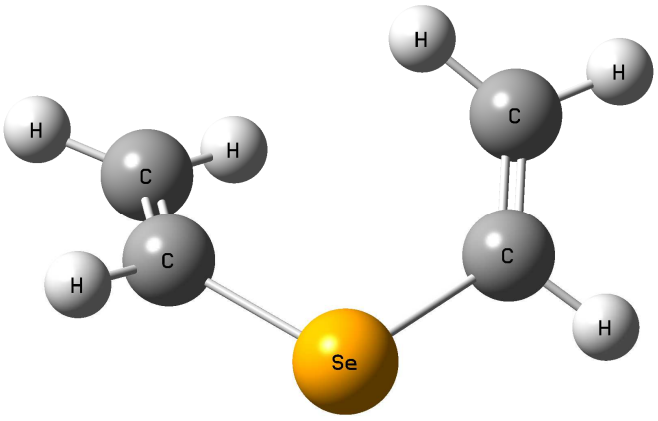

C,-1.6717478143,-1.1551364351,0.2263623732
C,-1.5145170703,0.0995145459,-0.1729240918
C,1.5145171709,0.0995150317,0.172924123
C,1.6717483174,-1.1551358988,-0.226362342
H,-2.6216442804,-1.651758326,0.0748045573
H,-0.8927855835,-1.7221448581,0.7137937834
H,-2.3281680491,0.6370998822,-0.6445860837
H,2.3281679773,0.6371006291,0.644586115
H,2.6216449427,-1.6517574851,-0.0748045261
H,0.8927862684,-1.7221445717,-0.7137937521
Se,-0.0000001354,1.2572272992,0.0000000156

d. Diethyl selenide

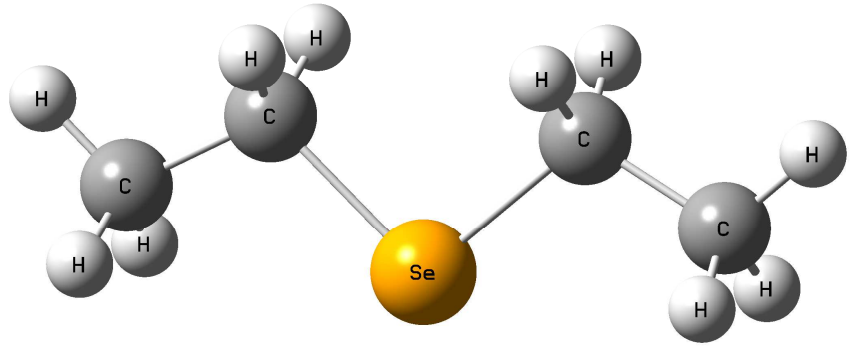

C,0.,1.4876577251,-0.6049163648
C,0.,-1.4876577251,-0.6049163648
C,0.,2.8300871235,0.1113327778
C,0.,-2.8300871235,0.1113327778
H,0.8844003853,1.3753237887,-1.2299306436
H,-0.8844003853,1.3753237887,-1.2299306436
H,0.8844003853,-1.3753237887,-1.2299306436
H,-0.8844003853,-1.3753237887,-1.2299306436
H,0.,3.6455581618,-0.6146868743
H,0.,-3.6455581618,-0.6146868743
H,-0.8822256968,2.9446536553,0.7418417228
H,0.8822256968,2.9446536553,0.7418417228
H,0.8822256968,-2.9446536553,0.7418417228
H,-0.8822256968,-2.9446536553,0.7418417228
Se,0.,0.,0.7009286041

e. Diethyl diselenide

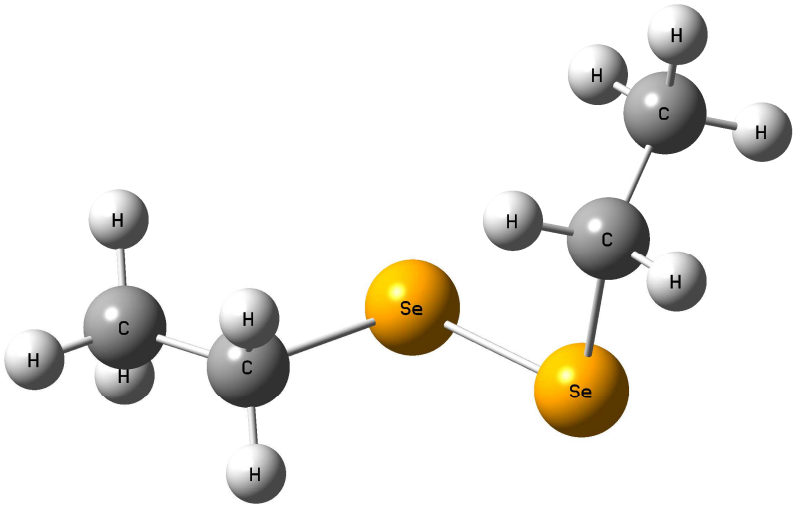

C,-4.0040189665,0.6658354249,-0.2441569024
H,-4.54670732,-0.2719925307,-0.3255037137
H,-4.5834799815,1.3604152158,0.3584609682
C,-3.4105090249,0.8934826096,3.8815204752
H,-4.104934018,1.5576767945,3.3723835302
H,-3.9253549137,0.4675928726,4.7443516987
Se,-2.316788856,0.2763347679,0.7450209433
Se,-3.1438763359,-0.6945844731,2.7097772517
C,-2.128540207,1.6009534242,4.2796156284
H,-1.6020397625,1.9756550928,3.401878767
H,-2.3521537203,2.4540544872,4.925544467
H,-1.4577404208,0.9321636944,4.8184878256
C,-3.6682143629,1.2494055333,-1.6084883837
H,-4.5865424401,1.4656150546,-2.1583944699
H,-3.1074805542,2.1807438566,-1.5202773605
H,-3.0783422958,0.5545095955,-2.2071552451

f. Diisopropyl selenide

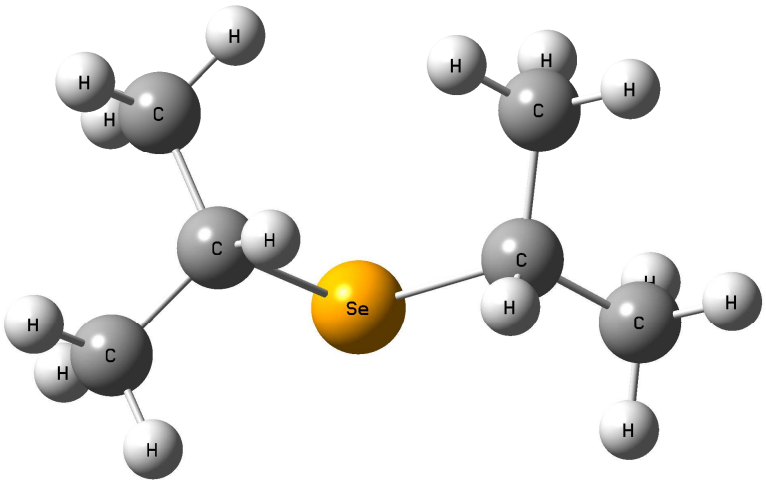

C,-0.0371068084,0.7260443361,-0.353968696
C,-1.0957241316,1.5967108623,0.3162987173
C,0.6902258789,-2.2470260565,-0.0867633906
H,-0.6902099186,2.5914756984,0.520535074
C,0.516936112,1.3710247215,-1.6201723962
H,0.9022900234,-1.9088823757,0.9278090291
H,-0.2746516616,1.5278835321,-2.3544088705
H,0.9551130577,2.3462888581,-1.386857929
H,1.2844510936,0.7572198116,-2.0882055811
H,-1.9668916712,1.7251414201,-0.3291530458
H,-1.4359482579,1.1631920134,1.2551462037
Se,-0.8105309195,-1.0859098533,-0.7140577528
C,1.9395793274,-2.1205034957,-0.9476863285
H,2.3298073342,-1.1035174715,-0.9563295404
H,2.7282478688,-2.7726868757,-0.5599633827
H,1.733559985,-2.4119594024,-1.9783350419
C,0.16310624,-3.6772808639,-0.0415738526
H,0.9409498616,-4.3493820403,0.328914838
H,-0.7032312878,-3.7672165665,0.6129666916
H,-0.1244239334,-4.0224540828,-1.03650531
H,0.7721469473,0.5345294808,0.3509850545

g. Dipropyl selenide

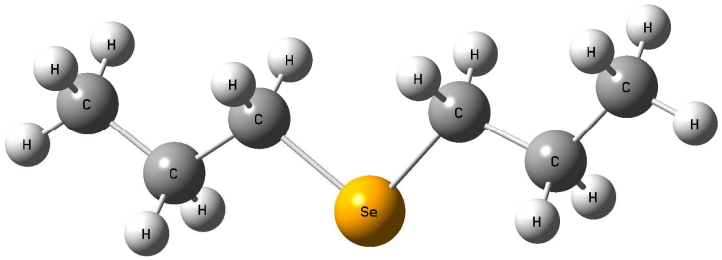

C,0.0000002585,1.4871445752,-0.7438891543
C,0.0000013975,-1.4871445747,-0.7438891556
H,0.8848261799,1.3772131001,-1.3704231853
H,-0.8848221014,1.3772124784,-1.3704281054
H,-0.8848210448,-1.377213153,-1.3704281086
H,0.8848272366,-1.3772124233,-1.3704231839
Se,-0.0000028472,0.0000000003,0.5621833724
C,-0.0000000222,-2.8354653726,-0.0335738398
H,-0.87509911,-2.9032470007,0.6170149326
H,0.8750954883,-2.9032462741,0.6170198199
C,0.0000032096,-4.0079414416,-1.0163934274
H,0.0000021249,-4.9618587066,-0.4873466401
H,-0.8814991074,-3.9850481132,-1.6600097778
H,0.881509101,-3.9850473815,-1.6600048562
C,-0.0000021874,2.8354653738,-0.0335738392
H,-0.8751013217,2.9032463328,0.6170149407
H,0.8750932767,2.9032469455,0.6170198128
C,0.0000001377,4.0079414418,-1.0163934279
H,-0.0000016676,4.9618587073,-0.4873466416
H,0.8815060387,3.9850480535,-1.6600048673
H,-0.8815021697,3.9850474403,-1.6600097678

h. Dibutyl selenide

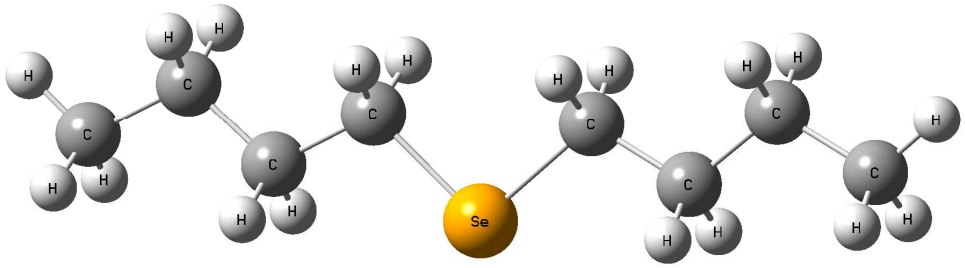

C,-0.0000050541,1.4878682362,-0.7091398258
C,0.0000006042,-1.4878682366,-0.709139827
H,0.8848032967,1.3771797052,-1.3353544409
H,-0.8848059758,1.3771759473,-1.3353642749
H,-0.8848009689,-1.3771795899,-1.3353639854
H,0.8848083037,-1.3771760642,-1.3353547333
Se,-0.0000091736,-0.0000000002,0.596483834
C,-0.0000004214,-2.8349424563,0.0026831003
H,-0.8755992344,-2.9038466045,0.6542320099
H,0.8755919125,-2.9038431637,0.6542410734
C,0.0000069351,-4.0171651407,-0.9714082227
H,-0.8746248568,-3.9464770193,-1.624653031
H,0.8746451908,-3.946473573,-1.6246440039
C,-0.0000118779,2.8349424561,0.002683101
H,-0.8756112253,2.9038430175,0.6542316683
H,0.8755799216,2.9038467506,0.6542414164
C,-0.0000089751,4.0171651402,-0.9714082224
H,0.8746298497,3.9464771785,-1.6246436301
H,-0.8746401979,3.9464734124,-1.624653404
C,0.0000059521,-5.3715354958,-0.2640161782
H,-0.8808554474,-5.4849631396,0.3710055057
H,0.0000112789,-6.1937362553,-0.9808245605
H,0.8808612345,-5.4849596601,0.3710146126
C,-0.0000158487,5.3715354956,-0.2640161784
H,-0.0000136073,6.1937362548,-0.9808245609
H,-0.8808779874,5.4849595026,0.3710051296
H,0.8808386945,5.484963297,0.3710149883

REFERENCES

REFERENCES

(1) Back, T. G. *Organoselenium Chemistry : A Practical Approach*, 1st ed.; Oxford University Press.: Oxford, U.K., 1999.

(2) Wirth, T. *Organoselenium Chemistry : Modern Developments in Organic Synthesis*, 1st ed.; Springer-Verlag Berlin Heidelberg: Berlin,Germany, 2000.

(3) Freudendahl, D. M.; Santoro, S.; Shahzad, S. A.; Santi, C.; Wirth, T. Green Chemistry with Selenium Reagents: Development of Efficient Catalytic Reactions. *Angew. Chemie Int. Ed.* **2009**, *48* (45), 8409–8411.

(4) Sancineto, L.; Tidei, C.; Bagnoli, L.; Marini, F.; Lenardão, E. J.; Santi, C. Selenium Catalyzed Oxidation of Aldehydes: Green Synthesis of Carboxylic Acids and Esters. *Molecules* **2015**, *20* (6), 10496–10510.

(5) Nogueira, C. W.; Zeni, G.; Rocha, J. B. T. Organoselenium and Organotellurium Compounds: Toxicology and Pharmacology. *Chem. Rev.* **2004**, *104* (12), 6255–6285.

(6) Hondal, R. J.; Ruggles, E. L. Differing Views of the Role of Selenium in Thioredoxin Reductase. *Amino Acids*, 2011, *41*, 73–89.

(7) Roman, M.; Jitaru, P.; Barbante, C. Selenium Biochemistry and Its Role for Human Health. *Metallomics* **2014**, *6* (1), 25–54.

(8) Tiekink, E. R. T. Therapeutic Potential of Selenium and Tellurium Compounds: Opportunities yet Unrealised. *Dalt. Trans.* **2012**, *41* (21), 6390–6395.

(9) Młochowski, J.; Brząszcz, M.; Giurg, M.; Palus, J.; Wójtowicz, H. Selenium-Promoted Oxidation of Organic Compounds: Reactions and Mechanisms. *European J. Org. Chem.* **2003**, *2003* (22), 4329–4339.

(10) Młochowski, J.; Wójtowicz-Młochowska, H. Developments in Synthetic Application of selenium(IV) Oxide and Organoselenium Compounds as Oxygen Donors and Oxygen-Transfer Agents. *Molecules* **2015**, *20*, 10205–10243.

(11) Jones, A. C.; O'Brien, P. *CVD of Compound Semicondcutors: Precursor Synthesis, Development and Applications*; Wiley-VCH: Weinheim, Germany, 1997.

(12) Kolodziejski, L. A.; Gunshor, R. L.; Nurmikko, A. V. Wide-Bandgap II-VI

Heterostructures for Blue/Green Optical Sources: Key Materials Issues. *Annu. Rev. Mater. Sci.* **1995**, *25* (1), 711–755.

(13) Mitsuhashi, H.; Mitsuishi, I.; Mizuta, M.; Kukimoto, H. Coherent Growth of ZnSe on GaAs by MOCVD. *Jpn. J. Appl. Phys.* **1985**, *24* (Part 2, No. 8), L578–L580.

(14) Giapis, K. P.; Jensen, K. F. Effect of Operating Conditions and Precursors on Optoelectronic Properties of OMVPE Grown ZnSe. *J. Cryst. Growth* **1990**, *101* (1–4), 111–117.

(15) Bourret, E. D.; Zach, F. X.; Yu, K. M.; Walker, J. M. Growth and Characterization of ZnSe Grown by Organometallic Vapor Phase Epitaxy Using Diisopropyl Selenide and Diethyl Zinc. *J. Cryst. Growth* **1995**, *147* (1–2), 47–54.

(16) Huguet, J. L. Oxidation of Olefins Catalyzed by Selenium. In *Oxidation of Organic Compounds*; Mayo, F. R., Ed.; American Chemical Society, 1968; Vol. 76, pp 345–351.

(17) Sharpless, K. B.; Lauer, R. F. Mild Procedure for the Conversion of Epoxides to Allylic Alcohols. First Organoselenium Reagent. *J. Am. Chem. Soc.* **1973**, *95* (8), 2697–2699.

(18) Sharpless, K. B.; Lauer, R. F.; Teranishi, A. Y. Electrophilic and Nucleophilic Organoselenium Reagents. New Routes to α,β-Unsaturated Carbonyl Compounds. *J. Am. Chem. Soc.* **1973**, *95* (18), 6137–6139.

(19) Wallschläger, D.; Feldmann, J. Formation, Occurrence, Significance, and Analysis of Organoselenium and Organotellurium Compounds in the Environment. In *Organometallics in Environment and Toxicology: Metal ions in life sciences*; Royal Society of Chemistry: Cambridge, 2010; Vol. 7, pp 319–364.

(20) Santi, C. *Organoselenium Chemistry : Between Synthesis and Biochemistry: EBSCOhost*; Santi, C., Ed.; Sharjah : Bentham Science Publishers, 2014.

(21) Liebman, J. F.; Slayden, S. W. Thermochemistry of Organoselenium and Organotellurium Compounds. In *PATAI'S Chemistry of Functional Groups*; John Wiley & Sons, Ltd.: Chichester, UK, 2011; pp 1–25.

(22) Voronkov, M. G.; Klyuchnikov, V. A.; Kolabin, S. N.; Shvets, G. N.; Varushin, P. I.; Deryagina, E. N.; Korchevin, N. A.; Tsvetnitskaya, S. I. Thermochemical Properties of Diorganylchalcogenides and -Dichalcogenides RMnR (M=S, Se, Te; n=1, 2). *Dokl. Akad. Nauk SSSR* **1989**, *307* (5), 1139–1144.

(23) Tel'noy, V. I.; Sheiman, M. S. Thermodynamics of Organoselenium and Organotellurium Compounds. *Russ. Chem. Rev.* **1995**, *64* (4), 309–316.

(24) Batt, L. Thermochemistry of Selenium and Tellurium Compounds. In *Organic Selenium and Tellurium Compounds*; John Wiley & Sons, Inc.: Chichester, UK,1986; pp 157–160.

(25) Pearson, J. K.; Ban, F.; Boyd, R. J. An Evaluation of Various Computational Methods for the Treatment of Organoselenium Compounds. *J. Phys. Chem. A* **2005**, *109* (45), 10373–10379.

(26) Heverly-Coulson, G. S.; Boyd, R. J. Systematic Study of the Performance of Density Functional Theory Methods for Prediction of Energies and Geometries of Organoselenium Compounds. *J. Phys. Chem. A* **2011**, *115* (18), 4827–4831.

(27) Maung, N.; Williams, J.; Wright, A. The Evaluation of Bond Dissociation Energies for Simple Selenium-Containing Molecules Using Ab Initio and Density Functional Methods. *J. Mol. Struct. THEOCHEM* **1998**, *453* (1–3), 181–189.

(28) Pearson, J. K.; Boyd, R. J. Quantum Mechanical Approaches to Selenium Biochemistry. In *Quantum Biochemistry*; Wiley-VCH Verlag GmbH & Co. KGaA: Weinheim, Germany, 2010; pp 585–603.

(29) Deakyne, C. A.; Ludden, A. K.; Roux, M. V.; Notario, R.; Demchenko, A. V.; Chickos, J. S.; Liebman, J. F. Energetics of the Lighter Chalcogen Analogues of Carboxylic Acid Esters †. *J. Phys. Chem. B* **2010**, *114* (49), 16253–16262.

(30) Zaccaria, F.; Wolters, L. P.; Fonseca Guerra, C.; Orian, L. Insights on Selenium and Tellurium Diaryldichalcogenides: A Benchmark DFT Study. *J. Comput. Chem.* **2016**, *37* (18), 1672–1680.

(31) Pople, J. A.; Head□Gordon, M.; Fox, D. J.; Raghavachari, K.; Curtiss, L. A. Gaussian□1 Theory: A General Procedure for Prediction of Molecular Energies. *J. Chem. Phys.* **1989**, *90* (10), 5622–5629.

(32) Curtiss, L. A.; Raghavachari, K.; Trucks, G. W.; Pople, J. A. Gaussian□2 Theory for Molecular Energies of First□ and Second□row Compounds. *J. Chem. Phys.* **1991**, *94* (11), 7221–7230.

(33) Curtiss, L. A.; Raghavachari, K.; Redfern, P. C.; Rassolov, V.; Pople, J. A. Gaussian-3 (G3) Theory for Molecules Containing First and Second-Row Atoms. *J. Chem. Phys.* **1998**, *109* (18), 7764–7776.

(34) Curtiss, L. A.; Redfern, P. C.; Raghavachari, K. Gaussian-4 Theory. *J. Chem. Phys.* **2007**, *126*, 084108–084112.

(35) DeYonker, N. J.; Cundari, T. R.; Wilson, A. K. The Correlation Consistent Composite Approach (ccCA): An Alternative to the Gaussian-N Methods. *J. Chem. Phys.* **2006**, *124*.

(36) DeYonker, N. J.; Grimes, T.; Yockel, S.; Dinescu, A.; Mintz, B.; Cundari, T. R.; Wilson, A. K. The Correlation-Consistent Composite Approach: Application to the G3/99 Test Set. *J. Chem. Phys.* **2006**, *125*, 104111–104115.

(37) DeYonker, N. J.; Mintz, B.; Cundari, T. R.; Wilson, A. K. Application of the Correlation Consistent Composite Approach (ccCA) to Third-Row (Ga−Kr) Molecules. *J. Chem. Theory Comput.* **2008**, *4* (2), 328–334.

(38) DeYonker, N. J.; Wilson, B. R.; Pierpont, A. W.; Cundari, T. R.; Wilson, A. K. Towards the Intrinsic Error of the Correlation Consistent Composite Approach (ccCA). *Mol. Phys.* **2009**, *107* (8–12), 1107–1121.

(39) DeYonker, N. J.; Ho, D. S.; Wilson, A. K.; Cundari, T. R. Computational S-Block Thermochemistry with the Correlation Consistent Composite Approach. *J. Phys. Chem. A* **2007**, *111* (42), 10776–10780.

(40) Jorgensen, K. R.; Wilson, A. K. Enthalpies of Formation for Organosulfur Compounds: Atomization Energy and Hypohomodesmotic Reaction Schemes via Ab Initio Composite Methods. *Comput. Theor. Chem.* **2012**, *991*, 1–12.

(41) Wilson, B. R.; DeYonker, N. J.; Wilson, A. K. Prediction of Hydrocarbon Enthalpies of Formation by Various Thermochemical Schemes. *J. Comput. Chem.* **2012**, *33* (25), 2032–2042.

(42) Curtiss, L. A.; Redfern, P. C.; Raghavachari, K. Gn Theory. *Wiley Interdiscip. Rev. Comput. Mol. Sci.* **2011**, *1*, 810–825.

(43) Blaudeau, J.-P.; McGrath, M. P. Extension of Gaussian-2 (G2) Theory to Molecules Containing Third-Row Atoms K and Ca. *J. Chem. Phys.* **1997**, *107* (13), 5016–5021.

(44) Curtiss, L. A.; Redfern, P. C.; Rassolov, V.; Kedziora, G.; Pople, J. A. Extension of Gaussian-3 Theory to Molecules Containing Third-Row Atoms K, Ca, Ga-Kr. *J. Chem. Phys.* **2001**, *114* (21), 9287–9295.

(45) Curtiss, L. A.; Redfern, P. C.; Raghavachari, K. Assessment of Gaussian-3 and Density-Functional Theories on the G3/05 Test Set of Experimental Energies. *J. Chem. Phys.* **2005**, *123*, 124107–124112.

(46) Mayer, P. M.; Gal, J. F.; Radom, L. The Heats of Formation, Gas-Phase Acidities, and Related Thermochemical Properties of the Third-Row Hydrides GeH_4, AsH_3, SeH_2 and

HBr from G2 Ab Initio Calculations. *Int. J. Mass Spectrom.* **1997**, *167*, 689–696.

(47) Peterson, C.; Penchoff, D. A.; Wilson, A. K. Prediction of Thermochemical Properties Across the Periodic Table: A Review of the Correlation Consistent Composite Approach (ccCA) Strategies and Applications. *Annu. Rep. Comput. Chem.* **2016**, *12*.

(48) Blaudeau, J.-P.; Curtiss, L. A. Optimized Gaussian Basis Sets for Use with Relativistic Effective(Core) Potentials: K, Ca, Ga-Kr. *Int. J. Quantum Chem.* **1997**, *61* (6), 943–952.

(49) Jankowski, K.; Polasik, M. Differential Correlation Effects for States of the $3d^n$ and $3d^n$ $4s^m$ Configurations. I. The Copper and Zinc Atoms and Their Ions. *J. Phys. B At. Mol. Phys.* **1985**, *18* (11), 2133–2146.

(50) Lee, E. P. F.; Wright, T. G. Methylcarbyne Radical [$CH_3C(\tilde{X}^2A''$; $\tilde{a}^4A_2$)] and the Chemiionization Reaction: $CH_3C + O \rightarrow CH_3CO^+ + E$-. *J. Phys. Chem. A* **1999**, *103* (6), 721–726.

(51) Decker, B. K.; Adams, N. G.; Babcock, L. M.; Crawford, T. D.; Schaefer, H. F. Thermokinetic Proton Transfer and Ab Initio Studies of the $[2H,S,O]^+$ System. The Proton Affinity of HSO. *J. Phys. Chem. A* **2000**, *104* (19), 4636–4647.

(52) Harding, M. E.; Vázquez, J.; Ruscic, B.; Wilson, A. K.; Gauss, J.; Stanton, J. F. High-Accuracy Extrapolated Ab Initio Thermochemistry. III. Additional Improvements and Overview. *J. Chem. Phys.* **2008**, *128* (11), 11411-114115.

(53) Nicolaides, A. An Evaluation of the Performance of G2, G2(MP2) and G2(MP2,SVP) Theories for Heats of Formation and Heats of Reaction in the Case of "Large" Hydrocarbons. *Mol. Phys.* **1996**, *88*, 759–766.

(54) Hehre, W. J.; Random, L.; Schleyer, P. V. R.; Pople, J. A. *Ab Initio Molecular Orbital Theory*, 1st ed.; John Wiley & Sons, Inc.: New York, US, 1986.

(55) Hehre, W. J.; Ditchfield, R.; Radom, L.; Pople, J. A. Molecular Orbital Theory of the Electronic Structure of Organic Compounds. V. Molecular Theory of Bond Separation. *J. Am. Chem. Soc.* **1970**, *92* (16), 4796–4801.

(56) Császár, A. G.; Allen, W. D.; Schaefer, H. F. In Pursuit of the Ab Initio Limit for Conformational Energy Prototypes. *J. Chem. Phys.* **1998**, *108* (23), 9751–9764.

(57) Wheeler, S. E.; Houk, K. N.; Schleyer, P. v. R.; Allen, W. D. A Hierarchy of Homodesmotic Reactions for Thermochemistry. *J. Am. Chem. Soc.* **2009**, *131* (7), 2547–2560.

(58) Wheeler, S. E. Homodesmotic Reactions for Thermochemistry. *Wiley Interdiscip. Rev. Comput. Mol. Sci.* **2012**, *2* (2), 204–220.

(59) Engelkemier, J.; Windus, T. L. Quantum Mechanical Modeling of Sugar Thermochemistry. In *Computational Modeling in Lignnocellulosic biofuel production*; American Chemical Scociey, 2010; pp 179–199.

(60) Frisch, M. J.; Trucks, G. W.; Schlegel, H. B.; Scuseria, G. E.; Robb, M. A.; Cheeseman, J. R.; Scalmani, G.; Barone, V.; Mennucci, B.; Petersson, G. A.; et al. Gaussian 09, 2009.

(61) Jorgensen, K. R.; Oyedepo, G. A.; Wilson, A. K. Highly Energetic Nitrogen Species: Reliable Energetics via the Correlation Consistent Composite Approach (ccCA). *J. Hazard. Mater.* **2011**, *186* (1), 583–589.

(62) Alsunaidi, Z. H. A.; Wilson, A. K. DFT and Ab Initio Composite Methods: Investigation of Oxygen Fluoride Species. *Comput. Theor. Chem.* **2016**, *1095*, 71–82.

(63) Gavin Williams, T.; Wilson, A. K. Performance of the Correlation-Consistent Composite Approach for Sulfur Species. *J. Sulfur Chem.* **2008**, *29* (3–4), 353–365.

(64) Becke, A. D. A New Mixing of Hartree–Fock and Local Density□functional Theories. *J. Chem. Phys.* **1993**, *98* (2), 1372–1377.

(65) Perdew, J. P.; Wang, Y. Accurate and Simple Analytic Representation of the Electron-Gas Correlation Energy. *Phys. Rev. B* **1992**, *45* (23), 13244–13249.

(66) Gibson, S. T.; Greene, J. P.; Berkowitz, J. A Photoionization Study of SeH and H_2Se. *J. Chem. Phys.* **1986**, *85* (9), 4815–4824.

(67) Jackson, V. E.; Dixon, D. A.; Christe, K. O. Thermochemical Properties of Selenium Fluorides, Oxides, and Oxofluorides. *Inorg. Chem.* **2012**, *51* (4), 2472–2485.

(68) Tasi, G.; Izsák, R.; Matisz, G.; Császár, A. G.; Kállay, M.; Ruscic, B.; Stanton, J. F. The Origin of Systematic Error in the Standard Enthalpies of Formation of Hydrocarbons Computed via Atomization Schemes. *ChemPhysChem* **2006**, *7* (8), 1664–1667.

(69) Cox, J. D.; Wagman, D. D.; Medvedev, V. A. *CODATA: Key Values for Thermodynamics*; Hemisphere Pub. Corp.: New York, U.S., 1989.

(70) Katritzky, A. R.; Chen, K.; Maran, U.; Carlson, D. A. QSPR Correlation and Predictions of GC Retention Indexes for Methyl- Branched Hydrocarbons Produced by Insects. *Anal. Chem.* **2000**, *72* (1), 101–109.

(71) Katritzky, A. R.; Dobchev, D. A.; Karelson, M. Physical, Chemical, and Technological Property Correlation with Chemical Structure: The Potential of QSPR. *Z. Naturforsch. Sect. B J. Chem. Sci.* **2006**, *61* (4), 373–384.

(72) Katritzky, A. R.; Kuanar, M.; Slavov, S.; Hall, C. D.; Karelson, M.; Kahn, I.; Dobchev, D. A. Quantitative Correlation of Physical and Chemical Properties with Chemical Structure: Utility for Prediction. *Chem. Rev.* **2010**, *110* (10), 5714–5789.

(73) Katritzky, A. R.; Petrukhin, R.; Tatham, D.; Basak, S.; Benfenati, E.; Karelson, M.; Maran, U. Interpretation of Quantitative Structure-Property and-Activity Relationships. *J. Chem. Inf. Comput. Sci.* **2001**, *41* (3), 679–685.

(74) Jover, J.; Bosque, R.; Martinho Simões, J. A.; Sales, J. Estimation of Enthalpies of Formation of Organometallic Compounds from Their Molecular Structures. *J. Organomet. Chem.* **2008**, *693* (7), 1261–1268.

(75) Rossini, F. D. Symposium on Fundamental Chemical Thermodynamics of Hydrocarbons and Their Derivatives: Heat of Formation of Gaseous Hydrocarbons. *Chem. Rev.* **1940**, *27* (1), 1–16.

(76) Prosen, E. J.; Rossini, F. D. Heats of Combustion and Formation of the Paraffin Hydrocarbons at 25 C. *J. Res. NBS* **1945**, *34*, 263–269.

(77) Prosen, E. J.; Johnson, W. H.; Rossini, F. D. Heat of Formation and Combustion of the Normal Alkylcyclopentanes and Cyclohexanes and the Increment per CH_2 Group for Several Homologous Series of Hydrocarbons. *J. Res. NBS* **1946**, *37*, 51–56.

(78) Kistiakowsky, G. B.; Ruhoff, J. R.; Smith, H. A.; Vaughan, W. E.; Smith, A.; Vaughan, W. E. Heats of Organic Reactions. IV. Hydrogenation of Some Dienes and of Benzene. *J. Am. Chem. Soc.* **1936**, *58* (1), 146–153.

(79) Mills, K. C. *Thermodynamic Data for Inorganic Sulphides, Selenides and Tellurides*; Butterworths: London, U.K., 1974.

(80) Cioslowski, J.; Schimeczek, M.; Liu, G.; Stoyanov, V. A Set of Standard Enthalpies of Formation for Benchmarking, Calibration, and Parametrization of Electronic Structure Methods. *J. Chem. Phys.* **2000**, *113* (21), 9377–9389.

(81) Schwartz, C. Importance of Angular Correlations between Atomic Electrons. *Phys. Rev.* **1962**, *126* (3), 1015–1019.

CHAPTER 5 TOWARDS A MORE RATIONAL DESIGN OF THE DIRECT SYNTHESIS OF ANILINE: A DFT STUDY

5.1 Introduction

Green chemical synthesis has been of significant interest for the development of safe and efficient reaction processes that reduce the generation of hazardous products and for economic benefits in the chemical industry. One process that has widely attracted the attention is the direct synthesis of aniline. Aniline ($C_6H_5NH_2$) is an important building block in the chemical industry as it can undergo numerous reactions either involving the amino group or the aromatic ring. These reactions can be extended for various industrial applications including the production of dyes, the production of polyurethane, use in the rubber industry, and in the manufacturing of pharmaceuticals, to name a few.[1,2] In 2013, global annual production of aniline was ~5 million tons and was anticipated to reach 6.2 million tons by 2015.[2] 80% of aniline goes to the production of methylene diphenylene isocyanate, which is used in polyurethane manufacture.[1] The mass production of aniline demands an efficient, safe, and economical synthesis. While the first reported production of aniline was in 1854 via the reduction of nitrobenzene, little improvements in this process have been reported, and hence nitrobenzene remains the raw material used by almost all commercial producers of aniline.[1] Scheme 5.1 summarizes the industrial synthesis of aniline, which is comprised of multiple steps. It begins with the nitration of benzene using a mixture of nitric acid and sulfuric acid. The next step is the hydrogenation (reduction) of the nitro group in the presence of a catalyst (Pt/Pd on carbon or Raney-Ni). Lastly, separation and distillation are performed to purify aniline.[1]

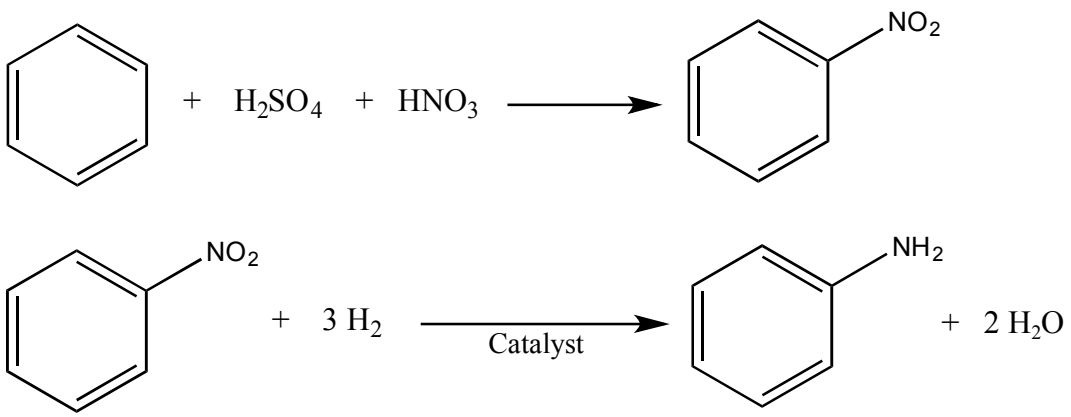

Scheme 5.1 Synthesis of aniline. Adapted from Reference 1.

The conventional route of the production of aniline, although it is practical and very exothermic, has drawbacks. It is not economical with respect to the capital cost and to atom economy. It also consumes a lot of energy, requires large amounts of corrosive acid catalysts and produces acid sludges, and can be accompanied by a great amount of by-products.[2] Thus, direct chemical synthesis of aniline is of significant interest for the development of more economic and environmentally friendly one-pot reaction process.

The direct route (Scheme 5.2) offers several advantages over the conventional process; however, it has several challenges. The main challenge is the difficulty of activating the benzene's strong C-H bond (BDE = ~113 kcal mol^{-1}) and ammonia's strong N-H bond (~108 kcal mol^{-1}) simultaneously.[3] Utilizing ammonia (NH_3) as an aminating agent is attractive due to low cost and atom efficiency. Another issue associated with the direct process is that the production of hydrogen can drive the reaction toward the formation of benzene, which reduces the yield of aniline. Decomposition of ammonia to N_2 and H_2 at high temperature is also one of the challenges that has to be inhibited to assure a high yield of aniline.

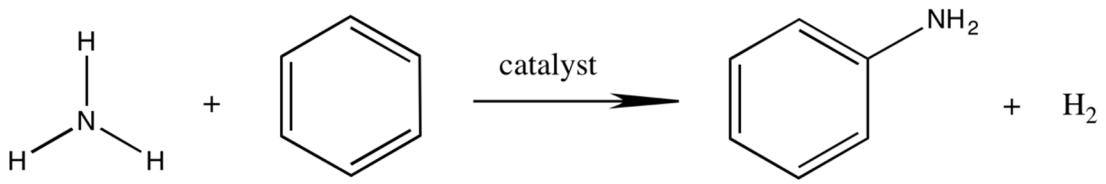

Scheme 5.2 The proposed direct route of the production of aniline.

Despite several experimental efforts,[4–25] a one-pot process has not been adopted yet for commercial applications, mostly due to low aniline yields. Most of the developments in this field are targeted towards the determination of an effective aminating agent, either ammonia or an ammonia derivative, in the presence of an effective catalyst. An oxidizing agent, such as oxygen gas, metal oxide, or hydrogen peroxide is typically required. A significant advance includes the use of the Ni/NiO/ZrO_2 cataloreactant,[19–22] to achieve direct amination of benzene to aniline. The NiO is used as a reducible oxide that can oxidize the produced hydrogen as well as can be easily reduced to metallic Ni^0. Aniline's yield from this reaction is about 13.6% at 623 K and 300 - 400 atm. Hagemeyer *et al.*[5] conducted a large screening study and found that Rh/Ni-Mn/K-TiO_2 cataloreactant produce the best benzene conversion and aniline selectivity. Both Hagemeyer's work[5] and Hoffmann *et al.*[7,8] emphasized the importance of metallic nickel as an active site for the formation of aniline. Hoffmann further proved that elemental Ni is essential to activate benzene's C-H bond and ammonia's N-H bond simultaneously by conducting a temperature-programmed reaction (TPR) experiment of the direct amination of benzene on the Ni/ZrO_2 catalyst at temperature range 523 - 873 K and standard pressure.[7] Although the DuPont's cataloreactant has shown to produce aniline from direct amination of benzene, no information

about the thermodynamics and the electronic properties of some intermediates involved in this reaction are available.

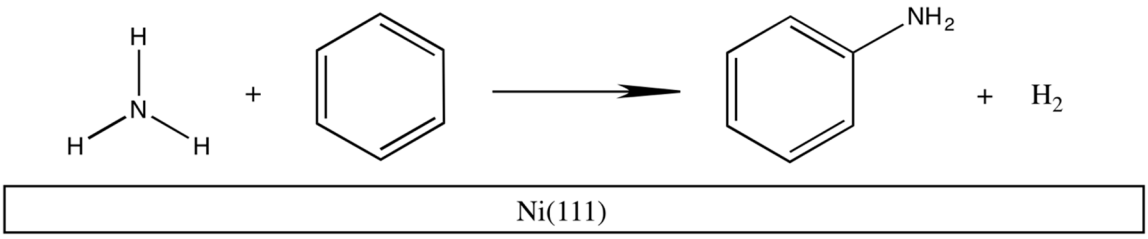

Scheme 5.3 The overall modeled reaction for the direct production of aniline.

To explore possible reaction intermediates and to better understand the role of nickel in direct aniline production, plane-wave DFT calculations were used to study the direct amination of benzene by a Ni(111) surface (Scheme 5.3). DFT modeling of surface reactions has demonstrated the potential for providing molecular-level understanding of heterogeneous catalysts. Adsorption energies, structures, sites, and thermochemical analysis of proposed reaction pathways relevant to the amination of benzene on the Ni(111) surface were investigated. Ni(111) is chosen due to its stability and its efficacy toward the adsorption of aniline.[26,27] It is necessary to examine the adsorption behavior of aniline on the Ni(111) surface in detail, including its adsorption geometry and energy, which has not been, to our knowledge, reported prior, to get information that can facilitate further catalyst design. This study also aims to compare and correlate a heterogeneous Ni(111)–imide model with the previous homogenous nickel-imide model for the C-H amination reaction.[28]

5.2 Computational Details

5.2.1 Method

All calculations were carried out using plane wave density functional theory (PW-DFT) as implemented in the Vienna Ab initio Simulation Package (VASP).[29–32] The electron exchange and correlation energies were addressed using the generalized gradient approximation as proposed by Perdew-Burke-Ernzerhof (GGA-PBE).[33,34] The electron ion interactions were described using the projector augmented wave (PAW) method[35,36] in which inner core electrons are treated using pseudopotentials whereas valence electrons are described by a plane wave basis set. In order to examine the effect of van der Waals (vdW) interactions on the adsorption energy the dispersion corrected DFT-D3[37] approach was used in this study. To obtain accurate energies, convergence tests were run to ensure optimal setting parameters to our calculations, shown in Figures 5.7, 5.8, and 5.9 of the appendix. Plane wave basis sets were expanded within a 400 eV energy cutoff, the Brillouin zone was integrated using 5x5x1 k-points mesh for adsorption systems and only the gamma point was used for gas phase molecules. Since Ni has magnetic properties, spin polarization was considered for open shell molecules and for all adsorption systems to ensure accurate adsorption energies, as recommended by Kresse *et al*.[38] The energy criterion for electronic minimization was 10^{-6} eV and the ions were allowed to relax until all atomic forces were less than 0.02 eV/Å. The Methfessel-Paxton smearing method[39] was used with $\sigma = 0.2$ eV. All calculations were performed at 0 K. Vibrational frequencies were calculated using a 600 eV energy cutoff at the gamma k-point and the force convergence criterion was tightened to be less than 10^{-5} eV/Å. For adsorbed systems, only the adsorbate and the topmost layer were relaxed during the vibrational frequency calculations. The zero point energy (ZPE) correction was added to all adsorption energies as follows:

$$ZPE = \sum_{i=1}^{n} \frac{hv_i}{2} \quad (5.1)$$

where v_i is the calculated real frequency of a system, n is the number of vibrations, and h is Planck's constant. For the electronic density of state (DOS) calculations, the k-point grid was increased to 9x9x1.

5.2.2. Surface Model

The DFT-optimized lattice constant of Ni used to build the slab is 3.52 Å (see Figure 5.7), which agrees well with the experimental lattice constant of Ni, 3.524 Å.[40] The Ni (111) surface was modeled as a five-layer periodic slab in the (111) Miller plane as shown in Scheme 5.4. A vacuum thickness of 10 Å along the c axis was employed between repeated slabs. During the geometry optimization, the top three layers were relaxed and the bottom two layers were kept fixed. The total number of nickel atoms in a slab is 45 atoms per unit cell and the surface unit cell is p(3x3). One molecule was adsorbed for each calculation.

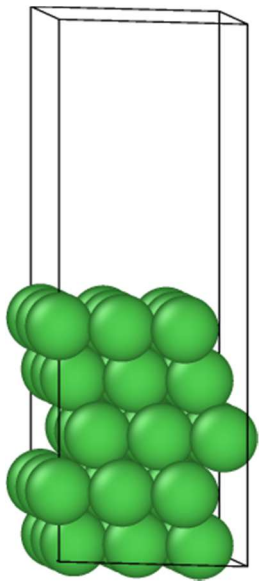

Scheme 5.4 The Ni(111) surface model.

5.2.3 Thermochemistry

As mentioned in Hoffmann's study,[7] the reaction temperature plays a critical role for the selectivity of aniline in the direct amination of benzene. DuPont's direct synthesis reaction was conducted at 623 K and 300 - 400 atm.[21] In an attempt to reduce the pressure needed, Hoffman carried out a TPR experiment of the direct amination of benzene with a prereduced Ni/ZrO_2 as a catalyst at ambient pressure and temperature range 523 - 873 K.[7] The onset formation of aniline was detected at temperatures lower than 600 K. Thus, in order to obtain realistic thermodynamics of the direct amination of benzene on the Ni(111) surface, statistical thermodynamics using the vibrational partition function were utilized to calculate the Gibbs free energies at 523 K as follows:

$$G(T) = H(T) - TS \tag{5.2}$$

where $H(T)$ is the enthalpy of the system and is calculated as

$$H(T) = E_{total} + ZPE + H_{corr} \tag{5.3}$$

where E_{total} is the total energy of the system determined by DFT calculations, ZPE is the zero point energy correction, calculated as shown in eqn (1), and H_{corr} is the thermal correction from 0 K to 523 K and is calculated as

$$H_{corr} = \sum_{i=1}^{n} \frac{h\nu_i}{e^{h\nu_i/k_BT} - 1} \tag{5.4}$$

where k_B is Boltzmann's constant.

Since all the molecules in this study are strongly bound to the Ni(111) surface, the translational and rotational modes are frustrated and replaced by vibrational modes, as suggested

by Blaylock *et al*.[41] The entropy correction to the energy of adsorbates S (shown in eqn (2)) only includes the contribution from the vibrational modes, and it takes the form:

$$S = \sum_{i=1}^{n} \left[\frac{h\nu_i / k_B T}{e^{h\nu_i / k_B T} - 1} - \ln\left(1 - e^{-h\nu_i / k_B T}\right) \right] \tag{5.5}$$

For gaseous molecules, the contributions from the transitional and rotational modes are included within the thermal correction and entropy.

5.2.4 Method Calibration

To validate the utilized method for free molecules, the bond dissociation energy (BDE) of the free molecules in the gas phase were calculated and compared with the available experimental data as shown in Table 5.1. In addition to the calibration, these energies help to correlate the dissociation of these molecules in the gas phase and on the Ni(111) surface. For a molecule AB, the BDE is computed as: BDE = (E_A + E_B) - E_{AB} where E_A and E_B are the calculated total energies of molecule A and molecule B and E_{AB} is the calculated total energy of molecule AB. Homolytic BDE calculations often represent a challenge for DFT due to the difference in electron correlation between a molecule and its fragments. Calculating reaction energies is usually more accurate because of the cancellation of error. Nevertheless, the calculated BDEs displayed in Table 5.1 generally show very good agreement with the experimental bond energies especially when ZPE and thermal correction are added. PBE and PBE-D3 BDEs are very similar. The largest difference between PBE and PBE-D3 is 1.1 kcal mol^{-1} for aniline's C-N BDE, but still within the experimental uncertainty. Therefore, as shown in Table 5.1, no notable improvement in the results is found when including the dispersion corrected functional. From the BDE results, breaking one C-H bond of benzene in the gas phase

is very endothermic, as expected, and requires a large amount of energy. We will show later how the use of a catalyst can help reduce this energetic demand. The same observation is appropriate for the first N-H dissociation energy of ammonia, as well as for NH_2, NH, and aniline. The BDE of aniline shows that breaking the C-N bond of aniline requires higher energy than N-H dissociation.

Table 5.1 Bond dissociation energies (BDE) of gaseous molecules in kcal mol^{-1}.

Bond Cleavage (AB =A+B)	**BDE**				
	PBE	**PBE-D3**	**PBE+ZPE+H_{corr}[a]**	**PBE-D3+ZPE+ H_{corr}[a]**	**Expt.[b]**
$C_6H_6 = C_6H_5 + H$	113.5	113.9	110.1	110.4	112.9±0.6[c]
$H_2 = 2\ H$	104.6	104.6	105.1	105.1	104.2[c]
$NH_3 = NH_2 + H$	112.6	112.6	107.7	107.7	107.6±0.1[c]
$NH_2 = NH + H$	99.5	99.5	97.2	97.2	97.6[d]
$C_6H_5NH_2 = C_6H_5 + NH_2$	107.8	108.7	103.0	104.1	104.2±0.6[c]
$C_6H_5NH_2 = C_6H_5\ NH + H$	94.1	94.6	90.5	90.7	88.0±2.0[e]

[a]Represent *DH* (298 K). [b]Experimental values are at 298 K. [c]Reference 3. [d]Reference 42. [e]Reference 43.

As the adsorption of ammonia and benzene on the Ni(111) surface have been studied before, their experimental adsorption energies were used to further validate the methods used in this study. Table 5.2 shows calculated adsorption energies from this study using PBE, PBE-D3, ZPE corrected adsorption energies, and the experimental adsorption energies for adsorbed ammonia and adsorbed benzene on the Ni(111) surface. Low energy electron diffraction (LEED) experiments[44,45] and previous calculations[46–48] confirmed that the nitrogen atom in ammonia is bound directly to the Ni(111) surface, whereas hydrogen atoms point away from the surface, as shown in Figure 5.1.a. The most stable adsorption site of NH_3 is atop, where the nitrogen atom is

bound directly to a single Ni atom on the surface via the electron lone pair of the N atom of ammonia. In addition, previous experiments[49–51] and calculations[52,53] show that the benzene ring adsorbs parallel to the surface with all hydrogen atoms tilted away from the surface (Figure 5.1.b). Our results agree well with these previous findings. The PBE adsorption energies (shown in Table 5.2) are in excellent agreement with experiments with ≤ 1.0 kcal mol^{-1} difference. When adding the ZPE correction to the PBE adsorption energy of ammonia, the absorption energy is equal to that from experiment, while the ZPE-corrected adsorption energy of benzene becomes 3.0 kcal mol^{-1} lower than the experimental value. This is still in reasonable agreement with experiment, as the experimental error associated with the use of temperature-programmed desorption (TPD) spectroscopy to approximate the adsorption energy of large systems, is estimated to be within 3 kcal mol^{-1}.[54,55] This demonstrates the importance of including the ZPE correction in the calculations of the adsorption energies, and thus the ZPE correction will be included in all adsorption energies. To examine the effect of the vdW interactions on the binding to the metal surface, the semi-empirical PBE-D3 functional was used. The computed adsorption energies for ammonia and benzene using PBE-D3, shown in Table 5.2, shows an overbinding of 9 kcal mol^{-1} for ammonia and 38.4 kcal mol^{-1} for benzene that represent the dispersion energies that contribute to the molecule-metal binding. A large dispersion energy of benzene on other (111) surfaces, such as Pt(111), Pd(111), Ag(111), and Au(111), was also previously obtained using different dispersion corrected methods.[54,56] Grimme *et al*.[37] pointed out that DFT-D3 is a great tool to provide accurate adsorption energies for molecules and solids, in particular for weakly bounded systems (physisorption interactions) where dispersive interactions are dominant. For chemisorbed molecules, such as all the adsorbates in the present study, the interaction between a molecule and a metal surface may not be captured in the DFT-D3 parameterization

and; therefore, leads to a large overbinding for the D3 corrections. DFT-D3 becomes more important when more than one molecules adsorb on the surface. Tonigold *et al.*[57] examined the performance of DFT-D3 on several water-metal systems as compared to PBE, and found that pure PBE adequately described the pure water-metal system adsorption behavior, but if additional adsorbates were added to the surface, then DFT-D3 was more reliable. So, adding a dispersion correction to the molecule-Ni(111) adsorption systems in the current study would not be expected to improve the results relative to experiment, and this is demonstrated by the results in Table 5.2. Since PBE adsorption energies are in excellent agreement with the experiment, the PBE energies will be used later to calculate reaction thermodynamics.

Table 5.2 Adsorption energies (E_{ad}) for ammonia and benzene adsorbed on a Ni(111) surface in kcal mol^{-1}.

Method	**E_{ad}**	
	NH_3/Ni(111) (atop)	**C_6H_6/Ni(111) (bridge)**
PBE	- 16.8	-19.1
PBE + ZPE	- 17.0	- 21.4
PBE-D3	- 25.8	-57.5
PBE-D3+ZPE	- 26.0	-59.8
Expt.	-17.0[a]	-18.0[b]

[a]Reference 58. [b]Reference 50.

a) NH_3^* b) $C_6H_6^*$

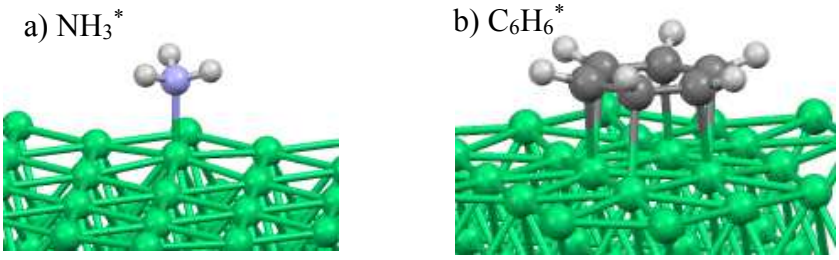

Figure 5.1 Adsorption structure of ammonia (a) and benzene (b) on the Ni(111) surface. (*) Indicates an adsorbed molecule.

5.3 Results And Discussion

5.3.1 Adsorption Geometries and Energies

The first step in surface reactions is usually the adsorption of the species involved in the reaction on the surface. Thus, it is of importance to study their adsorption behaviors. The adsorption behavior of the NH_x (x = 0 - 3) species and the aromatic species involved in the direct amination of benzene on the Ni(111) surface are reported and discussed here. Geometry optimizations were performed for all adsorption systems to find the most stable structure of the molecule-surface interaction, *i.e.*, the most favorable surface site for each adsorption process, which has the lowest adsorption energy. The computed adsorption energy is defined as: $E_{ad} = E_{adsorbate+Ni(111)} - E_{adsorbate} - E_{Ni(111)}$ where E_{ad} is the binding energy of a molecule bound to the surface, $E_{adsorbate+Ni(111)}$ is the calculated total energy of the optimized adsorption system, and $E_{adsorbate}$ and $E_{Ni(111)}$ are the calculated total energies of the isolated molecule and of the clean surface, respectively. As mentioned above, a ZPE correction is added to all total energies. Only the adsorption energies of the most stable structures on the Ni(111) are provided here.

5.3.1.1 NH_3^*, NH_2^*, NH^*, N^*, and H^*

a. Adsorption sites and energies. Both NH_2 and NH interact with the Ni(111) surface like ammonia does (same orientation), that is via the nitrogen atom. However, each species interacts with different active sites (see Figures 5.1.a, 5.2.a, and 5.2.b). Duan *et al.*[46,59] studied the adsorption sites and energies of NH_x species on the Ni(111) surface and found that NH_2 and NH interact with the Ni(111) surface via bridge and fcc sites, respectively, which is consistent with our findings. Duan reported the adsorption energies of NH_x species in two publications.[46,59] The adsorption energies are different in the two papers. Their adsorption energies and the present ones are listed in Table 5.3. Duan's study used 3x3x1 k-points mesh whereas in this study a

higher k-point mesh (5x5x1) was used. Our results are in very good agreement with the data provided by Duan.[46] The calculated adsorption energy of ammonia from this work is identical to the experimental value. It can be observed from Table 5.3 that the adsorption energy decreases (increasing stability) with a decrease in the number of hydrogen atoms going from NH_3 to N, as expected, given an increase in unsaturation of the nitrogen in this order. This is evident giving the different preferred interaction sites from the NH_3/Ni(111) system to the NH/Ni(111) system. Both NH_2-Ni(111) and NH-Ni(111) bindings involve forward donation from the nitrogen's lone-pair electron and the back donation from the d-electrons of the Ni atom(s). More investigations on the electronic properties of NH/Ni(111) and NH_2/Ni(111) systems will be illustrated later. Nitride and hydride both prefer to adsorb on the fcc site of the Ni(111) surface. Hydrogen molecules tend to always adsorb dissociatively on the Ni(111) surface.[38] Several studies on the interaction of a hydrogen atom with different surfaces also demonstrated that the hydrogen atom prefers to interact on the three-fold hollow site.[38] PBE-D3 adsorption energies of NH_x species and H (see Table 5.3), although overestimated, reveal the same trend as PBE adsorption energies, that is they are decreasing (relatively by the same magnitude as PBE) going from NH_3 to N.

Table 5.3 Adsorption sites and adsorption energies (E_{ad}) (in kcal mol^{-1}) for NH_x (x = 0 - 3) species and H adsorbed on a Ni(111) surface.

Adsorbate	**Adsorption sites**	**E_{ad}[a]**				
		PBE	**PBE (Ref. b)**	**PBE (Ref. c)**	**PBE-D3**	**Expt.**
NH_3	atop	-17.0	-17.3	-15.0	-26.0	-17.0
NH_2	bridge	-61.9	-63.0	-60.0	-69.7	-
NH	fcc	-103.8	-105.4	-101.0	-111.0	-
N	fcc	-121.0	-122.2	-119.7	-125.7	-
H	fcc	-64.5	-64.8	-64.6	-68.3	-

[a]ZPE correction is included within the computed adsorption energy. [b]Reference 46. [c]Reference 59. [d]Reference 58.

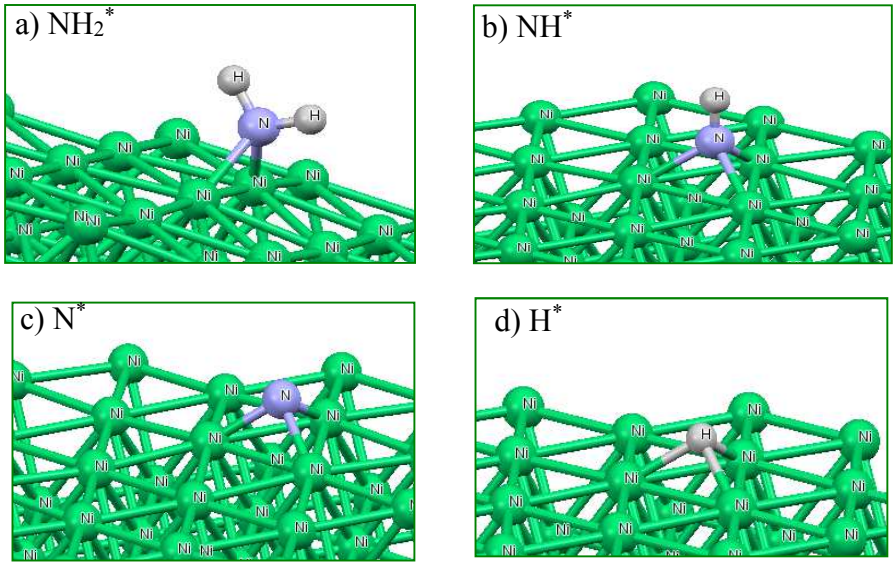

Figure 5.2 Adsorption sites of NH_2 (a), NH (b), N (c), and H (d) on the Ni(111) surface. (*) Indicates an adsorbed molecule.

b. Adsorption geometry. The predicted gas phase structural parameters of NH_3, NH_2, and NH from this work (using PW-PBE) are in excellent agreement with experiments (see Table 5.4). The predicted adsorbed structures of NH_x species agree very well with previous calculations by Duan *et al*.[46] The N-Ni bond distance in the NH_3/Ni(111) system is only 0.06 Å off from the experimental measured distance.[48] The N-H bond length in NH_3 elongates by 0.004 Å when adsorbed on the Ni(111) surface, but the N-H bond shortens by 0.01 Å and 0.03 Å in adsorbed NH_2 and NH, respectively. Differences in the N-H bond length can be attributed to the different molecule-surface electronic interaction for each system. Furthermore, the HNH bond angles open by 2.0° and 2.2° in NH_3 when adsorbed on the Ni(111), whereas it opens by 5.1° in adsorbed NH_2. This expansion is due to the shape of the NH_3 and NH_2 becoming more tetrahedral via adsorption. The distance between N and Ni decreases in the direction NH_3 (2.03 Å), NH_2 (1.93 Å), and NH (1.84 Å) highlight the strong binding of NH. In the N/Ni(111) system, the N-Ni bonds are the shortest among other N-Ni bonds, see Table 5.4, so when nitrogen gets

more unsaturated it binds very tightly to the surface. Hydride, on the other hand, greatly overlaps with the Ni atoms resulting in shorter H-Ni bonds compared to the N-Ni bond lengths, but the NiHNi angles are larger than the NiNNi (in adsorbed nitride) by 2.4°.

Table 5.4 Bond lengths (r) in Å and bond angles (a) in degree of free and adsorbed NH_x (x = 1 - 3) species, adsorbed N, and adsorbed H.

System	r(N-H)	a(HNH)	r(N-Ni) [r(H-Ni)]
NH_3	1.021	106.5	-
NH_3 (expt.)	1.021[a], 1.023[b]	106.7	-
NH_3/Ni(111)	1.025	108.5, 108.7	2.031
NH_3/Ni(111)(expt.)	-	-	1.97[c]
NH_2	1.037	102.5	-
NH_2 (expt.)	1.024[a], 1.038[b]	103.4, 102.4[c]	
NH_2/Ni(111)	1.025	107.6	1.932, 1.931
NH	1.051	-	-
NH (expt.)	1.036[a], 1.051[b]		
NH/Ni(111)	1.025	-	1.835
N/Ni(111)[d]	-	-	1.759
H/Ni(111)[e]	-	-	[1.702]

[a]Experimental bond lengths from Reference 60 (for NH_3 and NH_2) and Reference 61 (for NH). [b]Calculated bond lengths (using periodic PW91 functional) from Reference 62. [c]Reference 63.
[d]a(NiNNi) = 93.0°. [e]a(NiHNi) = 95.4°.

c. Vibrational Frequencies. In order to obtain a more complete picture of bond strengths and the structural change via adsorption, the vibrational frequencies of gaseous and adsorbed NH_x species were calculated and are organized in Table 5.5. Experimental vibrational frequencies of gas phase NH_3, NH_2, and NH and of adsorbed NH_3 on Ni(111) are also given in Table 5.5. The predicted vibrational frequencies from this work (not corrected for anharmonicity) are in reasonable agreement with available experimental frequencies. When comparing the calculated frequencies in gas phase and in adsorption, the decrease in the vibrational modes of NH_3 via adsorption is plausible owing to introducing the N-Ni binding that slightly weakens the N-H

bonds. This decrease ranges between 45 to 30 cm^{-1} in the frequencies; however, only the HNH wagging mode increased by 112 cm^{-1} via adsorption consistent with enlarging of this angle, as discussed earlier. On the other hand, the frequencies of NH_2 and NH has increased upon adsorption confirming the finding that the N-H bonds in these molecules become stronger when interacting with Ni(111) surface.

Table 5.5 Vibrational frequencies (in cm^{-1}) of free and adsorbed NH_3, NH_2, and NH.

	Gas phase[a]	**Adsorbed on a Ni(111) surface[a]**	**Gas phase (expt.)[b]**	**Adsorbed on a Ni(111) surface (expt.)[c]**
NH_3				
N-H stretch (*e*)	3505	3465	3444	3360
	3504	3459	3444	
N-H stretch (a_1)	3380	3341	3337	3270
HNH Bend (*e*)	1623	1593	1627	1580
	1623	1590	1627	
HNH Bend (a_1)[d]	1025	1137	950	1140
NH_2				
N-H stretch (a_1)	3349	3438	3301	
N-H stretch (a_1)	3254	3358	3219	
HNH Bend (b_2)	1497	1514	1497	
NH				
N-H stretch	3169	3397	3283	

[a]This work. [b]Reference 64 (for NH_3), reference 65 (for NH_2), and reference 66 (for NH). [c]Reference 67. [d]HNH wagging mode.

5.3.1.2 C_6H_6*, C_6H_5*, $C_6H_5NH_2$*, and C_6H_5NH*

a. Adsorption sites and energies. As mentioned above, benzene adsorbs parallel to the surface with all hydrogen atoms tilted away with respect to the surface (Figure 5.1.b). The calculated adsorption energy of benzene including the ZPE correction is -21.4 kcal mol^{-1} (see Table 5.6) coming mostly from π-interactions. The adsorption energy of phenyl on the Ni (111) surface is

more stable than that of adsorbed benzene by ~30 kcal mol^{-1}, see Table 5.6. The strong binding of phenyl compared to benzene is due to the strong σ-interaction introduced in the phenyl/Ni(111) system that is not present in the benzene/Ni(111) system (only π-interactions) resulting in different adsorption structures between these two systems. Phenyl adsorbs tilted with respect to the surface on the fcc site Figure 5.3.a, which is a stronger binding site than the bridge site (benzene's most stable site). This adsorption orientation of phenyl was also found by Feng *et al*.,[68] but their adsorption energy of phenyl using the PBE method and slab model (using different parameters compared to our study) is lower than ours by 92.8 kcal mol^{-1}. Feng *et al*.[68] also predicted an adsorption energy of benzene adsorbed on the bridge site that is 22.8 kcal mol^{-1} lower than the experimental adsorption energy of benzene. The adsorption energy of phenyl when adsorbed nearly vertical to the Ni(111) surface on the hcp site is found to be less stable than the tilted phenyl by approximately 3 kcal mol^{-1}, as the former loses some of the π-interactions (see Figure 5.11.a in the appendix). Higher adsorption energy of phenyl is predicted when adsorbed vertically on the bridge site, in which the π-electron interactions decrease the most (Figure 5.11.b**)**. The vertical orientation of phenyl may be likely when few binding sites are available on the Ni(111) surface.

Table 5.6 Adsorption sites and adsorption energies (E_{ad}) (in kcal mol^{-1}) of the aromatic species adsorbed on a Ni(111) surface.

Adsorbate	**Adsorption sites**	**E_{ad}[a]**		
		PBE	**PBE-D3**	**Expt.[b]**
C_6H_6 (parallel)	bridge	-21.4	-59.8	-18.0
C_6H_5 (tilted)	fcc	-51.1	-88.1	-
$C_6H_5NH_2$(parallel)	bridge, and atop	-20.4	-63.6	-
C_6H_5NH (vertical)	bridge	-38.7	-56.9	-

[a]ZPE correction is included within the computed adsorption energy. [b]Reference 50.

Previous studies of the adsorption of aniline on nickel surfaces showed slightly different adsorption behavior of aniline. On evaporated Ni films, aniline was found using X-ray photoelectron spectroscopy (XPS) to adsorb molecularly by π-electrons and dissociatively as an anion formed from losing a proton from the amino group.[69] Studies by Huang and co-workers[26,27] on the adsorption of aniline on Ni(100) and Ni(111) using fluorescence yield near-edge spectroscopy (FYNES) and (TPR) techniques revealed that adsorption of aniline is a structure sensitive reaction and that the Ni(111) surface is considered the most stable for the adsorption of aniline, where aniline does not easily undergo hydrogenolysis and hydrogenation until temperatures of ~ 800 K and higher. Huang *et al*.[26] concluded that aniline adsorbs on the Ni(111) surface at a small angle via π-interactions only, whereas Myers *et al*.[70] suggested that aniline form an unreactive surface polymer (polyaniline) when adsorbed on the Ni(111) surface that is stable to above 600 K. Same polyaniline was found on Ni(100) surface.[71] In Hoffmann's TPR experiment,[7,8] aniline was the only aromatic molecule detected below 610 K. When relaxing the aniline/Ni(111) system starting from various initial structures, in the current study, we found that aniline always interacts with the Ni(111) surface not only on the bridge site via the aromatic ring π−interactions but also on the atop site via the amino group σ-interaction, see Figures 5.3.b and 5.4.a. The adsorption energy of aniline is higher (less stable) than that for benzene by 0.9 kcal mol $^{-1}$ indicating a slightly weaker π-interaction between aniline and the Ni(111) surface compared to benzene. In addition, the N atom in aniline interacts slightly less strongly with the Ni(111) surface than the N atom in ammonia. To confirm the adsorption structure of aniline, a large slab model (5x5x4) of Ni(111) surface was constructed to study the adsorption of aniline (Figures 5.4.b and 5.4.c). The adsorption energy of aniline on the larger supercell p(5x5) is -26.3 kcal mol^{-1}, lower (more stable) by ~6 kcal mol^{-1} than the adsorption

energy of aniline on the smaller supercell p(3x3). Aniline rotates on the large surface and adsorbs on different kind of the bridge site (Figure 5.4.b), bridge site B (also known as bridge 0°), compared to the adsorption on bridge site A (bridge 30°) on the p(3x3)-Ni(111) surface unit cell (Figure 5.4.a). Aniline is found to be unstable on the hollow sites. Thus, the most stable adsorption orientation of aniline is predicted to be via bridge site B and atop site. For consistency the total energy of aniline adsorbed on the p(3x3) is used in calculating reaction thermodynamics. Anilide, $N(H)C_6H_5$, observed on evaporated nickel films,[69] prefers to adsorb vertically on the Ni(111) surface on a bridge site (see Figure 5.3.c) with an adsorption energy that is higher than vertical phenyl by 2.1 kcal mol^{-1} (Figure 5.11.b), which can be attributed to the C-Ni bond being stronger, in which the aromatic ring directly interacts with the surface, than N-Ni bond (the aromatic ring is away from the surface and causing a steric effect). The shortest C-Ni bond length in vertically adsorbed phenyl is 1.953 Å versus 1.974 Å for the N-Ni bond length in adsorbed anilide.

Similar to benzene, the PBE-D3 predicts lower adsorption energies for phenyl, aniline, and anilide in comparison to the PBE adsorption energies. This overestimation may involve the contribution of the vdW interactions to the molecule-metal binding, which is known to be significant for aromatic systems (see Table 5.6). The dispersion energy of phenyl is very close to benzene, whereas aniline has about 5 kcal mol^{-1} larger dispersion energy than benzene according to the PBE-D3 results. As anticipated, anilide has the lowest dispersion energy among the adsorbed aromatic species because the ring is not very close to the surface. The difference in adsorption energy between parallel-adsorbed benzene and tilted-adsorbed phenyl is 30.0 kcal mol^{-1} when using PBE and PBE-D3. Thus, PBE-D3 still provides correct qualitative trends of the adsorption energies.

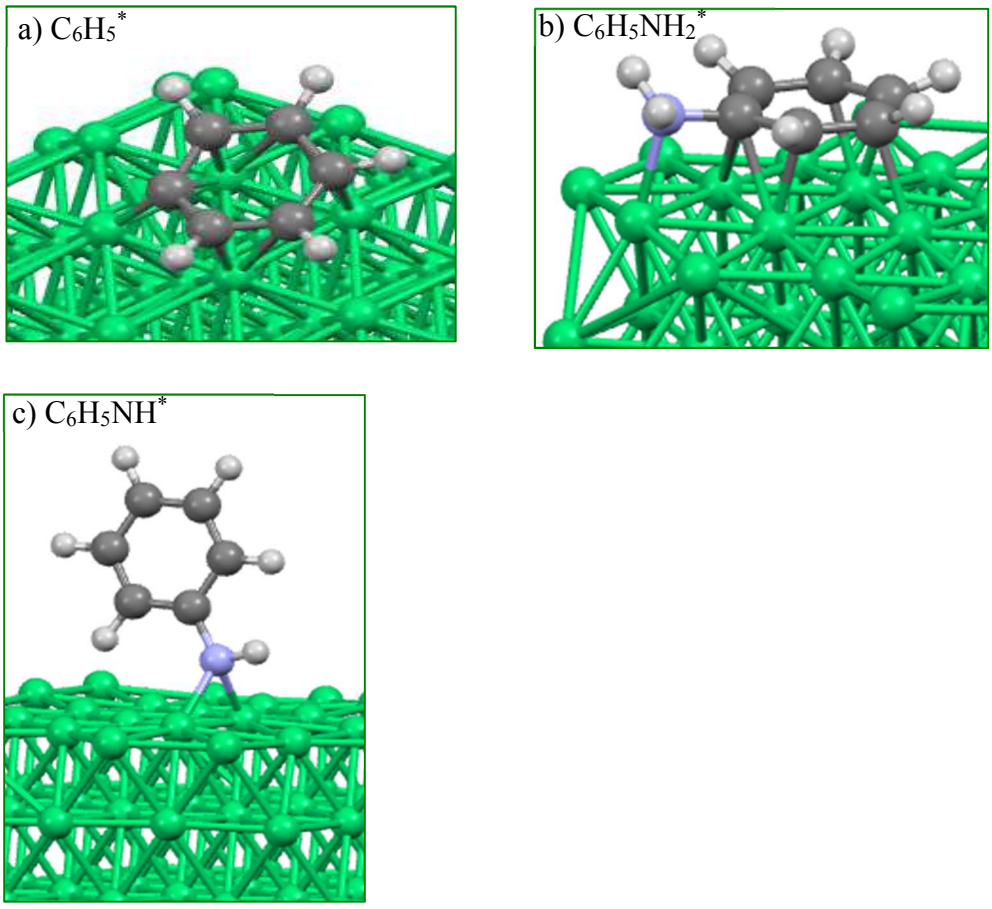

Figure 5.3 Adsorption sites of phenyl (a), aniline (b), and anilide (c) on the Ni(111) surface. (*) Indicates an adsorbed molecule.

b. Adsorption geometry. Important structural parameters of the free and adsorbed aromatic species are shown in Table 5.7 and Table 5.8. A full list can be found in Table 5.14 and Table 5.15 of the Appendix. The C-C bonds in phenyl elongate, similar to benzene, when adsorbed on the Ni(111) surface by 0.02 - 0.08 Å (see Table 5.7) resulting in a decrease in the bond order and a degree of molecular distortion that can also be seen from the changes in the CCH bond angles (Table 5.14). The C-H bond lengths of phenyl do not exhibit major changes via adsorption except that they become titled out of the plane of the aromatic ring, as shown in Figure 5.3.a. The C-Ni bonds in adsorbed phenyl vary in length, ranging from 1.905 to ~2.5 Å. The gradual

increase in the C-Ni bond lengths confirms that phenyl tilts from the surface, suggesting that it interacts with Ni(111) in both a σ fashion (through the shortest 1.905 Å bond) as well as π-interactions with the remainder of the ring. This is in contrast to the C-Ni distances in adsorbed benzene, which are all similar, ~ 2.1 Å.

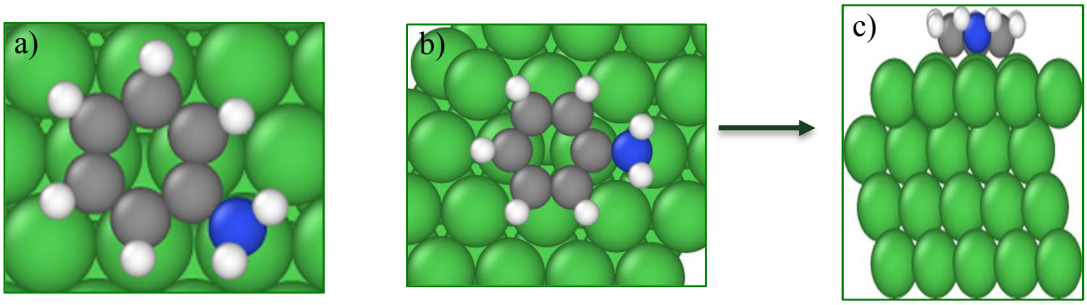

Figure 5.4 A top view of aniline adsorbed on the p(3x3) surface unit cell of Ni(111) on bridge site A (a), on the p(5x5) surface unit cell on bridge site B (b), and a side view of aniline adsorbed on the large 5x5x4 Ni(111) slab model.

Likewise in aniline, the C-C bonds get longer upon adsorption and the ring loses some degree of unsaturation. The C-Ni bond lengths in aniline range from 2.04 to 2.09 Å, almost similar to adsorbed benzene, except the two C_{ipso}-Ni bond distances (Table 5.8). The carbon atom connected to the amino group (C_{ipso}) in adsorbed aniline interacts with two Ni atoms (bridge sites) making the two C_{ipso}-Ni bond distances longer (2.585 Å and 2.133 Å). The perpendicular distance between the C_{ipso} and the surface, though, is still ~2.1 Å, as shown in Figure 5.3.b. Thus, the aromatic ring in aniline adsorbs parallel to the Ni(111) surface. The N-Ni distance in adsorbed aniline is also 2.1 Å, which is similar to the C-Ni bond lengths but longer by 0.07 Å than the N-Ni bond length in adsorbed ammonia. This is consistent with ammonia being a better σ donor than aniline. A steric effect may also play a role here in hindering the N atom from binding strongly to the Ni(111) surface. In addition, the HNH bond angle of the amino

group in adsorbed aniline also opens as in adsorbed ammonia to accommodate a more tetrahedral configuration about nitrogen.

Table 5.7 Bond lengths (r) in Å of free and adsorbed benzene and phenyl.

System	r(C-H)	r(C-C)	r(C-Ni)
C_6H_6	1.091	1.397	-
C_6H_6 (expt.)[a]	1.084	1.397	-
C_6H_6/Ni(111)	1.093, 1.095	1.434, 1.450	2.060, 2.085
C_6H_5	1.091, 1.092	1.405, 1.376, 1.398	-
C_6H_5(tilted)/Ni(111)	1.092, 1.095	1.438, 1.459, 1.433	2.237, 2.002, 2.411, 2.076, 2.487, 2.305, 1.905

[a]Reference 60.

In adsorbed anilide, four of the C-C bonds of the aromatic ring (two C_{ipso}-C bonds and the other two C-C bonds that are parallel to them) become shorter instead of becoming longer via adsorption as it is the case in aniline, benzene, and phenyl. The C-C bonds in adsorbed anilide are all longer than the ones in adsorbed aniline. The C-N bond in anilide elongates by 0.076 Å via adsorption, while it is still shorter than the C-N bond in adsorbed aniline. The nitrogen atom in adsorbed anilide interacts with the Ni(111) via bridge sites as the same fashion as it is in adsorbed amide (see Figure 5.1.a and Figure 5.3.c). Because of the steric effect resulting from the aromatic ring in anilide, the N-Ni bonds in adsorbed anilide are longer by 0.065 and 0.044 Å and the $NiNC_{ipso}$ angle opens about 10° larger than the NiNH angle of adsorbed amide. That can explain why the adsorption energy of anilide is predicted to be higher than amide's adsorption energy by 24 kcal mol^{-1}.

Table 5.8 Bond lengths (r) in Å and bond angles (a) in degree of free and adsorbed aniline and anilide.

System	r(C-H)	r(N-H)	r(C-C)	r(C-N)	r(C-Ni)	r(N-Ni)
$C_6H_5NH_2$ [a]	1.091	1.014	1.407, 1.393, 1.398	1.394	-	-
$C_6H_5NH_2$ (expt.)[b,c]	1.084		1.397, 1.394	1.402	-	-
$C_6H_5NH_2$/Ni(111)[d]	1.090, 1.096	1.021	1.433, 1.448, 1.456, 1.452	1.435	2.056, 2.094, 2.040, 2.585, 2.133	2.084
C_6H_5NH	1.091	1.032	1.407, 1.383, 1.437	1.340	-	
C_6H_5NH/Ni(111)[e]	1.103, 1.091	1.030	1.392, 1.398, 1.410	1.416		1.995, 1.974

[a]a(HNH) = 112.7°. [b]Reference 72. [c]a(HNH) = 113.1°. [d]a(HNH) = 110.0°. [e]a($NiNC_{ipso}$)= 127.4°.

c. Vibrational Frequencies. The calculated vibrational frequencies of C-H, C-C, N-H, and C-N bonds of free and adsorbed benzene, phenyl, aniline, and anilide are given in Table 5.9, as well as their experimental frequencies in the gas phase and the experimental frequencies of benzene adsorbed on the Ni(111) surface. A full list of the calculated frequencies can be found in Table 5.16 of the Appendix. Calculated gas phase frequencies are in good agreement with experiments although not corrected for anharmonicity. From the lower C-C bond frequencies of adsorbed benzene, phenyl, and aniline compared to the C-C in the gas phase, it is reasonable to conclude that the adsorbed C-C bonds are not as strong as they are in the gas phase, mostly because of their contribution to the π-interactions with the Ni (111) surface. The frequency of the C-C bond of aniline only decreases by 59 cm^{-1} when adsorbed on the Ni(111) compared to a 147 cm^{-1} decrease in the same frequency for benzene, which supports our proposal that aniline has higher adsorption energy than benzene because it involves weaker π-interactions, which also can be seen from the slight differences in the C-Ni bond lengths in aniline compared to benzene, as

mentioned in the former section. On the other hand, the C-C stretch frequencies of adsorbed anilide become higher by 27 cm^{-1} versus the gas phase indicating a stable aromatic ring. No large differences in the C-H stretch modes are seen between the gas phase and the adsorbed molecules, although they become slightly lower with adsorption. The C-H bond lengths do not change much via adsorption since hydrogen atoms tilt away from the surface. Like the C-H stretching modes, the N-H stretching modes display no significant differences in the frequencies between gas phase and adsorbed molecules. The C-N stretching modes of aniline and anilide exhibit a high decrease in the frequencies between free and adsorbed molecules. Although the C-N bond becomes longer via adsorption, aniline was found to be stable against hydrogenolysis when adsorbed on the Ni(111) surface in the presence of hydrogen but at very high temperature (more than 800 K).[26]

Table 5.9 C-H, C-C, C-N, and N-H vibrational frequencies (in cm^{-1}) of gas phase and adsorbed C_6H_6, C_6H_5, $C_6H_5NH_2$, and C_6H_5NH.

	Gas phase[a]	**Adsorbed on a Ni(111) surface[a]**	**Gas phase (expt.)[b]**	**Adsorbed on a Ni(111) surface (expt.)[c]**
C_6H_6				
C-H stretch (e_1u)	3122	3086	3062	3025
	3121	3084	3068	
	3106	3074	3063	
	3105	3065	3047	
C-C stretch (e_2g)	1586	1439	1596	1425
	1586	1422	1596	
C_6H_5				
C-H stretch (a_1)	3108	3089	3086	
	3105	3084	3072	
	3093	3071	3037	
	3088	3061	3060	
C-C stretch (b_2)	1590	1426	1593	
	1527	1421	1497	
$C_6H_5NH_2$				
N-H stretch (b_2)	3580	3486	3500	
(a_1)	3479	3394	3418	
C-H stretch (b_2)	3125	3096	3053	

Table 5.9 Continued.

(a_1)	3108	3087	3041
C-C stretch (a_1)	1612	1553	1619
(b_2)	1599	1446	1590
C-N stretch (a_1)	1280	1137	1279
C-H bending (a_1)	1168	1114	1173
C_6H_5NH			
N-H stretch	3313	3291	
C-H stretch	3129	3129	
	3122	3113	
C-C stretch	1551	1578	
	1522	1566	
C-N stretch	1303	1237	
	1155	1196	

[a]This work. [b]Reference 64 (for C_6H_6), reference 73 (for C_6H_5), and reference 74 (for $C_6H_5NH_2$). [c]Reference 75.

5.3.2 Decomposition Reactions

Reaction energies (ΔE), reaction enthalpies (ΔH) at 523 K, and reaction free energies (ΔG) at 523 K were calculated for several decomposition reactions and are listed in Table 5.10 and 5.11.

5.3.2.1 Decomposition of Ammonia

Ammonia decomposition on close-packed surfaces of reactive transition metals requires high pressure and temperature to overcome the decomposition barrier.[76] The use of NiO in DuPont's cataloreactant may have favored the decomposition of ammonia into the NH_x species, as Hoffman *et al*.[7] found that no NH_3 was detected above 523 K, meaning that the Ni surface were covered with NH_x species. Adsorption of ammonia on the Ni(111) surface is an exergonic reaction but can decompose by increasing the heat.[7] The reaction energy, enthalpies and free energies are shown in Table 5.10. Breaking two N-H bonds of ammonia to produce imide (NH_3^*

➔ $NH^* + 2\ H^*$) shows the lowest reaction enthalpy (-20.1 kcal mol^{-1}), followed by breaking the N-H bond of amide (NH_2^* ➔ $NH^* + H^*$) (-13.7 kcal mol^{-1}), and (NH_3^* ➔ $NH_2^* + H^*$) (-6.4 kcal mol^{-1}). Finally, the decomposition of NH^* to H^* and N^* displays the highest reaction enthalpy. According to the present results, the decomposition of ammonia on the Ni(111) surface to imide is the most favorable, thus, imide is predicted to be the most prevalent species on the Ni(111) surface among NH_x species, although amide cannot be ruled out, while nitride seems less likely as does undissociated ammonia, which is consistent with Daun's calculations of the activation energies.[46] Daun's found that the lowest energy barrier corresponds to the dehydrogenation of the NH_2^* to give NH^* and H^*, in which NH_2^* diffuses on the surface from the moderate binding bridge site to the strong binding fcc site. The adsorption energy of NH_2 on the fcc site is higher than the bridge site by 7 kcal mol^{-1} (see Figures 5.10.a in the Appendix and 5.2.a), but the imide species binds more strongly and are more stable than amide on the fcc site (Table 5.3). A recent experimental study of the decomposition of ammonia on the closed-packed surface Co(0001), which is anticipated to carry similar reactivity of the Ni (111) surface, found that imide is the most stable species among the NH_x species and can be selectively produced using the electron-induced dissociation technique at low temperature.[76] Gibbs free energies of the decomposition reactions of ammonia on the Ni(111) surface at 523 K predicted that these reaction are exergonic (except the dehydrogenation of imide), see Table 5.10, with the imide-Ni(111) being the most favorable decomposition reaction of ammonia at this temperature. The differences between ΔH and ΔG are small as shown from the results in Table 5.10 indicating small contributions from the entropies.

Table 5.10 Reaction energies ΔE, enthalpies ΔH, and free energies ΔG of the adsorption and decomposition reactions of ammonia on the Ni(111) surface, all in kcal mol^{-1}.[a]

Reaction pathways	ΔE	ΔH (523 K)	ΔG (523 K)
$NH_3 + * \xrightarrow{\Delta} NH_3^*$	-17.0	-22.0	-19.0
$NH_3^* + * \xrightarrow{\Delta} NH_2^* + H^*$	-4.1	-6.4	-3.5
$NH_3^* + 2* \xrightarrow{\Delta} NH^* + 2H^*$	-15.6	-20.1	-14.4
$NH_2^* + * \xrightarrow{\Delta} NH^* + H^*$	-11.5	-13.7	-10.9
$NH^* + * \xrightarrow{\Delta} N^* + H^*$	5.1	3.3	5.4

[a](*) Indicates an adsorbed molecule.

5.3.2.2 Decomposition of Benzene

As shown in Table 5.11, the decomposition of benzene to phenyl and hydrogen on the Ni(111) surface is thermodynamically less favorable than the adsorption of benzene on the Ni(111) surface. This result is expected given the difficulty to activate the C-H bond and the high stability of the benzene ring. However, compared to the energy required to break the benzene's C-H bond in the gas phase (113 kcal mol^{-1}), Table 5.1, the use of the Ni(111) surface does reduce the endothermicity of breaking the C-H bond by ~99 kcal mol^{-1}. These results lead to the conclusion that benzene is more stable on the Ni(111) surface than phenyl and the C-H bond can be possibly activated at high temperature.

Table 5.11 Reaction energies ΔE, enthalpies ΔH, and free energies ΔG of the adsorption and decomposition reactions of benzene on the Ni(111) surface, all in kcal mol^{-1}.[a]

Reaction pathways	ΔE	ΔH (523 K)	ΔG (523 K)
$C_6H_6 + * \xrightarrow{\Delta} C_6H_6^*$	-21.4	-25.1	-22.1
$C_6H_6^* + * \xrightarrow{\Delta} C_6H_5^* + H^*$	5.3	1.8	6.8

[a](*) Indicates an adsorbed molecule.

5.3.3 Production of Aniline

Hoffman *et al.*[7] represented a kinetic study of the semi-batch oxidative synthesis of aniline catalyzed by NiO/ZrO_2 and found that temperature is a critical parameter to move the

reaction forward. Full coverage of NH_x species on the Ni surface is also required for the formation of aniline so that it can control the adsorption geometry of benzene on the nickel surface.[7,8] Hoffman suggested that an adsorbed phenyl-type intermediate would be possible for this process, yet no confirmation of this proposal has been provided. In this section, possible reaction pathways between imide and benzene, since they are likely the most prevalent (stable) species on the surface, are proposed and investigated based on their reaction enthalpies and reaction free energies at 523 K. Surface reactions generally go through a catalytic cycle comprised of elementary steps, beginning with adsorption, then reaction, and finally desorption. Two mechanisms common in surface reactions are the Langmuir-Hinshelwood and Rideal-Eley mechanisms.

5.3.3.1 Langmuir-Hinshelwood Mechanism

In this mechanism, all reactants involved in the reaction are adsorbed on the surface before reacting. Under this scheme, two reaction processes for the production of aniline were proposed: insertion and stepwise, see Table 5.12 and Scheme 5.5. The first reaction pathway entails direct insertion of the imide into a C-H bond of adsorbed benzene generating new C-N and N-H bonds and thus coordinated aniline. Then, aniline is desorbed. The overall reaction is endergonic and must be aided with heating and/or pressure, as it is also endothermic by 21.5 kcal mol^{-1} at 523 K.

The second reaction pathway modeled is a stepwise formation of the C-N and N-H bonds. The first step proceeds by a C-H bond activation in which a benzene's C-H bond breaks and a Ni-C bond forms, resulting in C_6H_5/Ni(111) and NH_2/Ni(111). These two species react in the second exothermic step akin to a C-N formation process to produce aniline, which would then be desorbed from the Ni(111) surface. The overall process is, of course, also endothermic

by ~21.4 kcal mol^{-1} at 523 K, but the calculations are interesting in that they suggest that the initial C-H activation step is disfavored (ΔH = 24.5 kcal mol^{-1}) relative to the second C-N formation step (ΔH = -3.1 kcal mol^{-1}). The uphill nature of the first step is consistent with the dehydrogenation of benzene on the Ni(111) being unfeasible, as shown earlier. In part, this disfavorability of the first step can be attributed to the loss of some of the π-interactions between the aromatic ring and the surface in phenyl as compared to the adsorbed benzene, Figures 5.1.b and 5.3.a. The ΔG of this reaction also favors the second step over the benzene's C-H bond activation indicating that formation of aniline is more entropically favored than the formation of phenyl.

Table 5.12 Reaction energies ΔE, enthalpies ΔH, and free energies ΔG of the proposed reaction processes of the production of aniline on the Ni(111) surface, all in kcal mol^{-1}.[a]

Reaction processes of the production of aniline	ΔE	ΔH (523 K)	ΔG (523 K)
Langmuir-Hinshelwood mechanism			
I. Insertion			
$NH^* + C_6H_6^* \xrightarrow{\Delta} C_6H_5NH_2^* + ^*$	17.0	21.5	14.8
II. C-H activation/C-N formation			
$NH^* + C_6H_6^* \xrightarrow{\Delta} NH_2^* + C_6H_5^*$	24.9	24.5	25.2
$NH_2^* + C_6H_5^* \xrightarrow{\Delta} C_6H_5NH_2^* + ^*$	-8.0	-3.1	-10.4
Rideal-Eley mechanism			
I. Coupling			
$NH^* + C_6H_6 + ^* \xrightarrow{\Delta} C_6H_5NH^* + H^*$	0.9	-2.6	-2.0
$C_6H_5NH^* + H^* \xrightarrow{\Delta} C_6H_5NH_2^* + ^*$	-5.3	-1.8	-6.8

[a](*) Indicates an adsorbed molecule.

5.3.3.2 Rideal-Eley Mechanism

In this reaction, not all of the reactants needed to be adsorbed prior to reacting. It is possible that a gas phase reactant collides with a preadsorbed molecule on the surface. In the third modeled reaction pathway, benzene is introduced to a preadsorbed imide on the Ni(111) surface to produce H/Ni(111) and the $N(H)C_6H_5$/Ni(111), bound anilide, in which the aromatic ring is nearly perpendicular to the surface and bound to the Ni(111) surface via N atom. A

coupling between NHC_6H_5 and H is followed to produce aniline. The first step in this reaction pathway is more thermodynamically favorable (slightly exothermic) than the first step in the second reaction pathway (C-H activation/C-N formation reaction), see Scheme 5.5. The computed difference between these steps is 27.1 kcal mol^{-1} favoring the production of anilide. Another reason for the production of surface-bound anilide/hydride being more favored than the amide/phenyl is the existence of the hydrogen, which adsorbs strongly to the Ni(111) surface (-64.5 kcal mol^{-1}, Table 5.3). Both steps in this reaction are exergonic processes indicating that binding via nitrogen is entropically favored. This reaction pathway is highly likely to achieve the direct production of aniline. Although high temperatures are needed for the desorption reaction.

Table 5.13 Reaction energies ΔE, enthalpies ΔH, and free energies ΔG of the desorption reaction of aniline on the Ni (111) surface, all in kcal mol^{-1}.[a]

Reaction process	ΔE	ΔH (523 K)	ΔG (523 K)
Desorption of aniline			
$\mathbf{C_6H_5NH_2^* \xrightarrow{\Delta} C_6H_5NH_2 + *}$	20.3	25.1	22.1

[a](*) Indicates an adsorbed molecule.

5.3.4 Desorption of Aniline

Desorption of aniline is calculated to cost 25.1 kcal mol^{-1} thermal energy at 523 K, as shown in Table 5.13. Thus, heat is needed to overcome this barrier. Because the desorption reaction involves increasing in entropy, owing to conversion from being surface-bound to gas phase, the enthalpy barrier has to be overcome for this reaction to proceed.

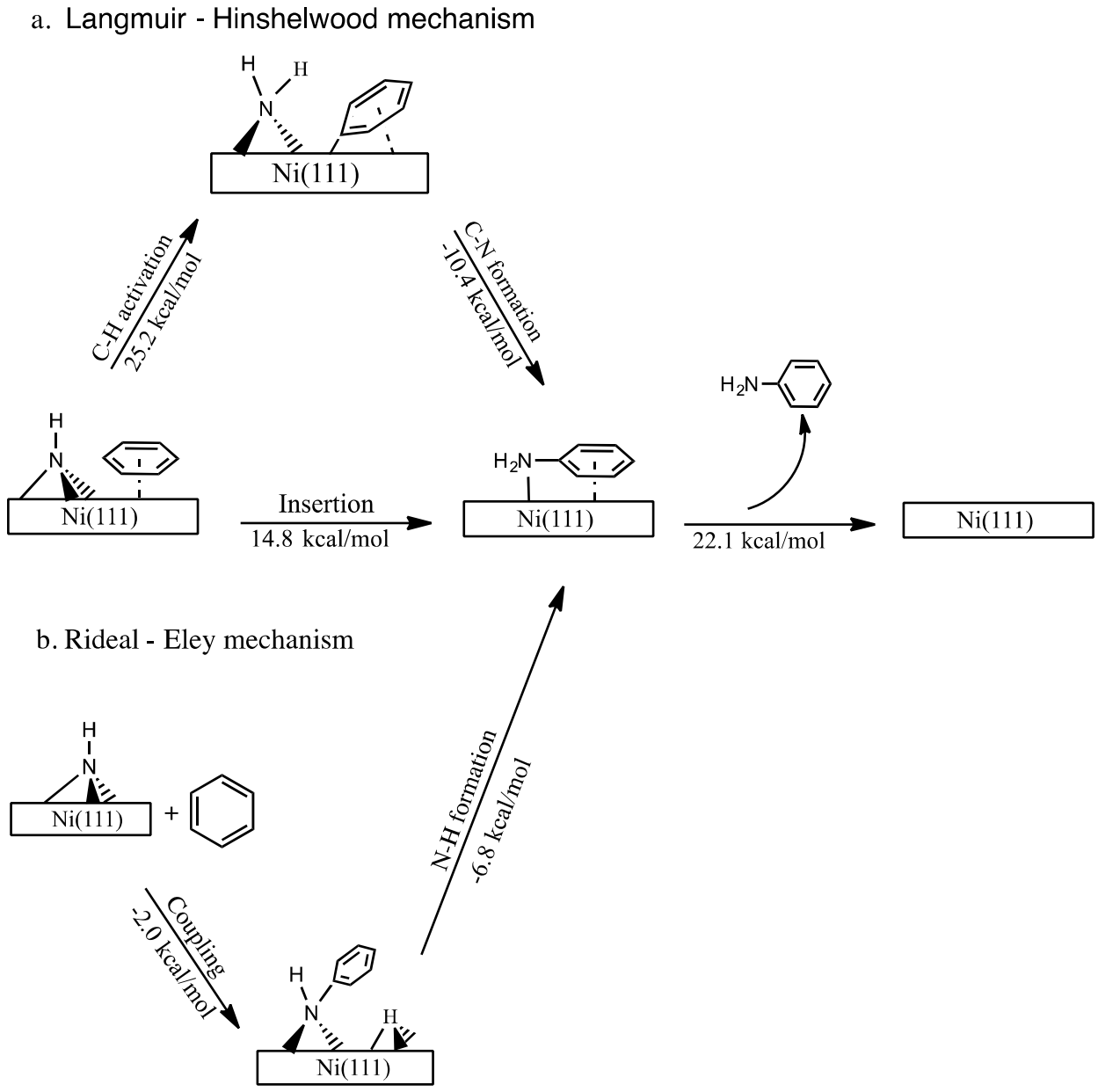

Scheme 5.5 Possible reactions pathways for the production of aniline and the change in the reaction free energies for each process.

5.3.5 Density of States

In order to interpret the electronic structure of the NH/Ni(111) and NH_2/Ni(111) systems, the density of states of these systems and of the clean Ni(111) surface were calculated.

Furthermore, the local density of state (LDOS) was also calculated for the N atom in the isolated molecules as well as in the adsorption systems. The LDOS for the Ni atom interacting with the N atom in the adsorption system was also calculated. Since the findings of the DOS and LDOS for the NH_2/Ni(111) system and the NH/Ni(111) system are similar, only the results of the later will be discussed. The results of the DOS and the LDOS of the NH_2/Ni(111) system are displayed in Figure 5.12 of the Appendix.

Figures 5.5.a and 5.5.b show the LDOS of the N atom in the isolated NH and in the NH/Ni(111) system, respectively. Each LDOS shows the contributions from s, p, and d bands in the electronic structure. Figures 5.5.c and 5.5.d show the DOS of the clean Ni(111) surface and the LDOS of one of the Ni atoms that interact with the NH, respectively. The Fermi level is set to 0 eV, hence all energies are relative to the Fermi energy, E_f, which represents the energy of the highest occupied electronic state.

By comparing between Figures 5.5.a and 5.5.b, it can clearly be seen that the two bands at -13 and -10.5 eV in the isolated molecule have shifted via adsorption. The band at -13 eV corresponds to the 2σ states (bonding) from the N atom in the NH whereas the band at -10.5 eV corresponds to the 3σ state (lone pair) from the N atom in the NH. When the NH adsorbs on the Ni(111) surface the bonding band shifts away from the Fermi level (-16 eV) while the lone pair band shifts toward the Fermi level (-8 eV). So, the N bonding state does not contribute to the NH-surface bonding whereas the N lone pair state contributes to the bonding with the surface. In addition, the valence bands between -2 eV and the Fermi level in the isolated NH lose their density and smear out via adsorption. These bands represent the N atom 1π states (2 unpaired electrons) and the 3σ state of the NH (in the triplet state). These states involve most of the NH-surface bonding character.

On the other hand, Figure 5.5.d shows that the adsorption induces short and narrow bands at about -16 and -8 eV in the LDOS of the Ni atom in the adsorption system as compared to Figure 5.5.c (free Ni(111) surface). These bands correspond to the N atom in the adsorbed NH (bonding states (-16 eV) and lone pair states (-8 eV)). The N atom 1π states are also shown at -5 eV, indicating that they are populated when interacting with the nickel surface. Figure 5.5.d shows that the valence band is dominated by d states from Ni atoms. Therefore, the NH-surface bonding (the valence band) is a mixture of Ni atom d states and N atom lone pair state and 1π states to which the d-states contribute the most.

From the spin density plot, shown in Figure 5.6, spin up and spin down densities of N atom are very similar. Which leads to the conclusion that the NH interacts with the surface more as an imide (singlet NH^{2-}) rather than as an imidyl (doublet $NH^{\bullet -}$) radical anion or as a nitrene (triplet NH••) radical. The NH_2 also interacts with the surface as an amide (NH_2^-) rather than as an aminyl ($NH_2\bullet$) radical via analysis of its up and down spin densities, see Figure 5.13 of Appendix. Furthermore, from our calculations, anilide is found to adsorb in similar way as amide based on its adsorption structure and vibration, thus one may surmise that anilide interacts with the surface as an anion ($C_6H_5(H)\ N^-$) rather than anilinyl ($C_6H_5(H)\ N\bullet$).

Electronic properties of imide on the heterogeneous Ni(111) surface are thus quite different from the electronic states of a homogeneous imide-nickel model,[28] where imide interacts as an imidyl ($NR^{\bullet -}$) radical anion, R = hydrocarbyl substituent. These electronic states may allow homogeneous imide systems to undergo hydrogen atom abstraction (HAA) reactions, which are disfavored in heterogeneous models.

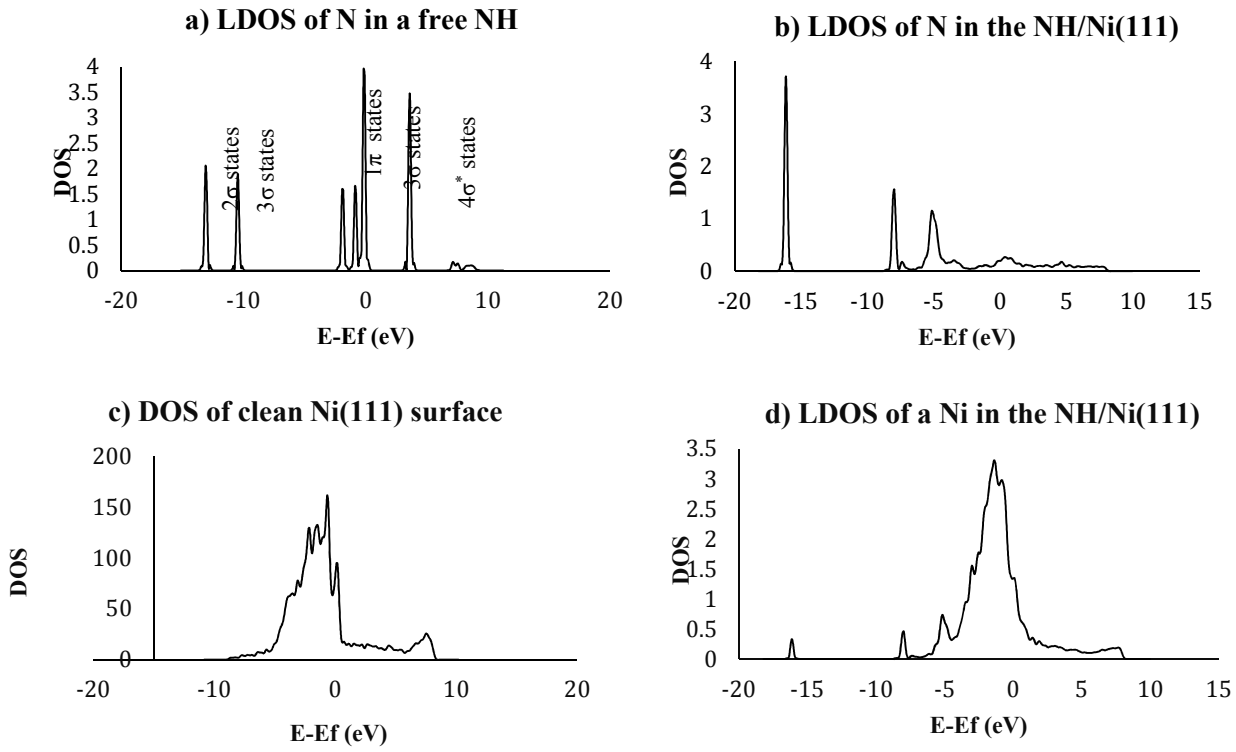

Figure 5.5 The local density (LDOS) of N in NH (a), N (b), and Ni (d) in NH/Ni(111) system and the density of states (DOS) of clean Ni(111) surface (c).

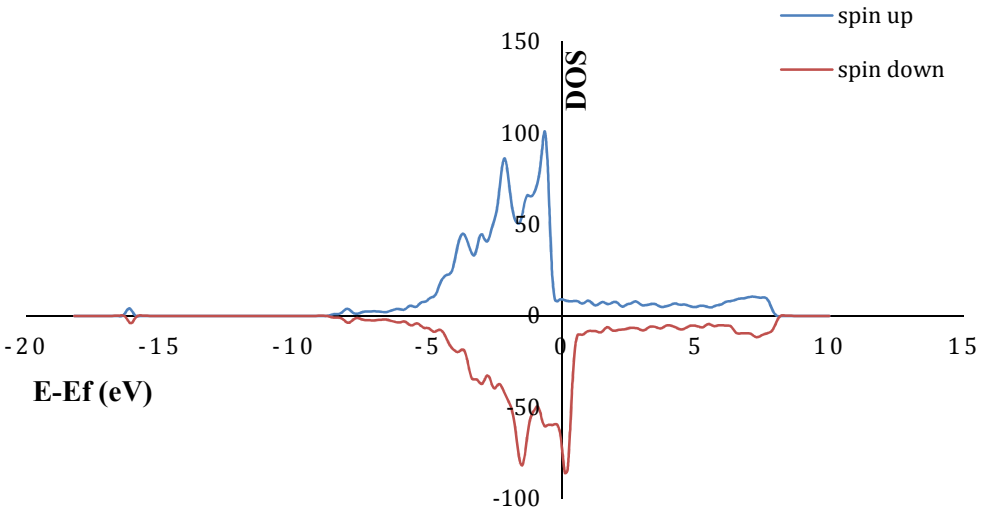

Figure 5.6 Spin density of the NH/Ni(111) system.

5.4. Conclusions

This study presents an initial step toward understanding and identifying relevant species involved in the direct amination of benzene using first principles density functional calculations. Calculations predict aniline adsorbs parallel to the surface via the aromatic ring and the nitrogen atom. The adsorption energy of aniline is higher (less stable) than benzene indicating weaker π interaction with the surface. Among all the species, imide (NH) and benzene are predicted to be the most stable on the Ni(111) surface. The DOS calculations predict that NH interacts with the surface as an imide (NH^{2-}) and NH_2 as amide (NH_2^-), and hence quite different from molecular analogues, which have more radical character in the ligands. Three reaction pathways were proposed relevant to the direct amination of benzene on the Ni(111) surface, and based on the thermodynamics, the reaction involves producing a surface-bound anilide and then coupling between NHC_6H_5 and H on the Ni(111) surface seems most likely to produce aniline than the other reaction pathways. Anilide adsorbs vertically on the Ni(111) surface on similar way as an amide, thus one may surmise that anilide interacts with the surface as an anion ($C_6H_5(H)\ N^-$). More detailed conclusions about the catalytic potential of Ni(111) surface for the direct amination of benzene cannot be drawn at this stage until the kinetic study of the transition states, coverage, and activation energies is completed.

APPENDIX

APPENDIX

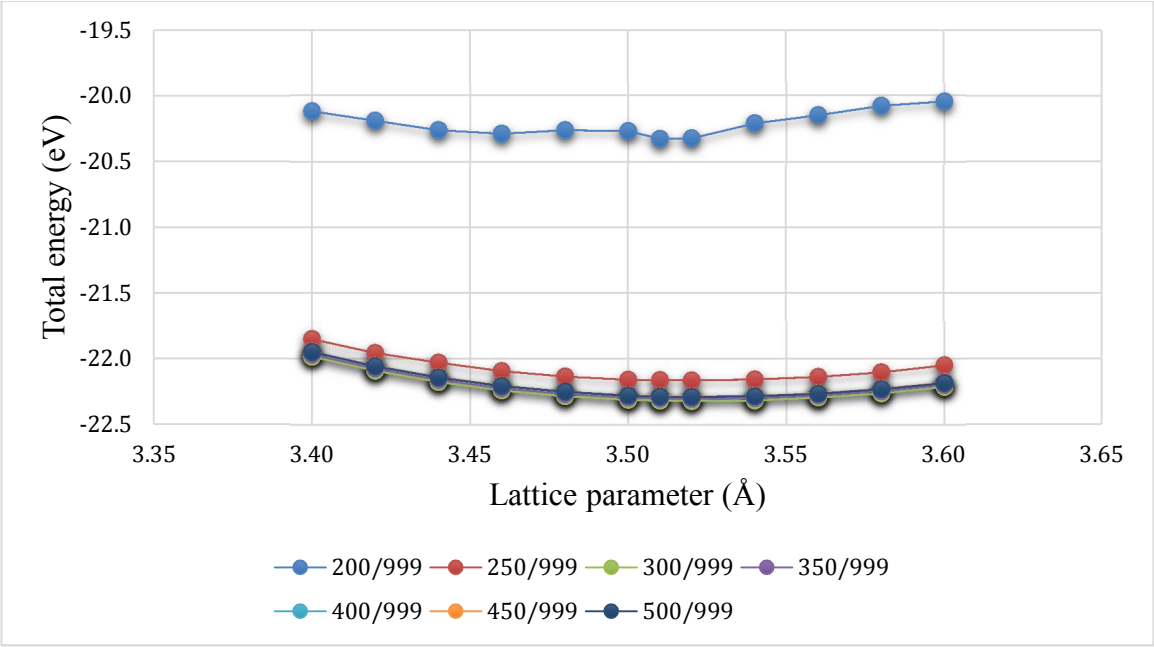

Figure 5.7 Lattice constant convergence test for bulk fcc Ni using variable E_{cutoff} and fixed k-points (9x9x9). The DFT-optimized lattice constant is 3.52 Å

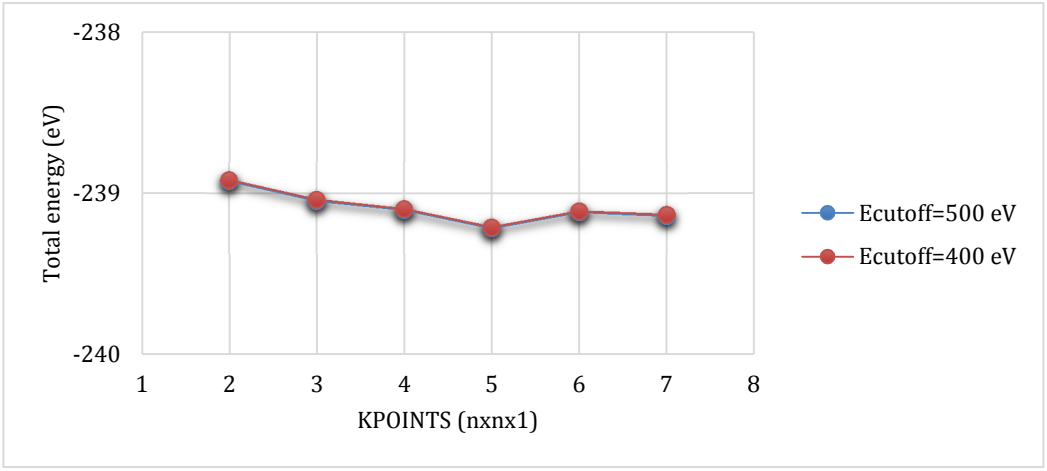

Figure 5.8 K-points convergence test for the Ni(111) surface using two values of E_{cutoff} (400 and 500 eV). The optimal set of k-points for our systems is 5x5x1.

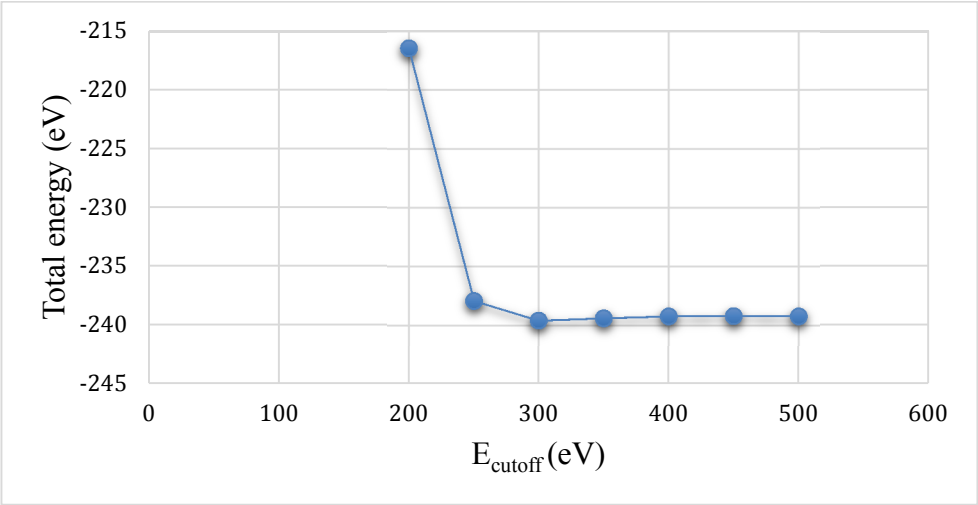

Figure 5.9 Energy cut off convergence test for the Ni(111) surface using 5x5x1 k-points. The optimal energy cut off for our systems is 400 eV.

a) NH_2^*(fcc site)

b) NH_2^*(atop site)

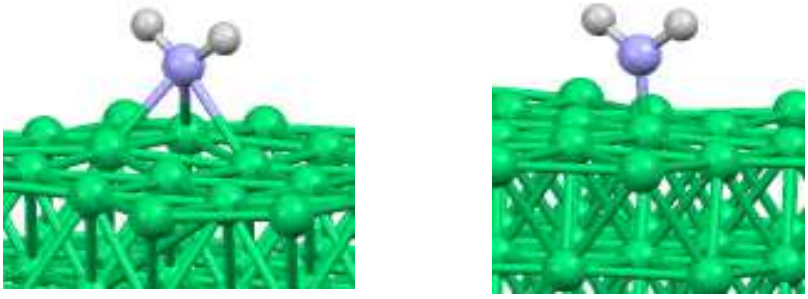

E_{ad} = -54.9 kcal mol^{-1}

E_{ad} = -24.1 kcal mol^{-1}

Figure 5.10 Adsorption sites and adsorption energies (E_{ad}) of NH_2 adsorbed on an fcc site (a), and NH_2 adsorbed on an atop site (b) of the Ni(111) surface. (*) Indicates an adsorbed molecule.

a) $C_6H_5^*$(nearly vertical) (hcp site)

b) $C_6H_5^*$ (vertical) (bridge site)

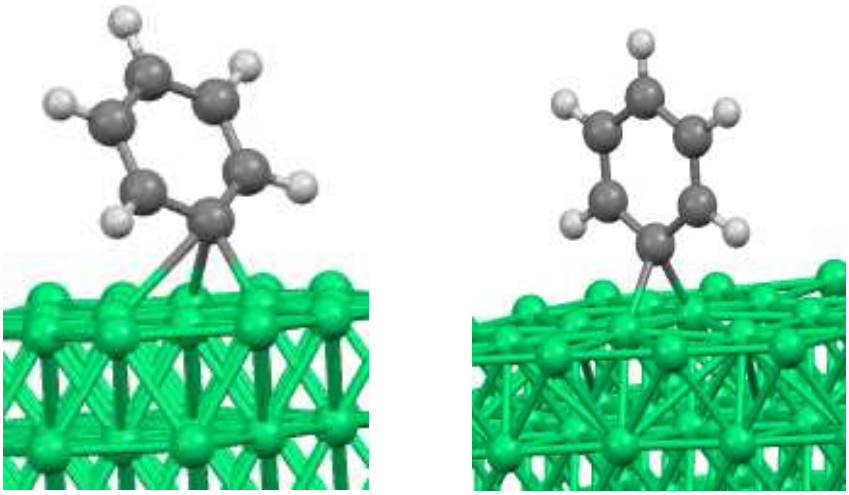

E_{ad} = - 48.4 kcal mol^{-1}

E_{ad} = - 40.8 kcal mol^{-1}

Figure 5.11 Adsorption sites and adsorption energies (E_{ad}) of C_6H_5 adsorbed on an hcp site (a), and C_6H_5 adsorbed on an bridge site (b) of the Ni(111) surface. (*) Indicates an adsorbed molecule.

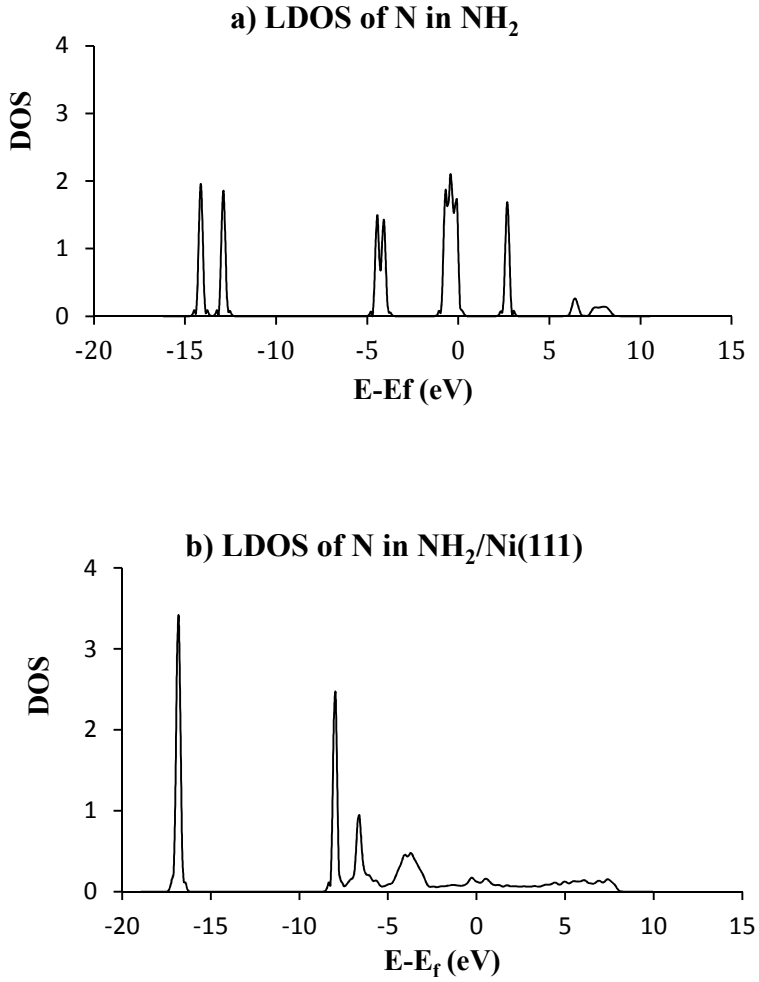

Figure 5.12 The local density of states (LDOS) of N in NH_2 (doublet) (a), N (b), in NH_2/Ni(111) system.

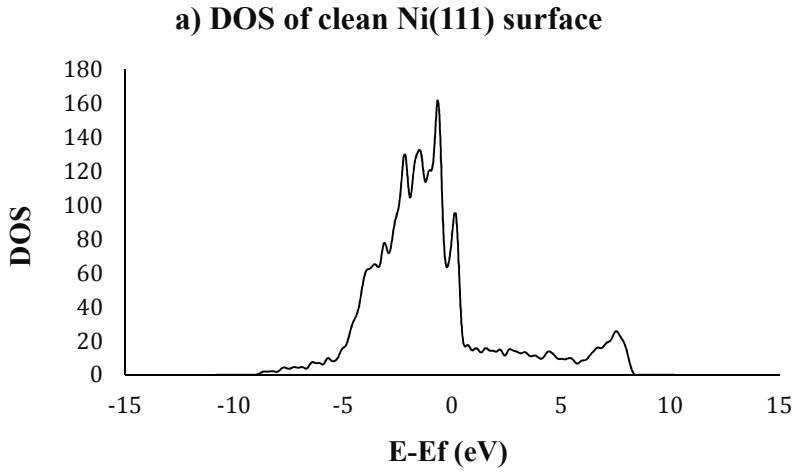

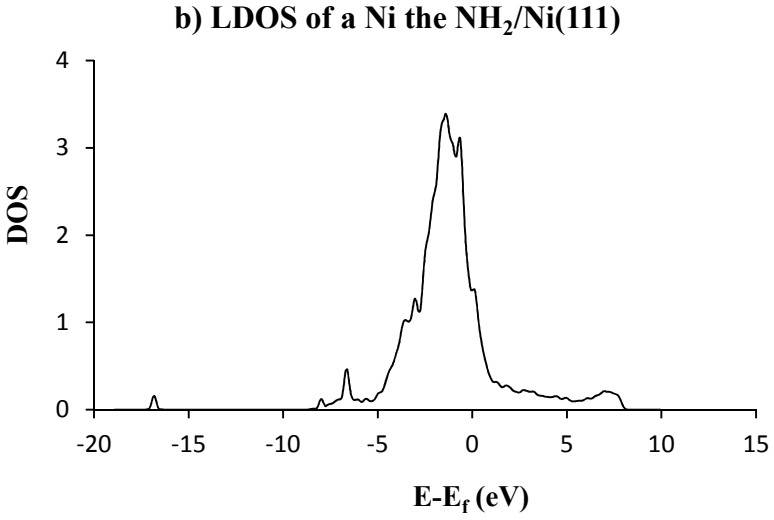

Figure 5.13 The density of states (DOS) of clean Ni(111) surface (a) and the local density of states (LDOS) of Ni in NH_2/Ni(111) system (b).

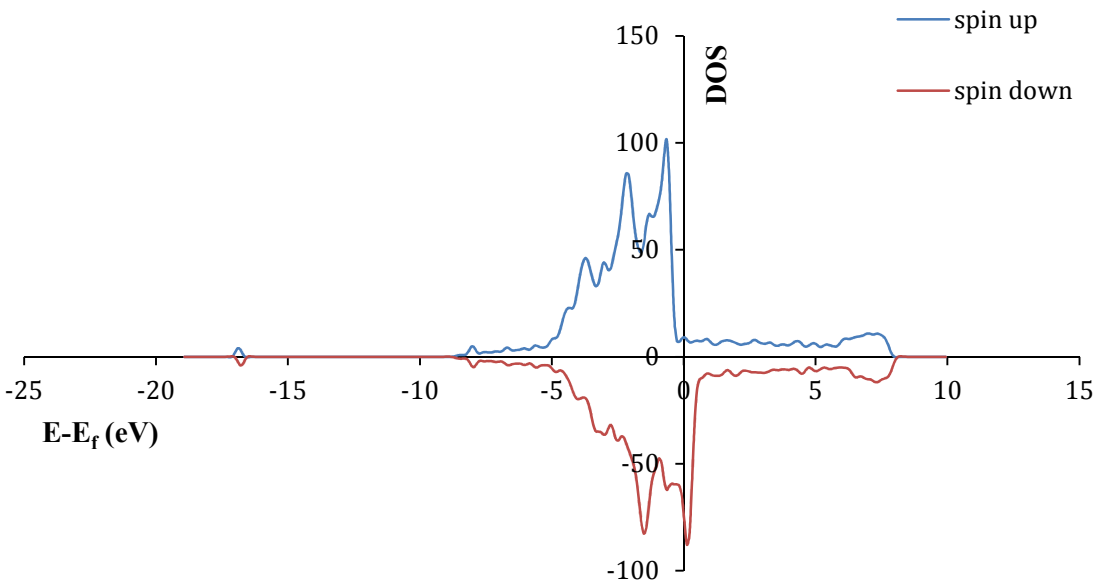

Figure 5.14 Spin density of the NH_2/Ni(111) system.

Table 5.14 Bond lengths (r) in Å and bond angles (a) in degree of free and adsorbed benzene and phenyl.

Compound	r(C-H)	r(C-C)	a(CCH)	r(C-Ni)	a(CCC)
C_6H_6	1.091	1.397, 1.398	120.0	-	120.0
C_6H_6 (expt.)[a]	1.084	1.397	120.0	-	120.0
C_6H_6/Ni(111)*	1.093, 1.095	1.433, 1.449, 1.434, 1.450	118.5, 118.0, 117.9, 117.8	2.060, 2.081, 2.085, 2.079	121.8, 121.1, 117.7
C_6H_5	1.091, 1.092	1.405, 1.376, 1.398	122.6, 119.6, 120.3, 121.0	-	126.2, 116.4, 120.1, 120.7
C_6H_5/Ni(111)**	1.092, 1.095, 1.094, 1.093	1.438, 1.429, 1.458, 1.459, 1.433, 1.432	119.4, 120.3, 119.3, 119.1, 118.4	2.237, 2.002, 2.411, 2.076, 2.475, 2.487, 2.000, 2.305, 1.905	116.0, 119.8,119.6, 120.5, 118.7, 120.8

[a]Reference 60. *CCCH = 161.9°, 161.3°, 151.8°, and 150.7°. ** $C_{radicl}CCH$= 176.7° and 176.5°, $HCC_{radicl}C$= 144.7° and 148.3°, and CCCH= 164.2°, 161.5°, and 159.5°.

Table 5.15 Bond lengths (r) in Å and bond angles (a) in degree of free and adsorbed aniline and anilide.

Compound	r(C-H) [r(N-H)]	r(C-C) [r(C-N)]	a(CCH)	r(C-Ni) [r(N-Ni)]	a(CCN) [a(HNH)]	a(CCC)
$C_6H_5NH_2$	1.090, 1.092, 1.091 [1.014]	1.407, 1.393, 1.398 [1.394]	119.1, 120.6, 120.4, 120.1, 120.0	-	120.7 [112.7]	118.5, 120.5, 118.9, 120.8
$C_6H_5NH_2$ (expt.)[a]	1.084	1.397, 1.394, 1.396 [1.402]	-	-	- [113.1]	119.4, 120.1, 120.7, 118.9
$C_6H_5NH_2$/Ni(111)	1.090, 1.093, 1.096, 1.094 [1.021, 1.022]	1.433, 1.448, 1.456, 1.430, 1.452, 1.451 [1.435]	117.6, 118.8, 118.3, 116.2, 118.9	2.056, 2.064, 2.094, 2.057, 2.040, 2.585, 2.133 [2.084]	116.0, 120.6 [110.0]	116.4, 121.7, 117.5, 120.4, 122.6
C_6H_5NH	1.090, 1.092, 1.091 [1.032]	1.407, 1.383, 1.437 [1.340]	118.3, 120.2, 119.8, 119.6, 121.8	-	124.6, 118.09	117.3, 120.9, 120.4, 120.1, 120.2, 121.1
C_6H_5NH/Ni(111) *	1.103, 1.092, 1.091, 1.094 [1.030]	1.403, 1.392, 1.398, 1.399, 1.393, 1.410 [1.416]	119.4, 120.2, 120.4, 119.5, 119.3	- [1.995, 1.974]	119.2, 122.6	118.2, 121.0, 120.4, 119.2, 120.5, 120.8

[a]Reference 72. *a(HNNi)= 108.2° and 104.3°, a(NiNNi)= 76.5°, a(NiNC)= 127.4° and 130.0°, and r(Ni-Ni) = 2.458 Å.

Table 5.16 Calculated vibrational frequencies of gas phase and adsorbed aromatic species, in cm^{-1}.

Compound	Calculated vibrational frequencies (cm^{-1})	
	Gas phase	Adsorbed
Benzene	3131	3095
	3122	3086
	3121	3084
	3106	3074
	3105	3065
	3096	3059
	1586	1439
	1586	1422
	1465	1384
	1465	1376
	1337	1353
	1336	1291
	1166	1126
	1165	1120
	1142	1097
	1036	985
	1035	945
	993	941
	991	884
	987	880
	959	869
	958	826
	838	806
	837	750
	704	741
	666	599
	600	551
	599	540
	397	450
	397	437
ZPE	2.66	2.56
Phenyl	3120	3112
	3108	3089
	3105	3085
	3093	3072
	3088	3061
	1590	1426
	1527	1422
	1425	1350
	1425	1347
	1328	1306
	1268	1194
	1145	1121
	1145	1106

Table 5.16 Continued.

	1050	981
	1029	951
	998	947
	969	915
	957	862
	939	850
	869	790
	792	754
	701	735
	655	628
	597	584
	576	550
	412	516
	383	445
ZPE	2.31	2.24
Aniline	3580	3487
	3479	3395
	3125	3096
	3108	3088
	3102	3076
	3087	3063
	3087	3048
	1612	1553
	1599	1447
	1582	1419
	1489	1384
	1457	1372
	1356	1343
	1324	1272
	1281	1174
	1168	1115
	1147	1094
	1109	1070
	1039	971
	1026	950
	983	907
	958	865
	941	840
	859	793
	814	763
	802	741
	740	707
	685	706
	614	573
	549	548
	519	498
	489	485
	404	463

Table 5.16 Continued.

	377	440
	348	375
	211	350
ZPE	3.11	3.01
Anilide	3313	3292
	3130	3130
	3123	3114
	3111	3105
	3102	3084
	3091	2915
	1552	1578
	1522	1567
	1450	1472
	1433	1445
	1347	1371
	1319	1332
	1303	1237
	1156	1196
	1143	1167
	1142	1155
	1062	1084
	1006	1027
	973	980
	966	975
	960	946
	892	876
	812	821
	806	794
	764	752
	679	709
	653	670
	597	616
	518	568
	467	508
	407	497
	374	404
	186	329
ZPE	2.75	2.78

REFERENCES

REFERENCES

(1) Aniline. *Ullmann's Encyclopedia of Industrial Chemistry*; Wiley-VCH Verlag GmbH & Co. KGaA: Weinheim, Germany, 2011; Vol.3, pp 465–478.

(2) Saha, B.; De, S.; Dutta, S. Recent Advancements of Replacing Existing Aniline Production Process With Environmentally Friendly One-Pot Process: An Overview. *Crit. Rev. Env. Sci. Technol.* **2013**, *43* (1), 84–120.

(3) Blanksby, S. J.; Ellison, G. B. Bond Dissociation Energies of Organic Molecules. *Acc. Chem. Res.* **2003**, *36* (4), 255–263.

(4) Becker, J.; Hölderich, W. F. Amination of Benzene in the Presence of Ammonia Using a Group VIII Metal Supported on a Carrier as Catalyst. *Catal. Lett.* **1988**, *54* (3), 125–128.

(5) Hagemeyer, A.; Borade, R.; Desrosiers, P.; Guan, S.; Lowe, D. M.; Poojary, D. M.; Turner, H.; Weinberg, H.; Zhou, X.; Armbrust, R.; Fengler, G.; Notheis, U. Application of Combinatorial Catalysis for the Direct Amination of Benzene to Aniline. *Appl. Catal. A Gen.* **2002**, *227*, 43–61.

(6) Guo, B.; Zhang, Q.; Li, G.; Yao, J.; Hu, C. Aromatic C-N Bond Formation via Simultaneous Activation of C-H and N-H Bonds: Direct Oxyamination of Benzene to Aniline. *Green Chem.* **2012**, *14* (7), 1880–1883.

(7) Hoffmann, N.; Löffler, E.; Breuer, N. A.; Muhler, M. On the Nature of the Active Site for the Oxidative Amination of Benzene to Aniline over NiO/ZrO_2 as Cataloreactant. *ChemSusChem.* **2008**, *1*, 393–396.

(8) Hoffmann, N.; Muhler, M. On the Mechanism of the Oxidative Amination of Benzene with Ammonia to Aniline Over NiO/ZrO_2 as Cataloreactant. *Catal. Lett.* **2005**, *103* (1–2), 155–159.

(9) Hu, C.; Zhu, L.; Xia, Y. Direct Amination of Benzene to Aniline by Aqueous Ammonia and Hydrogen Peroxide over $V-Ni/Al_2O_3$ Catalyst with Catalytic Distillation. *Ind. Eng. Chem. Res.* **2007**, *46* (10), 3443–3445.

(10) Kuznetsova, N. I.; Kuznetsova, L. I.; Detusheva, L. G.; Likholobov, V. A.; Pez, G. P.; Cheng, H. Amination of Benzene and Toluene with Hydroxylamine in the Presence of Transition Metal Redox Catalysts. *J. Mol. Catal. A Chem.* **2000**, *161* (1–2), 1–9.

(11) Lü, Y. F.; Zhu, L. F.; Liu, Q. Y.; Guo, B.; Hu, X. K.; Hu, C. W. Direct Amination of Benzene to Aniline with Several Typical Vanadium Complexes. *Chinese Chem. Lett.* **2009**, *20* (2), 238–240.

(12) Yu, T.; Zhang, Q.; Xia, S.; Li, G.; Hu, C. Direct Amination of Benzene to Aniline by Reactive Distillation Method over Copper Doped Hierarchical TS-1 Catalyst. *Catal. Sci. Technol.* **2014**, *4* (3), 639–647.

(13) Yuzawa, H.; Yoshida, H. Direct Aromatic-Ring Amination by Aqueous Ammonia with a Platinum Loaded Titanium Oxide Photocatalyst. *Chem. Commun.* **2010**, *46*, 8854–8856.

(14) Zhu, L. F.; Guo, B.; Tang, D. Y.; Hu, X. K.; Li, G. Y.; Hu, C. W. Sodium Metavanadate Catalyzed One-Step Amination of Benzene to Aniline with Hydroxylamine. *J. Catal.* **2007**, *245* (2), 446–455.

(15) Tang, D.; Zhu, L.; Hu, C. Comprehensive DFT Study of the Mechanism of Vanadium-Catalyzed Amination of Benzene with Hydroxylamine. *Organometallics* **2011**, *30* (21), 5675–5686.

(16) Yu, T.; Yang, R.; Xia, S.; Li, G.; Hu, C. Direct Amination of Benzene to Aniline with H_2O_2 and $NH_3 \cdot H_2O$ over Cu/SiO_2 Catalyst. *Catal. Sci. Technol.* **2014**, *4* (9), 3159-3167.

(17) Zhai, H.; Lin, H.; Lu, X.; Xia, X.-H. Highly Efficient Amination of Benzene to Aniline Mediated by Bromine with Metal Oxide as Cataloreactant. *Chem. Lett.* **2006**, *35* (12), 1358–1359.

(18) Yuzawa, H.; Kumagai, J.; Yoshida, H. Reaction Mechanism of Aromatic Ring Amination of Benzene and Substituted Benzenes by Aqueous Ammonia over Platinum-Loaded Titanium Oxide Photocatalyst. *J. Phys. Chem. C* **2013**, *117* (21), 11047–11058.

(19) Squire, E. N. Synthesis of Aromatic Amines by Reaction of Aromatic Compounds with Ammonia. U.S. Patent 3,929,889, Dec 30, 1975.

(20) Squire, E. N. Synthesis of Aromatic Amines by Reaction of Aromatic Compounds with Ammonia. U.S. Patent 3,919,155, Nov 11, 1975.

(21) DelPesco, T. W. Synthesis of Aromatic Amines by Reaction of Aromatic Compounds with Ammonia. U.S. Patent 4,031,106, June 21, 1977.

(22) DelPesco, T. W. Synthesis of Aromatic Amines by Reaction of Aromatic Compounds with Ammonia. U.S. Patent 4,001,260, Jan 4, 1977.

(23) Poojary, D. M.; Borade, R.; Hangmeyer, A.; Zhou, X.-P.; Dube, C. E.; Notheis, U.;

Armbrust, R.; Rasp, C.; Lowe, D. M. Amination of Aromatic Hydrocarbons and Heterocyclic Analogs Thereof. U.S. Patent 6,933,409, Aug 23, 2005.

(24) Thomas, C. L. Preparation of Aromatic Amines. Canadian Patent 553,988A, Apr 3, 1958.

(25) Acharyya, S. S.; Ghosh, S.; Bal, R. Direct Catalytic Oxyamination of Benzene to Aniline over Cu(II) Nanoclusters Supported on $CuCr_2O_4$ Spinel Nanoparticles via Simultaneous Activation of C–H and N–H Bonds. *Chem. Commun.* **2014**, *50* (50), 13311–13314.

(26) Huang, S. X.; Fischer, D. A.; Gland, J. L. Aniline Hydrogenolysis on Nickel: Effects of Surface Hydrogen and Surface Structure. *Cata. Lett.* **1995**, *34*, 365–374.

(27) Huang, S. X.; Fischer, D. A.; Gland, J. L. Aniline Adsorption, Hydrogenation, and Hydrogenolysis on the Ni(100) Surface. *J. Phys. Chem.* **1996**, *100* (24), 10223–10234.

(28) Wiese, S.; McAfee, J. L.; Pahls, D. R.; McMullin, C. L.; Cundari, T. R.; Warren, T. H. C–H Functionalization Reactivity of a Nickel–Imide. *J. Am. Chem. Soc.* **2012**, *134* (24), 10114–10121.

(29) Kresse, G.; Hafner, J. Ab Initio Molecular-Dynamics Simulation of the Liquid-Metal-Amorphous-Semiconductor Transition in Germanium. *Phys. Rev. B* **1994**, *49* (20), 14251–14269.

(30) Kresse, G.; Furthmüller, J. Efficient Iterative Schemes for Ab Initio Total-Energy Calculations Using a Plane-Wave Basis Set. *Phys. Rev. B* **1996**, *54* (16), 11169–11186.

(31) Kresse, G.; Hafner, J. Ab Initio Molecular Dynamics for Liquid Metals. *Phys. Rev. B*, 1993, *47*, 558–561.

(32) Kresse, G.; Furthmüller, J. Efficiency of Ab-Initio Total Energy Calculations for Metals and Semiconductors Using a Plane-Wave Basis Set. *Comput. Mater. Sci.* **1996**, *6* (1), 15–50.

(33) Perdew, J. P.; Burke, K.; Ernzerhof, M. Generalized Gradient Approximation Made Simple. *Phys. Rev. Lett.* **1996**, *77*, 3865–3868.

(34) Perdew, J. P.; Burke, K.; Ernzerhof, M. Erratum: Generalized Gradient Approximation Made Simple. *Phys. Rev. Lett.* **1997**, *78*, 1396–1396.

(35) Blöchl, P. E. Projector Augmented-Wave Method. *Phys. Rev. B* **1994**, *50* (24), 17953–17979.

(36) Kresse, G.; Joubert, D. From Ultrasoft Pseudopotentials to the Projector Augmented-

Wave Method. *Phys. Rev. B* **1999**, *59* (3), 1758–1775.

(37) Grimme, S.; Antony, J.; Ehrlich, S.; Krieg, H. A Consistent and Accurate Ab Initio Parametrization of Density Functional Dispersion Correction (DFT-D) for the 94 Elements H-Pu. *J. Chem. Phys.* **2010**, *132* (15), 154104–154123.

(38) Kresse, G.; Hafner, J. First-Principles Study of the Adsorption of Atomic H on Ni (111), (100) and (110). *Surf. Sci.* **2000**, *459* (3), 287–302.

(39) Methfessel, M.; Paxton, A. T. High-Precision Sampling for Brillouin-Zone Integration in Metals. *Phys. Rev. B* **1989**, *40* (6), 3616–3621.

(40) Taylor, A. Lattice Parameters of Binary Nickel Cobalt Alloys. *J. Inst. Met.* **1950**, *77*, 585–594.

(41) Blaylock, D. W.; Teppei Ogura; William, H. G.; Gregory, J. O. B. Computational Investigation of Thermochemistry and Kinetics of Steam Methane Reforming on Ni(111) under Realistic Conditions. *J. Phys. Chem. C* **2009**, *113* (12), 4898–4908.

(42) Luo, Y.-R. *Comprehensive Handbook of Chemical Bond Energies*; Taylor & Francis Group, LLC.: Boca Raton, FL, US, 2007.

(43) McMillen, D. F.; Golden, D. M. Hydrocarbon Bond Dissociation Energies. *Annu. Rev. Phys. Chem.* **1982**, *33* (1), 493–532.

(44) Netzer, F. P.; Madey, T. E. Interaction of NH_3 with Oxygen-Predosed Ni(111). *Surf. Sci.* **1982**, *119* (2–3), 422–432.

(45) Seabury, C. W.; Rhodin, T. N.; Purtell, R. J.; Merrill, R. P. Chemisorption and Reaction of NH_3 on Ni(111). *Surf. Sci.* **1980**, *93* (1), 117–126.

(46) Duan, X.; Ji, J.; Qian, G.; Fan, C.; Zhu, Y.; Zhou, X.; Chen, D.; Yuan, W. Ammonia Decomposition on Fe(110), Co(111) and Ni(111) Surfaces: A Density Functional Theory Study. *J. Mol. Catal. A Chem.* **2012**, *357*, 81–86.

(47) Kurten, T.; Biczysko, M.; Rajamäki, T.; Laasonen, K.; Halonen, L. Computational Study of the Adsorption Energetics and Vibrational Wavenumbers of NH_3 Adsorbed on the Ni(111) Surface. *J. Phys. Chem. B* **2005**, *109* (18), 8954–8960.

(48) Diawara, B.; Joubert, L.; Costa, D.; Marcus, P.; Adamo, C. Ammonia on Ni(111) Surface Studied by First Principles: Bonding, Multilayers Structure and Comparison with Experimental IR and XPS Data. *Surf. Sci.* **2009**, *603* (20), 3025–3034.

(49) Bertolini, J. C.; Dalmai-Imelik, G.; Rousseau, J. Benzene Adsorption on Nickel (100) and (111) Faces Studied by Leed and High Resolution Electron Energy Loss Spectroscopy. *Surf. Sci.* **1977**, *67* (2), 478–479.

(50) Myers, A. K.; Schoofs, G. R.; Benziger, J. B. Comparison of Benzene Adsorption on nickel(111) and nickel(100). *J. Phys. Chem.* **1987**, *91* (9), 2230–2232.

(51) Lehwald, S.; Ibach, H.; Demuth, J. E. Vibration Spectroscopy of Benzene Adsorbed on Pt(111) and Ni(111). *Surf. Sci.* **1978**, *78* (3), 577–590.

(52) Yamagishi, S.; Jenkins, S. J.; King, D. A. Symmetry and Site Selectivity in Molecular Chemisorption: Benzene on Ni{111}. *J. Chem. Phys.* **2001**, *114* (13), 5765–5773.

(53) Mittendorfer, F.; Hafner, J. Density-Functional Study of the Adsorption of Benzene on the (111), (100) and (110) Surfaces of Nickel. *Surf. Sci.* **2001**, *472* (1–2), 133–153.

(54) Liu, W.; Ruiz, V. G.; Zhang, G.-X.; Santra, B.; Ren, X.; Scheffler, M.; Tkatchenko, A. Structure and Energetics of Benzene Adsorbed on Transition-Metal Surfaces: Density-Functional Theory with van Der Waals Interactions Including Collective Substrate Response. *New J. Phys.* **2013**, *15* (5), 053046–053072.

(55) Campbell, C. T.; Árnadóttir, L.; Sellers, J. R. V. Kinetic Prefactors of Reactions on Solid Surfaces. *Z. Phys. Chem.* **2013**, *227* (9–11), 1435–1454.

(56) Yildirim, H.; Greber, T.; Kara, A. Trends in Adsorption Characteristics of Benzene on Transition Metal Surfaces: Role of Surface Chemistry and van Der Waals Interactions. *J. Phys. Chem. C* **2013**, *117* (40), 20572–20583.

(57) Tonigold, K.; Groß, A. Dispersive Interactions in Water Bilayers at Metallic Surfaces: A Comparison of the PBE and RPBE Functional Including Semiempirical Dispersion Corrections. *J. Comput. Chem.* **2012**, *33* (6), 695–701.

(58) Redondo, A.; Zeiri, Y.; Low, J. J.; Goddard, W. A. Application of Transition State Theory to Desorption from Solid Surfaces: Ammonia on Ni(111). *J. Chem. Phys.* **1983**, *79* (12), 6410–6415.

(59) Duan, X.; Qian, G.; Liu, Y.; Ji, J.; Zhou, X.; Chen, D.; Yuan, W. Structure Sensitivity of Ammonia Decomposition over Ni Catalysts: A Computational and Experimental Study. *Fuel Process. Technol. Spec. Issue APCRE11* **2013**, *108*, 112–117.

(60) Herzberg, G. *Electronic Spectra of Polyatomic Molecules*; D. Van Nostrand Company Inc.,: Princeton, NJ, US, 1967.

(61) Haynes, W. M.; Lide, D. R.; Bruno, T. J. *CRC Handbook of Chemistry and Physics : A Ready-Reference Book of Chemical and Physical Data*, 94th ed.; CRC Press, Taylor & Francis Group: Boca Raton, Florida, US, 2013.

(62) Huang, W.; Lai, W.; Xie, D. First-Principles Study of Decomposition of NH_3 on Ir(100). *Surf. Sci.* **2008**, *602* (6), 1288–1294.

(63) Schindler, K. M.; Fritzsche, V.; Asensio, M. C.; Gardner, P.; Ricken, D. E.; Robinson, A. W.; Bradshaw, A. M.; Woodruff, D. P.; Conesa, J. C.; González-Elipe, A. R. Structural Determination of a Molecular Adsorbate by Photoelectron Diffraction: Ammonia on Ni{111}. *Phys. Rev. B* **1992**, *46* (8), 4836–4843.

(64) Shimanouchi, T. Tables of Molecular Vibrational Frequencies. Consolidated Volume II. *J. Phys. Chem. Ref. Data* **1977**, *6* (3), 993–1102.

(65) Jacox, M. E. Vibrational and Electronic Energy Levels of Polyatomic Transient Molecules. Supplement B. *J. Phys. Chem. Ref. Data* **2003**, *32* (1), 1–441.

(66) Irikura, K. K. Experimental Vibrational Zero-Point Energies: Diatomic Molecules. *J. Phys. Chem. Ref. Data* **2007**, *36* (2), 389–397.

(67) Fisher, G. B.; Mitchell, G. E. A Vibrational Study of Ammonia Chemisorbed on Ni(110) and Ni(111): Whither Goest the Metal-Nitrogen Stretching Mode on FCC (111) Surfaces? *J. Electron Spectros. Relat. Phenomena* **1983**, *29* (1), 253–259.

(68) Feng, H.; Ma, J.; Hu, Z. Six-Membered-Ring-Based Radical Mechanism for Catalytic Growth of Carbon Nanotubes with Benzene Precursor. *J. Phys. Chem. C* **2009**, *113* (37), 16495–16502.

(69) Kishi, K.; Chinomi, K.; Inoue, Y.; Ikeda, S. X-Ray Photoelectron Spectroscopic Study of the Adsorption of Benzene, Pyridine, Aniline, and Nitrobenzene on Evaporated Nickel and Iron. *J. Catal.* **1979**, *60* (2), 228–240.

(70) Myers, A. K.; Benziger, J. B. Effect of Substituent Groups on the Interaction of Benzene with Ni(111). *Langmuir* **1989**, *5* (6), 1270–1288.

(71) Schoofs, G. R.; Benziger, J. B. Reactions of Organonitrogen Molecules with Ni(100). *J. Phys. Chem.* **1988**, *92* (3), 741–750.

(72) Schultz, G.; Portalone, G.; Ramondo, F.; Domenicano, A.; Hargittai, I. Molecular Structure of Aniline in the Gaseous Phase: A Concerted Study by Electron Diffraction and Ab Initio Molecular Orbital Calculations. *Struct. Chem.* **1996**, *7* (1), 59–71.

(73) Friderichsen, A. V.; Radziszewski, J. G.; Nimlos, M. R.; Winter, P. R.; Dayton, D. C.; Donald, E. D.; Ellison, G. B. The Infrared Spectrum of the Matrix-Isolated Phenyl Radical. *J. Am. Chem. Soc.* **2001**, *123*, 1977–1988.

(74) Evans, J. C. The Vibrational Assignments and Configuration of Aniline, Aniline-NHD and Aniline-ND2. *Spectrochim. Acta* **1960**, *16* (4), 428–442.

(75) Bertolini, J. C.; Rousseau, J. On the Vibrational Electron Energy Loss Spectra of Benzene Chemisorbed on the (111) and (100) Nickel Faces. *Surf. Sci.* **1979**, *89*, 467–476.

(76) Kizilkaya, A. C.; Niemantsverdriet, J. W.; Weststrate, C. J. Ammonia Adsorption and Decomposition on Co(0001) in Relation to Fischer–Tropsch Synthesis. *J. Phys. Chem. C* **2016**, *120* (7), 3834–3845.

CHAPTER 6 CONCLUDING REMARKS

In this dissertation, several computational approaches and thermochemical schemes have been utilized to establish effective routes for the determination of accurate structural and thermochemical properties of various sets of molecular systems. To assess the reliability of these approaches, enthalpies of formation were calculated and compared to experimental data. Another aspect of this work includes the application of periodic density functionals on a heterogeneous catalytic process for the identification of possible reaction intermediates and the prediction of thermodynamically preferred reaction pathways. A brief summary of these projects and possible future directions is provided below.

6.1 DFT and Composite Methods Investigations

6.1.1 Enthalpies of Formation for Oxygen Fluoride Species via Atomization Approach

In Chapter 3, the reliability of the ccCA, G3, and G3B3 composite methods for the prediction of the enthalpies ($\Delta H°_{f,298}{}'s$) of formation of oxygen fluoride species was assessed. In addition to these methods, the study employed the M06 and M06-2X functionals with various basis set sizes to examine their performance for the prediction of structures and $\Delta H°_{f,298}{}'s$ of the same set of oxygen fluoride species. Only seven of these molecules have known $\Delta H°_{f,298}{}'s$, hence determining an accurate theoretical approach would help to enable reliable predictions in the absence of experimental data. The ccCA-S3 method results in the lowest MAD among the methods tested. The MAD for ccCA-S3 was 1.4 kcal mol^{-1} with respect to the reference data (note, this includes data from experiments as well as high-level *ab initio* calculations). However, the MAD of ccCA-S3 was reduced to 0.6 kcal mol^{-1} when compared to the enthalpies of formation from the Active Thermochemical Tables (ATcT). The ATcT uses artificial intelligence

algorithms to reduce experimental uncertainties associated with the measured $\Delta H°_{f,298}{}'s$ by integrating experimental data with highly accurate theoretical thermochemical properties. G3 and G3B3 achieved MAD of 1.5 kcal mol^{-1} with respect to the reference data for the $\Delta H°_{f,298}{}'s$ of oxygen fluoride species while incorporating an empirical parameter that is intended to reduce the overall MAD. The MADs of G3 and G3B3 also were reduced when comparing to the ATcT values (0.8 kcal mol^{-1} for G3 and 0.7 kcal mol^{-1} for G3B3). To come to a conclusion about the performance of composite methods on halogen oxide species, $\Delta H°_{f,298}{}'s$ of chlorine oxides species are also calculated. The results show that ccCA-S3 still produces the lowest MAD of 1.1 kcal mol^{-1} for the chlorine oxides species, while G3 and G3B3 result in MADs of 2.3 and 3.5 kcal mol^{-1}, respectively. Thus, ccCA-S3 is recommended for halogen oxide systems and is promising for other halogen systems and peroxides. Another important finding from this study is that although the M06 and M06-2X density functionals are considered useful methods for main group species, they are not recommended for predicting structures and $\Delta H°_{f,298}{}'s$ for oxygen fluoride species.

6.1.2 Enthalpies of Formation for Organoselenium Compounds via Reactions Schemes

In Chapter 4, several thermochemical reaction schemes including isodesmic (RC2) and hypohomodesmotic (RC3) reaction schemes were employed to predict $\Delta H°_{f,298}{}'s$ of organoselenium compounds via composite methods and density functionals and the results were compared to the traditional atomization approach. The impact of the RC2 and RC3 schemes on the accuracy of the predicted $\Delta H°_{f,298}{}'s$ also was evaluated. Although RC2 and RC3 are both known to cancel most of the errors that arise from the differential correlation effects and size

extensivity, their impact on the accuracy of the $\Delta H°_{f,298}{}'s$ predicted using composite methods is not significant except for ccCA-S3 with respect to the RC0 approach. The reduction in the MAD of ccCA-S3 is -2.18 kcal mol^{-1} (RC2) and -1.87 (RC3) kcal mol^{-1} compared to RC0, showing higher accuracy when using RC2 and RC3 reaction schemes. The MADs of all four ccCA variants become nearly the same when using RC2 and RC3, which reduces the dependency on the various extrapolation schemes. G3 was found to be independent on the choice of thermochemical schemes, yet G4 shows a systematic reduction in the MAD going from RC0 to RC3. In contrast to the composite methods, a large decrease in MADs was seen when using the RC2 and RC3 schemes with the single point energy calculations utilized within the ccCA methodology. It is then extremely important to use these reaction schemes instead of the RC0 approach to predict accurate $\Delta H°_{f,298}{}'s$ for organoseleinum species. The accuracy of DFT increases when using the RC3 reaction scheme with an MAD of 0.76 kcal mol^{-1} for the calculated $\Delta H°_{f,298}{}'s$ of organoselenium compounds, with respect to experiments.

6.1.3 Future Interest

Although ccCA performed reasonably well when applied to oxygen fluoride species and chlorine oxides, it is of interest to examine the performance of more sophisticated methods such as multireference-ccCA (MR-ccCA) on these highly correlated set of molecules. In addition, because M06 and M06-2X perform less successfully with respect to experiment when applied to systems such as oxygen fluorides using the atomization approach, the use of isodesmic reaction schemes with these functionals would likely be more accurate based on results presented in these studies.

Organoselenium species are very important molecules in various fields of chemistry, materials science, and biochemistry. However, experimental thermochemical data, such as enthalpies of formation, are either very limited or associated with high uncertainties. Therefore, establishing reliable data experimentally and theoretically would be of great help for future work with these types of molecules. Particularly, an expanded database of enthalpies of formation of the elemental products and reactants of organoselenium species, which are very scarce, can improve the accuracy of the thermochemical reaction schemes, such as RC3. These reaction schemes then can be extended to define organoselenium compounds containing other heteroatoms, such as selenone, selenoxide, and selenocysteine, etc.

6.2 Periodic DFT for the Direct Amination of Benzene on the Ni(111)

The direct amination of benzene to produce aniline was listed by Haggin[1] as one of the top ten most challenging reaction for catalysis. As an effort to study this reaction theoretically on the Ni(111) surface, Chapter 5 presents an initial step of investigating various aspects such as identifying the adsorption behaviors and energetics of all intermediates involved in this reaction. First principle calculations predict that aniline adsorbs parallel to surface but the adsorption of aniline is less stable than benzene adsorption. Imide and benzene are found to be the most prevalent species among NH_x and aromatic adsorbed species, respectively. Information from the density of states shows that NH and NH_2 species interact with the Ni(111) as imide (NH^{2-}) and amide (NH_2^-) rather than radicals as is the case in the molecular analogues resulting in different C-H amination mechanisms. Three reaction pathways relevant to the direct amination of benzene on the Ni(111) were proposed and the reaction involves producing a surface-bound anilide and

then coupling between NHC_6H_5 and H on the Ni(111) surface seems the most thermodynamically favorable and, in turn, the most likely to produce aniline than other proposed mechanisms.

6.2.1 Future Interest

In order to use our results to design heterogeneous catalysts for the direct synthetic of aniline, a kinetic study is warranted. This includes the prediction of transition states and activation barriers. Another aspect that would contribute to this work is a study of the coverage effect of adsorbates on the Ni(111) surface, i.e. to calculate the adsorption of benzene on pre-adsorbed NH_x at different coverages and to investigate the adsorbate-adsorbate interactions. These calculations require the use of dispersion corrected density functional and a large surface unit (not less than 6x6) to accommodate the large aromatic species. Since PBE-D3 was not capable of capturing the molecule-surface interaction accurately, it would be of interest to use other dispersion corrected functionals such as optB88-vdW as it has shown utility for several adsorption systems.

REFERENCES

REFERENCES

(1) Haggin, J. Chemists Seek Greater Recognition for Catalysis. *Chem. Eng. News* **1993**, *71* (22), 23–27.